ATTRITION OF MANTLE CARGO DURING KIMBERLITE ASCENT: INSIGHTS FROM ANALOGUE EXPERIMENTS

by

DAVID SASSE

B.Sc., The University of British Columbia, 2016

A THESIS SUBMITTED IN PARTIAL FULFILLMENT OF

THE REQUIREMENTS FOR THE DEGREE OF

MASTER OF SCIENCE

in

THE FACULTY OF GRADUATE AND POSTDOCTORAL STUDIES

(Geological Sciences)

THE UNIVERSITY OF BRITISH COLUMBIA

(Vancouver)

December 2019

© David Sasse, 2019

The following individuals certify that they have read, and recommend to the Faculty of Graduate and Postdoctoral Studies for acceptance, a thesis entitled:

Attrition of mantle cargo during kimberlite ascent: Insights from analogue experiments

submitted by David Sasse in partial fulfillment of the requirements for

the degree of Master of Science

in Geological Sciences

Examining Committee:

James Kelly Russell, Geological Sciences
Supervisor

Thomas Jones, Geological Sciences
Supervisory Committee Member

Maya Kopylova, Geological Sciences
Supervisory Committee Member

Lucy Porritt, Geological Sciences
Additional Examiner

Abstract

Kimberlite magmas transport mantle cargo in the form of xenoliths and xenocrysts to the surface of the Earth. Due to the lack of recent kimberlite eruptions and unanswered questions concerning melt composition and magma rheology, the mechanisms supporting efficient ascent of these cargo-rich magmas remains enigmatic. Although olivine is the dominant mineral phase in kimberlite, given the polymineralic nature of mantle xenoliths, xenocrysts are transported as a multi-mineral mixture. Within the ascending dyke, high particle concentrations and high velocities resulting in turbulent flow provides an environment for frequent particle-particle interaction. Xenocryst morphologies, textures and size distributions observed in kimberlite deposits are not reflective of how they occur in xenoliths and are therefore modified during ascent to the surface. The degree of modification of each mineral varies and is a function of its chemical and physical properties. Here I present a series of analogue attrition experiments on the mantle minerals: olivine, orthopyroxene, clinopyroxene, garnet and diamond designed to inform on the ascent of kimberlite magmas. Data is collected on particle size distributions, particle morphologies and particle velocities. Natural xenocrysts extracted from coherent kimberlite reveal remarkably similar surface features and morphologies to that of the experiments suggesting that attrition indeed operates during kimberlite ascent. Kimberlite ascent velocities are estimated by using a scaling analysis of the experiment conditions and by investigating impact pits observed on the surfaces of kimberlitic olivine and garnet xenocrysts. Both methods result in calculated ascent velocities of ~ 4 m s^{-1}. In mineral mixtures, cleavage is shown to be a controlling factor in determining attrition rates whereby minerals with cleavage undergo accelerated breakdown. I suggest that the accelerated breakdown of orthopyroxene increases assimilation rates, contributing to the onset of turbulent ascent.

Lay Summary

Anyone who has walked along a beach, or a dry stream bed will have at some point observed the remarkably well rounded and polished pebbles. These shapes and textures are the result of low energy collisions over long periods of time.

Kimberlite is a rock type well known for being the major global source of diamonds. The magma that goes on to form the rock, kimberlite, originates deep in the Earth's interior and picks up mantle rocks and minerals on its way to surface. The mantle material observed in kimberlites is often anomalously well rounded and just like the pebbles in a stream, began as angular fragments. This study aims to better understand the processes that lead to the observed morphologies in kimberlite and to gain insight into the conditions present during the ascent of kimberlite magma towards the surface.

Preface

This thesis was completed under the supervision of Dr. Kelly Russell and Dr. Thomas Jones who collectively designed the project, offered direction and helped with editing. This dissertation is original, unpublished, independent work by the author, Sasse. D. The project was completed as a requirement of the NSERC CREATE program: Diamond Exploration and Research Training School (DERTS).

Table of Contents

Abstract ..... **iii**

Lay Summary ..... **iv**

Preface ..... **v**

Table of Contents ..... **vi**

List of Tables ..... **ix**

List of Figures ..... **xi**

List of Symbols ..... **xvii**

Acknowledgements ..... **xix**

Chapter 1: Introduction **1**

Chapter 2: Background on Attrition **6**

2.1 Particle Attrition Mechanisms and Applications 6

2.2 Applications in Engineering 9

2.2.1 Applications in Chemical Engineering 9

2.2.2 Applications in Mining 11

2.3 Attrition in Geological Environments 13

2.4 Applications in Volcanology 14

2.5 Attrition in Kimberlites 17

Chapter 3: Attrition Apparatus for Experiments **23**

3.1 Modifications to the Attrition Apparatus 25

3.2 Experimental Conditions 26

3.3 Scaling the Experiments to the Natural System 29

3.4 Data Collection During and After Experiments 30

3.5 Experimental Grid 34

Chapter 4: Sample Characterization.....36

4.1 Sample Characterization 36

4.1.1 Density Measurements 36

4.1.2 2D Shape Characterization 38

4.1.3 Scanning Electron Microscopy 40

4.1.4 Summary of Experiments Chosen for Analysis 40

4.1.5 Mineral Properties Summary 42

Chapter 5: Results and Analysis.....43

5.1 Attrition of Individual Minerals 43

5.1.1 Fines Production Datasets 43

5.1.2 Grain Size Distributions 49

5.1.3 Experiment Observations / Videography 52

5.1.4 Grain Shapes and Surfaces 58

5.2 Attrition of Mineral Mixtures 72

Chapter 6: Discussion 75

6.1 Transport Duration and Velocity of Kimberlite Ascent 75

6.2 Morphology and Surface Features of Coherent Kimberlite Xenocrysts 79

6.3 Mineral Physical Properties Related to Attrition Susceptibility and Mechanisms 84

6.4 Attrition Mechanics 86

6.4.1 Abrasion Mechanics 87

6.4.2 Fragmentation Mechanics 93

6.5 Implications of Multiphase Mineral Mixtures in Nature 94

Chapter 7: Conclusion 97

References.....99

Appendices 115

Appendix A Experiment Apparatus 115

A.1 Experiment Apparatus Photograph.....115

Appendix B Mineral Supplementary Information 116

B.1 Photographs of Minerals Used in This Study.....116

B.2 Mineral X-Ray Diffraction Analysis 117

Appendix C Select Datasets Analyzed.....119

C.1 Grain Size Distribution Datasets 119

Appendix D University of Alberta Diavik Xenolith Analysis.....132

D.1 Morphology Measurements of Select Eclogite and Peridotite Xenoliths.....132

D.2 3D Laser Scanner Methods 134

Appendix E MATLAB Shape Script 135

Appendix F Physical Mineral Property References Used 138

List of Tables

Table 2-1. Observations and interpretations of rounded xenoliths from kimberlite in the literature.....21

Table 3-1. The calculated superficial velocity present within different areas of the attrition apparatus at different gas fluxes. Highlighted conditions are those used in this study.....28

Table 3-2. Mastersizer settings used for each mineral. 34

Table 3-3. Experimental grid showing the 49 experiments performed in this study. X denotes that an experiment was performed at the noted time. Series 1, 2, 3, 4, 5 are single mineral experiments on the minerals olivine, orthopyroxene, clinopyroxene, garnet and diamond respectively. Series 6 and 7 are mineral mixture experiments with series 6 representing an olivine-garnet mixture and series 7 representing an olivine-clinopyroxene mixture.....35

Table 4-1. Reported densities obtained for each mineral. 37

Table 4-2. Post-experiment measurements of run products for each experiment. X represents measurements which were completed for each experimental series. 42

Table 4-3. Summary of physical properties of all minerals analyzed in this study 42

Table 5-1. Table of masses (g) recorded for each experiment: m_0 is the initial mass, m_r is the total mass recovered after the experiment, m_d is the mass of daughter products and m_l is the difference between the starting and the recovered mass. 44

Table 5-2. Table of model fit parameters for each mineral series. RMSE = Root Mean Square Error. 48

Table 5-3. Height data collected from each experiment. h_0 is the initial bed height, h_p is the height of the column and φ, a metric for particle concentration is calculated as h_0/h_p. 53

Table 5-4. Particle tracking results for each mineral: n, the number of particles tracked, the average of the absolute value of all particle velocities (v_{ave}), the mode velocities of the histogram data (v_{mode}) presented in Figure 5-5b, differential velocity (Δv) which is approximated by taking the difference between the two peak velocities and maximum differential is taken as the range of the histogram distribution.....57

Table 5-5. Table summarizing the change in circularity (C), solidity (S) and convexity (C_{vx}) for each mineral from 0 h to 24 h.....63

Table 5-6. Sieve fraction sizes (µm) selected for SEM imagery of daughter particles.....69

List of Figures

Figure 1-1. Rounded mantle cargo from various kimberlite localities. a) Olivine macrocrysts from a coherent lava flow, Igwisi Hills, Tanzania. b) Various types of xenoliths present in coherent kimberlite from West Greenland. c) Photomicrograph (xpl) of rounded olivine from the A154N pipe, Diavik, NWT. d) Hand sample of olivine macrocryst rich coherent kimberlite, Diavik, NWT. e) Left: Eclogite xenolith from Diavik, right: Cut eclogite xenolith from West Greenland. 2

Figure 1-2. (not to scale). Ascent path of a kimberlite magma adapted from Jones et al. (2019). Inset shows a stratified kimberlite dyke wherein the mantle is sourced at the crack tip and milled in a turbulent, fluid rich suspension. The mantle cargo then settles and is preserved in the magma tail of the dyke. 4

Figure 2-1. Schematic illustrating attrition mechanisms and resulting grain size distributions. Fragmentation is a high energy process leading to wholesale breakage of particles into smaller daughter particles of similar sizes. Abrasion is a less energetic process involving chipping of surface asperities on the parent grains creating ultrafine daughter products.....7

Figure 2-2. Grain size evolution of particles undergoing attrition. Time 0: Particles have a narrow distribution and one mode. Time 1: A proportion of parent material is converted into fragmented and abraded daughter products. Time 2: The particle size distribution remains stable as there is not enough energy to further modify the particles. 8

Figure 2-3. Schematic of an ASTM jet attrition apparatus modified from Jones et al. (2017) 10

Figure 2-4. a) Angular olivine phenocryst imaged by Jones et al. (2014). b) Rounded and polished olivine sand grain from Punalu'u Black Sand Beach, Hawaii.....13

Figure 2-5. A) Attrition of mantle cargo after being picked up by the ascending dyke. B) Abrasion of xenoliths as they collide with themselves and dyke walls during settling. C) High energy disruptive collisions of juvenile volcanic clasts. Xenolith wall rocks are fluidized and milled in the particle rich gas jet. D) Lower energy collisions take place in the plume resulting in attrition primarily by abrasion and secondary ash production. E) Particles are fluidized in pyroclastic density currents where rounding takes place through abrasion. 16

Figure 2-6. Stratified kimberlite dyke modified from Brett et al. (2015). Xenoliths are sampled by the crack tip into the fluid/gas rich head of the dyke where they are disaggregated and the liberated xenocrysts are milled. They then settle into the volatile-poor tail where they are preserved.....18

Figure 2-7. a) Gas velocity (U_g) is much greater than the terminal settling velocity (U_t); xenoliths are elutriated. b) Gas velocity falls between the minimum fluidization velocity (U_{mf}) and elutriation velocity; xenoliths are fluidized and milled in the gas jet. c) Gas velocity is much less than minimum fluidization velocity; xenoliths are unable to become fluidized.....20

Figure 3-1. a) Schematic diagram of attrition apparatus used in this study. Inset shows sample resting on distributer plate and fluidized by the gas jet (solid arrow). b) Distributor plate components.....24

Figure 3-2. Minimum fluidization and elutriation velocities of olivine. Green marker represents the starting conditions of 105 L min^{-1} gas flux (1.8 m s^{-1} in the attrition tube) and 610-710 µm (655 µm mean) used for all experiments. Shaded region represents region of fluidization possible for attrition experiments on olivine. Parameters used: ρ_g = 1.225 kg m^{-3}, ρ_p = 3246 kg m^{-3}, μ = 1.82 × 10^{-5}, ε = 0.58, ϕ = 1.....28

Figure 3-3. Cartoon illustration of data collected during an experiment. h_0 is the initial bed height, h_p is the height of the fluidized column. Select experiments of each mineral were filmed using a high-speed camera and a strobe light. The height of the strobe light (h_l) and the height of the camera (h_c) changed for each mineral. 31

Figure 3-4. Experimental flow regimes in the attrition apparatus taken from Jones et al. (2019). 33

Figure 4-1. Mass plotted against volume for three aliquots measured of each mineral. A linear curve is fitted through the data points and the origin to obtain the best approximation of density. 37

Figure 4-2. a) An image of a garnet grain taken with the binocular microscope. b) The grain thresholded and converted to binary. 38

Figure 4-3. Visualization of parameters used to quantify shape metrics from Campbell (2012). 39

Figure 5-1. Mass loss (m_l) plotted against time for each mineral series. Uncertainty is represented as one relative standard deviation obtained from repeating experiment 1-F three times. 45

Figure 5-2. a) Proportion of daughter products (m_d) normalized to the mass recovered (m_r) plotted against time for each mineral series. Experiment 1-F is highlighted as it is used to calculate relative standard deviation. b) Model values of *a*, the infinite time limit of attrition and *b*, the attrition rate constant for all minerals. The ellipses represent 95% confidence envelope based on the fit of equation 5-1 to the data. 47

Figure 5-3. Grain size distributions for each mineral series: (a) Olivine; (b) Orthopyroxene; (c) Clinopyroxene; (d) Garnet; (e) Diamond. The starting (input) distribution is shaded in grey and the experiment run products are plotted as continuous lines which become darker with increasing

experiment duration. Insets show the finer daughter products, measured by laser particle size analysis (LPSA), at an enlarged scale. For the readers ease the diamond inset y-axis scale is an order of magnitude lower than the other plots to account for the low abundances of diamond daughter products. The complete particle size dataset can be found in Appendices C.1-C.5.....51

Figure 5-4. a) Column height (h_p) plotted against mineral density for each mineral. b) Particle concentration (φ) plotted against density for each mineral. Symbology is consistent with that used in previous figures.....54

Figure 5-5. Particle tracking results for a) olivine, b) orthopyroxene, c) clinopyroxene, d) garnet, e) diamond. Left: Raw particle velocity values for each particle tracked. Center: Velocity values plotted as histograms with 0.2 m s^{-1} bin width. Right: Velocity distribution within the attrition tube, y is the distance above the base of the tube (mm) and x is the distance across the tube.....56

Figure 5-6. Representative parent particle binary images for each mineral at select experiment durations ranging from 0 h to 24 h. Note that no experiment was conducted at 0.5 h for orthopyroxene.....58

Figure 5-7. a) Solidity, b) Convexity, c) Circularity plotted against time (h). Colors and symbology are consistent with previous figures.....62

Figure 5-8. Axial ratio (A) plotted against circularity (C) for olivine (green) and orthopyroxene (yellow). Marker size is proportional to experiment duration, larger symbols denote longer experiments. Colors and symbols are consistent with previous figures. Representative binary images of the experiments are shown for reference.....64

Figure 5-9. SEM images (in Secondary Electron mode) of representative parent particle morphology at select experiment durations. Rows represent different minerals and columns denote experiment duration. 65

Figure 5-10. SEM images of representative parent particle surfaces at select experiment duration. Rows represent different minerals and columns denote experiment duration. 66

Figure 5-11. Left: Smaller scale impact features (< 20 µm) associated with surface roughness. Right: Arrows pointing at larger impact features (> 100 µm) interpreted to result from higher energy collisions. 68

Figure 5-12. Daughter products from individual sieve fractions (see Table 5-6) for each mineral for the shortest experiment times. Rows show sieve fraction size and columns show mineral type. All images taken at 0.5 h except Opx whose shortest experiment is 2 h. Sieve fractions are classified by formation: Abraded parent particles, fragmentation products and abrasion products. Opx was found to have both fragmented parent and abraded parent particles in the 300 – 355 µm bin.....70

Figure 5-13. Daughter products from mode sieve fractions for each mineral for the longest common experiment duration of 24 h. Shading is consistent with that in Figure 5-12. 71

Figure 5-14. Ratio of daughter particles to the total (m_d / m_r) against time for a short (2 h) medium (6 h) and long (24 h) duration. Circles represent the m_d / m_r bulk mixture and triangles the m_d / m_r of the individual minerals obtained from separating the minerals from the bulk mixture. Solid lines are for the single mineral experiments taken from Figure 5-2 and dashed lines are an average of these two curves. The bulk mixture should plot along the predicted dashed line if the attrition rates and limits do not change for each mineral. 73

Figure 6-1. a) Mineral series attrition curves where the x-axis is converted to distance using calculated ascent velocities. b) Olivine curves from Jones et al. (2019) showing the effects of changing input mass and gas flux. 78

Figure 6-2. Morphology and surface features of clinopyroxene, garnet and olivine grains extracted from Diavik coherent kimberlite compared with experiment products. 80

Figure 6-3. Comparison of chemical and mechanical surface features on natural Diavik xenocrysts of olivine, clinopyroxene and garnet. Olivine: Left: dissolution feature showing straight edges. Right: hemispherical impact pit overprinting a rough surface. Clinopyroxene: Left: Globular formations on exposed cleavage planes. Right: Cleavage controlled breakage. Garnet: Left: layer of fibrous kelyphite rim on garnet. Right: conchoidal fractures from repeated impacts.....82

Figure 6-4. a) Left: diamond showing equant tetragonal pits. Right: Inset highlighting difference between impact pit and trigon. b) Left: Rough edge of an attrited diamond with one surface showing cleavage-controlled breakage and another surface with trigons. Right: Inset of trigons. 83

Figure 6-5. Model *a* and *b* values plotted against mineral physical properties where *H* is hardness, K_c is fracture toughness, γ is the fracture surface energy and Y is the Young's modulus. 85

Figure 6-6. Impact pit example are outlined in yellow dashed lines for olivine and garnet on the surface of Diavik xenocrysts. Solid yellow lines show the measurement taken for the impact pit diameter. 90

Figure 6-7. Lines showing relationship between impact velocity and pit size for different size grains of a) olivine and b) garnet. Pit sizes were measured for two grains of olivine and two grains of garnet from Diavik (dashed curves show sizes of grains). The average velocities were computed from the average pit diameters (vertical and horizontal dashed lines). The shaded regions denote total range.....92

List of Symbols

a	attrition model time limit
a_{image}	minor axis
A_{CH}	convex hull area
A_{image}	area of binary image
b	attrition model rate
b_{image}	major axis
C	circularity
C_{vx}	convexity
d_p	particle diameter
D	dyke diameter
F	normal compressive force
g	acceleration due to gravity
h_c	height of camera
h_f	fountain height
h_l	height of strobe light
h_p	pneumatic column height
$h_{0\ calc}$	initial calculated bed height
$h_{0\ meas}$	initial measured bed height
H	hardness
i	impact pit diameter
k	material proportionality constant
K_c	fracture toughness
l	crack length
L	attrition tube diameter
m_d	mass of daughter particles
m_l	mass loss
m_r	recovered mass
m_0	initial mass
n	number of peaks
$P_{ellipse}$	elliptical perimeter
P_{image}	perimeter
Re	Reynolds number
Re_{exp}	Reynolds number of experiments
Re_k	Reynolds number of kimberlite magma
s	slip ratio
S	solidity
t	time
U	superficial velocity

U_g	superficial gas velocity
U_{mf}	minimum fluidization velocity
U_t	terminal settling velocity
v	dyke ascent velocity
v_{ave}	average velocity
v_{mode}	mode velocity
v_{p}	particle velocity
v^*	bulk velocity
Y	Young's modulus
α_c	material chipping proportionality factor
α_w	material wear proportionality factor
Δs	sliding distance
Δv	average differential velocity
ε	void fraction
γ	fracture surface energy
μ	viscosity
μ^*	bulk viscosity
ϕ	particle sphericity
φ	particle concentration
φ_{Jones}	particle concentration by Jones et al. (2019)
ρ	magma bulk density
ρ_{g}	gas density
ρ_{p}	particle density
ρ^*	bulk density
σ_f	stress of crack propagation
σ_{im}	stress from impact
ζ_{chip}	breakage by chipping
ζ_{wear}	breakage by wear

Acknowledgements

I would like to firstly thank my supervisor Kelly Russell and co-supervisor Tom Jones for their invaluable guidance over the past 2 years. Kelly, I greatly admire your curiosity of the natural world and eagerness to explore unchartered areas in research. Since starting this project, I have become a much better scientist, public speaker and writer, all of which is owed to your mentorship. I am very proud to have been part of your lab group. Tom, this project would not have been possible without your continuous insights and direction. You have taught me everything I know about analogue experimentation and attrition and have always been patient with me no matter how trivial my questions may be. I am very grateful that you always set time aside time for my research regardless of the time zone. Most importantly, in addition to being a great teacher, you have become a good friend of mine.

I would also like to thank my third committee member, Maya Kopylova for teaching me so much about kimberlites. Maya your willingness to facilitate scientific discussion in the kimberlite community through the Vancouver Kimberlite Cluster (VKC) is admirable and I am thankful for the opportunity you gave me to host the conference over the past 2 years.

Many thanks to all my Volcanology and Petrology lab mates for making the lab environment so amazing. The insightful discussions have been incredibly helpful. Special thanks to Amy Ryan for training me on so much lab equipment and always being eager to hear what I'm up to in my research.

I would like to thank my family for always being supportive of my decisions and offering continuous encouragement.

Lastly, I would like to extend my gratitude to my partner, Jeanne who has been with me and given me unconditional support and motivation every step of the way. She has always helped

me see the positive side of things and given me the courage to be my best self. I also thank her for her help with the tedious work of crushing and sorting minerals.

I acknowledge and am grateful for the financial support of the NSERC CREATE program: Diamond Exploration and Research Training School (DERTS) whose funding made this project possible.

Chapter 1: Introduction

Kimberlites are bodies of volcanic rock preserved as shallow pipes, sheets, dykes and sills across cratons (Brown et al., 2007; Brown and Valentine, 2013; Dawson, 1971; Kavanagh and Sparks, 2011), notable for their diamond bearing potential. The low viscosity, volatile rich parental magmas which form kimberlites originate deep within the Earth, in excess of 150 km and ascend towards the surface at anomalous speeds estimated between 1 and 20 m s^{-1} (Russell et al., 2012; Sparks et al., 2006; Wilson and Head, 2007). Transit through the cratonic mantle to the surface occurs on the scale of hours to days (Sparks et al., 2006) during which the magma samples and entrains xenoliths and xenocrysts. The transported mantle cargo can comprise ~ 50% volume (Holden et al., 2009; Moss et al., 2010; Scott Smith, 2008) of the final rock. Many of the xenocrysts, especially olivine, and xenoliths are commonly observed to be rounded and ellipsoidal in shape (Arndt et al., 2006, 2010; Jones et al., 2014; Peltonen et al., 2002; Peterson and Lecheminant, 1993; Smith and Griffin, 2005)(Figure 1-1). Importantly, mantle xenocrysts have initial size distributions, shapes and textures which change during transport within kimberlite magmas. Hence, the mineral sizes, shapes and surface features are fingerprints of the transport conditions and provide unique data which can be utilized to inform on the mechanisms, rates and timescales attending to kimberlite ascent.

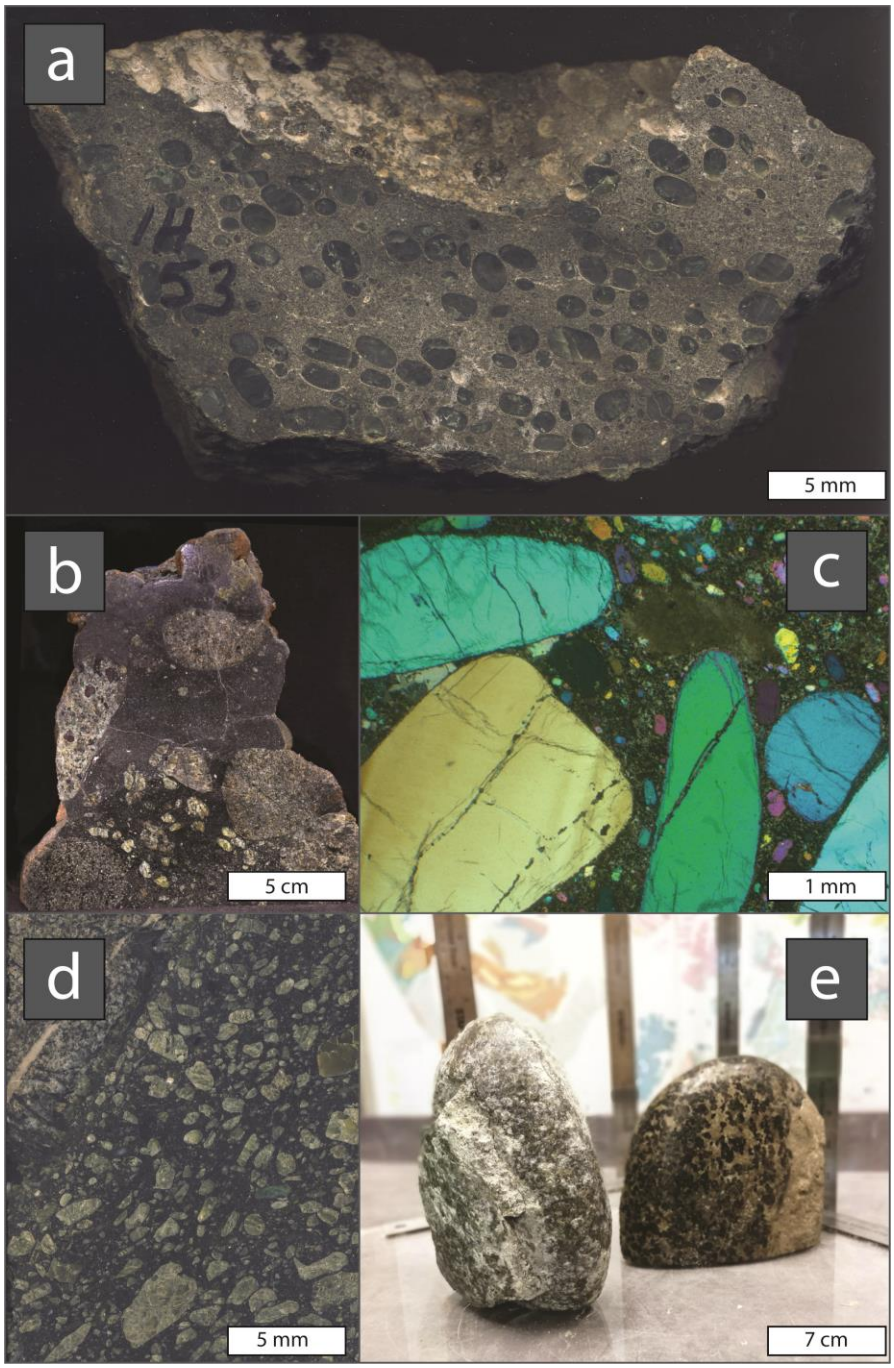

Figure 1-1. Rounded mantle cargo from various kimberlite localities. a) Olivine macrocrysts from a coherent lava flow, Igwisi Hills, Tanzania. b) Various types of xenoliths present in coherent kimberlite from West Greenland. c) Photomicrograph (xpl) of rounded olivine from the A154N pipe, Diavik, NWT. d) Olivine macrocryst rich coherent kimberlite, Diavik, NWT. e) Left: Eclogite xenolith from Diavik, right: Cut eclogite xenolith from West Greenland.

Kimberlites make their way to the surface in dykes (Figure 1-2). During the ascent, the overlying mantle is fractured due to over-pressures created by the magma buoyancy (Kavanagh et al., 2018; Russell et al., 2012; Sparks et al., 2006), causing wall rocks to be entrained into the leading tip of the kimberlite dyke. The xenoliths are then subject to rapid depressurization, causing their disaggregation and subsequent release of xenocrysts into the fluid rich head of the stratified kimberlite dyke (Figure 1-2). This turbulent, low viscosity environment provides ideal conditions for particle-particle interactions herein termed attrition (Brett et al., 2015; Jones et al., 2019, 2014; Jones and Russell, 2018; Russell et al., 2012; Sparks et al., 2006). Attrition has been suggested as a dominant process in numerous volcanic systems including: rounding of pumice clasts within pyroclastic density currents (Dufek and Manga, 2008; Jones et al., 2016; Kueppers et al., 2012; Manga et al., 2011), milling of accessory lithic xenoliths within volcanic conduits (Campbell et al., 2013; Mellors and Sparks, 1991; Nairn et al., 1994), transport and eruption of mantle xenoliths (Arndt et al., 2010; Peltonen et al., 2002; Peterson and Lecheminant, 1993; Smith and Griffin, 2005), and secondary production of fine ash particles (Jones and Russell, 2017). These studies have demonstrated that transported cargo is efficiently resized and shaped under turbulent conditions, and that the properties of attritted particles provide a powerful tool to inform on the conditions present during transport.

Here I build upon the work of Jones et al. (2019) and present a series of novel attrition experiments on select mantle minerals to better understand attrition during kimberlite dyke ascent. To do this, data is collected during and after the experiments which informs on the size distributions, shapes, morphologies, surface textures and particle velocities. I use these data as a unique tool to inform on conditions, timescales and velocities attending to kimberlite ascent, and discuss the implications of a multiphase mineral system present in kimberlite magmas.

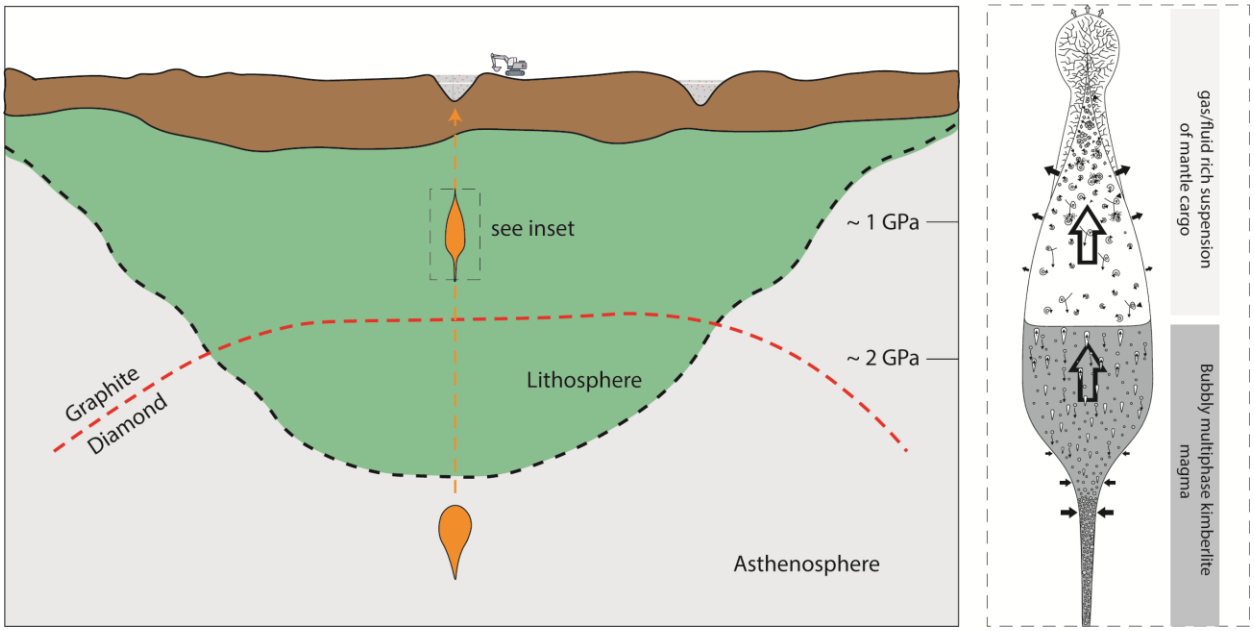

Figure 1-2. (not to scale). Ascent path of a kimberlite magma adapted from Jones et al. (2019). Inset shows a stratified kimberlite dyke wherein the mantle is sourced at the crack tip and milled in a turbulent, fluid rich suspension. The mantle cargo then settles and is preserved in the melt rich tail of the dyke.

Attrition studies in volcanic regimes is relatively limited and therefore much is still unknown. This work greatly broadens our understanding of this mechanism in kimberlites and should be used towards building a comprehensive model of kimberlite ascent dynamics.

The following chapters of the thesis are structures as follows:

- Chapter 2 contains background information on attrition, which consists of an overview of the mechanisms attending to the process as well as a comprehensive literature review.
- Chapter 3 shows the methods utilized to perform the experiments. This includes the design of the modified attrition apparatus and how experiment conditions were chosen.

The filming of particle-particle interactions using high speed videography is discussed as well as how grain size distributions were determined.

- Chapter 4 contains the methods used to characterize the experiment samples (pre and post experiment). This includes the process of characterizing the sample grain morphologies both qualitatively and quantitatively. A table of mineral physical properties used throughout the thesis is found at the end.
- Chapter 5 presents the results from the experiments and applies an empirical model used to quantify attrition rates and limits of each mineral. Results of experiments incorporating mineral mixtures are also presented and compared to the single-mineral experiments.
- In Chapter 6 a scaling analysis is performed in which kimberlite ascent velocities are calculated and mass loss relationships from each mineral experiment are related to kimberlite ascent. Morphologies and textures of minerals produced from the experiments are then compared to that observed in the Diavik kimberlite deposit. Textures produced by chemical and mechanical processes are discussed which is used to interpret the processes operating during kimberlite ascent. Next, the physical properties of the minerals are related to attrition rates and limits and any relationship or lack thereof is discussed. Lastly, the mechanisms of attrition are explored and a model relating impact pit diameters to impact velocity is constrained by experiment data and applied to xenocrysts from the A154N Diavik kimberlite pipe.
- Finally, Chapter 7 concludes by reviewing the findings of this research and summarizes the implications for kimberlite ascent dynamics.

Chapter 2: Background on Attrition

2.1 Particle Attrition Mechanisms and Applications

Attrition has two primary modes (Jones et al., 2017; Tardin et al., 2001; Xiao et al., 2011): abrasion and fragmentation (Figure 2-1). Abrasion is a relatively low energy process that causes wearing of surface asperities, subsequently rounding the grain by releasing fine particles and surface chips (Bemrose and Bridgwater, 1987; Jones et al., 2017; Xiao et al., 2011). The particle size distribution of parent particles is only weakly modified (Figure 2-1) whilst a fine daughter population is produced. On the microscale, abrasion is associated with plastic deformation and yield at the surface of the grain (Bayham et al., 2016; Hutchings, 1993; Scala, 2013), releasing ultrafine particles and in the case of surface chipping, brittle failure in which a fracture propagates from the site of impact, extending laterally and curving towards the surface, releasing small chips.

Fragmentation is a more energetic process in which a fracture propagates internally leading to the formation of fragments that are roughly the same order of magnitude in size as the original grain (Bemrose and Bridgwater, 1987; Ghadiri and Zhang, 2002; Jones et al., 2017; Xiao et al., 2011). In this case, the size distribution changes such that an intermediate peak develops representing the fragmented daughter products (Figure 2-1).

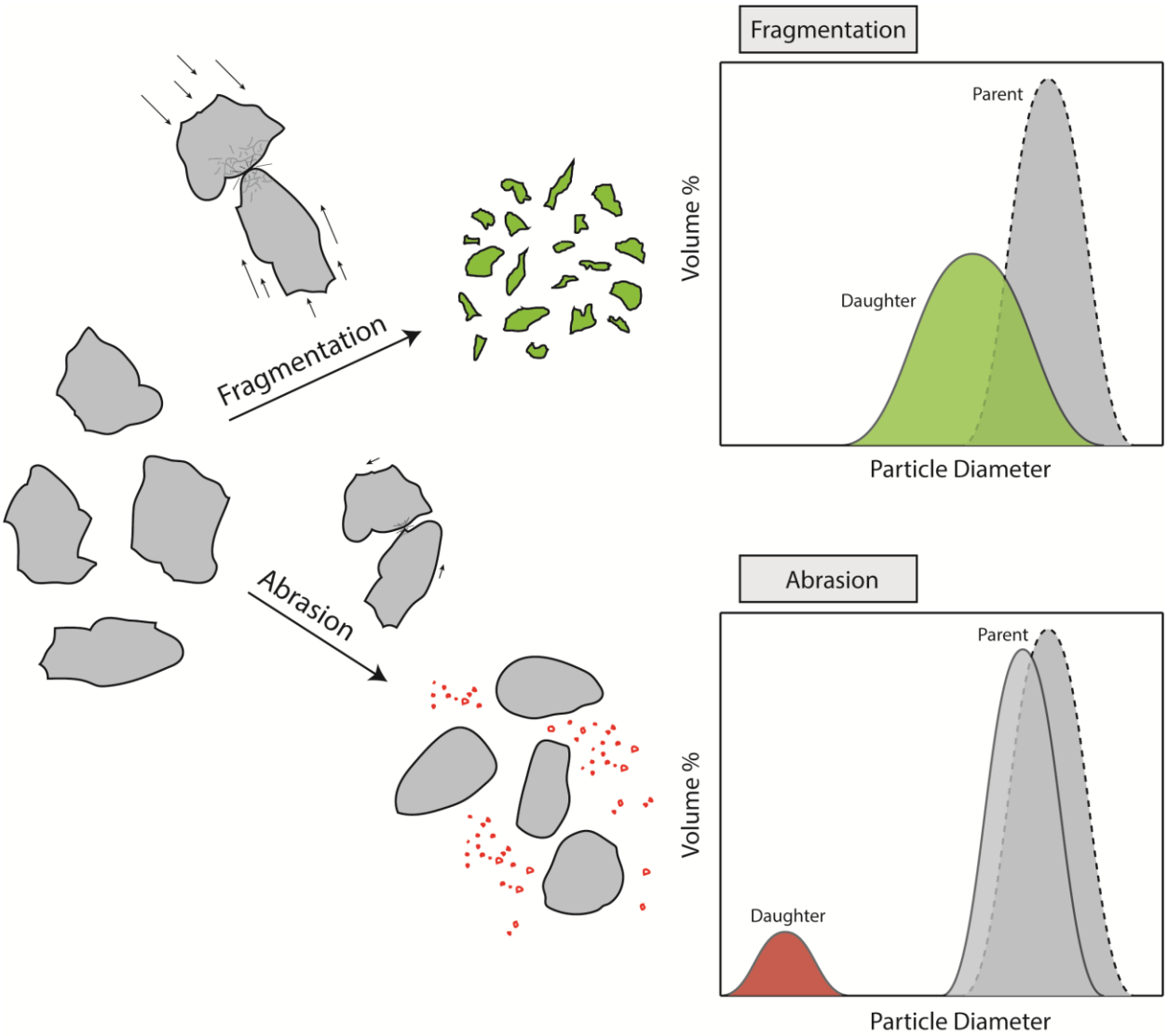

Figure 2-1. Schematic illustrating attrition mechanisms and resulting grain size distributions. Fragmentation is a high energy process leading to wholesale breakage of particles into smaller daughter particles of similar sizes. Abrasion is a less energetic process involving chipping of surface asperities on the parent grains creating ultrafine daughter products.

Griffith (1921) showed that materials fail by crack propagation when energetically favorable, that is when energy released by relaxing the strain is greater than the energy of the newly formed surface. Implicit in the theory is that larger particles will achieve fragmentation

under lower energy conditions, as a larger crack length requires a lower critical stress. The implication is that under relatively constant or waning energy conditions, particles undergoing attrition will initially fragment until the size is reduced such that fragmentation is no longer energetically favorable (Figure 2-2). From this point only abrasion operates, rounding the particles until all surface asperities are removed (Figure 2-2).

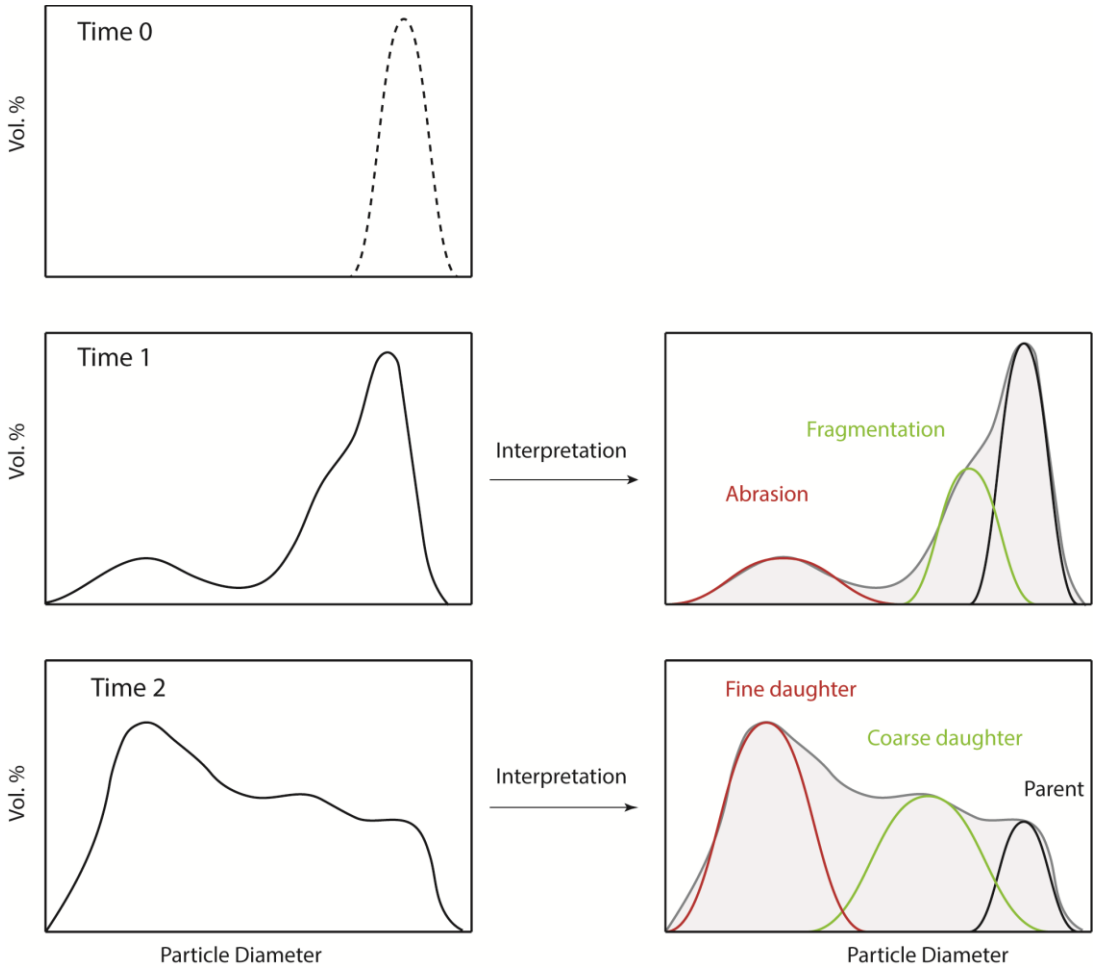

Figure 2-2. Grain size evolution of particles undergoing attrition. Time 0: Particles have a narrow distribution and one mode. Time 1: A proportion of parent material is converted into fragmented and abraded daughter products. Time 2: The particle size distribution remains stable as there is not enough energy to further modify the particles.

2.2 Applications in Engineering

2.2.1 Applications in Chemical Engineering

Attrition of particles has been extensively studied mainly for applications in fluidized bed systems to promote enhanced contact between gases and solids. Industrial applications of fluidized beds include but are not limited to: fluidized bed reactors (multiphase chemical reactions), fluid catalytic cracking (FCC) used in petroleum refineries, drying and cooling of particulate matter, spray granulation, and CO_2 and SO_2 capture (Abanades et al., 2004; Knight et al., 2014; Pacciani et al., 2008; Sun et al., 2007) .

Numerous types of apparatus exist to test the attrition susceptibility of materials, including: jet cup attrition (Cocco et al., 2010), cyclone attrition (Reppenhagen and Werther, 2000), impact attrition (Chen et al., 2007) and more commonly, jet attrition in fluidized beds (Jones et al., 2017; Werther and Xi, 1993a; Xiao et al., 2012). The basic components of a laboratory scale standard (ASTM) fluidized bed used for chemical engineering studies include (Figure 2-3): A distributer plate which the gas enters through, a primary attrition tube where the particle collisions take place, a settling chamber to promote recycling of particles back into the attrition tube and a fines collection filter system where elutriated ultrafine (micron scale) particles accumulate.

As the gas flux is turned on to a critical value, the drag force exerted by the flow exceeds the downward force of gravity and the particles become fluidized, allowing for particle-particle interactions. If there is enough energy, particles will undergo fragmentation and abrasion processes, resizing the particle population. Several factors constitute the efficiency of attrition in the fluidized bed, which can be broken down into environmental factors and material properties

(Bemrose and Bridgwater, 1987; Boerefijn et al., 2007; Forsythe and Hertwig, 1949; Jones et al., 2017; Werther and Xi, 1993b). Environmental factors include the experimental controls such as residence time in the air jet, gas type, temperature, pressure, particle load and gas velocity. Material properties governing attrition include grain size, hardness, toughness, density, shape and texture.

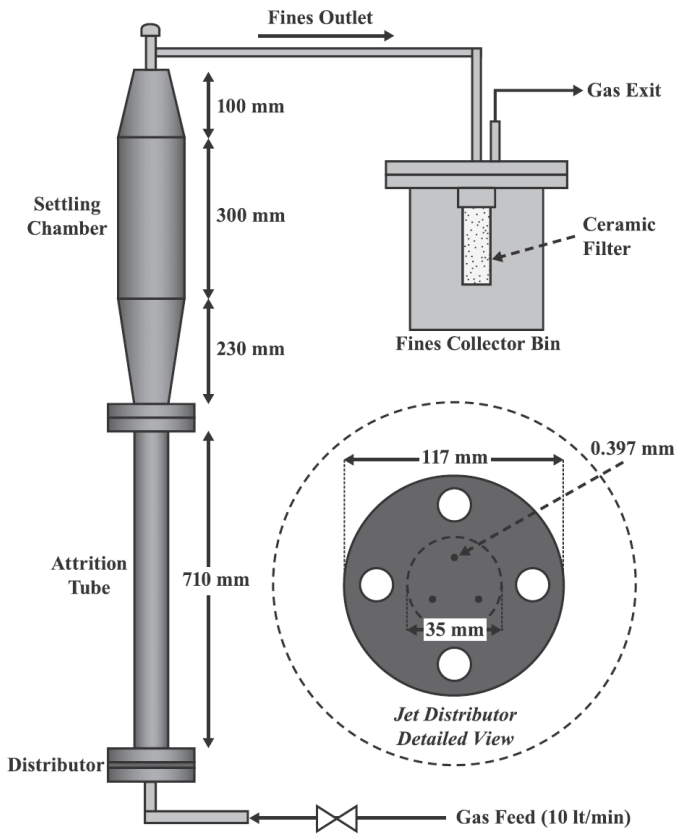

Figure 2-3. Schematic of an ASTM jet attrition apparatus modified from Jones et al. (2017)

Chen et al. (2007) investigated the effect of temperature on limestone attrition using an impact apparatus and observed reduced attrition with higher temperatures. This was explained by a change in the bulk material properties (Young's modulus, tensile strength, etc.) with a change in temperature. Xiao et al. (2014) used Entropy of Information (EOI) as a metric to predict the

attrition susceptibility of starting grain size distributions. Larger particles and wider starting size distributions were calculated to have a larger EOI and consequently a higher initial attrition rate. Kim et al. (2019) studied the effects of material properties on attrition in binary mixtures using iron and limestone particles. They found that both limestone and iron underwent increased attrition in the mixture in comparison to the single-phase experiments. Across all attrition studies in the literature, regardless of the materials used, the dominant pattern in the experiment data is a rapid decay in the attrition rate with increased residence time (Gwyn, 1969; Jones et al., 2017; Kang et al., 2017; Xiao et al., 2012).

2.2.2 Applications in Mining

In the pretreatment processing of ore, the first step involves the size reduction of solid material by grinding, crushing or other processes. In the mining industry, this process is typically referred to as comminution (Napier-Munn and Wills, 2005; Wills and Napier-munn, 2006). During this physical processing stage, all modes of fracture (compressive, tensile and shear) can be discerned depending on the type of comminution device. During crushing (compression), coarse daughter particles result from tensile failure and fine particles are produced by either shear stress or compressive failure at the point of loading (Napier-Munn and Wills, 2005). In a rapid impact loading event (ball mill) a particle will experience a high stress and undergo significantly more strain than necessary to achieve a simple fracture, resulting in rapid breakage by tensile failure (Fuerstenau and Abouzeid, 2002; Sadrai, 2007). If, however, impact energy is not greater than the particle yield stress, fracture occurs predominantly through chipping, where edges are broken away from the particle (Fulchini et al., 2019; Ghadiri and Zhang, 2002). In milling devices (stirred mills in particular), particle-particle attrition often becomes the most

significant breakage process (Gupta and Yan, 2016). This results in a high proportion of ultrafine particles through surface abrasion, in which shear stress causes surface wear. This byproduct may or may not be desirable depending on the industry sector and stage in the comminution cycle.

Comminution of ore material is an energy intensive process which consumes the largest amount of energy in the mining process, estimated between 30% and 70% of total energy expenditure (Nadolski et al., 2014; Radziszewski, 2013; Sadrai et al., 2006). With the efficiency of commination typically below 5% (Tromans, 2008), a large body of research is focused at better understanding the energy requirements for ore/mineral breakage (Nadolski et al., 2014). A common approach to determine the energy efficiency of comminution is to compare the energy input with the energy of the new surface ("required energy") created, calculated by multiplying the new surface area (m^2) by the specific surface energy in J m^{-2}. Using this approach, energy efficiency can be as low as 1% (Radziszewski, 2013). Adopting this method, Sadrai et al. (2006) performed a series of high velocity (50-300 m s^{-1}) impact experiments on limestone, quartz and rock salt, measuring energy efficiency as a ratio of energy consumed (kinetic energy of the particle) to energy produced. The results showed that breakage at high velocities can be as much as 200-300% more efficient than low impact devices such as tumbling mills. Nadolski et al. (2014) investigated the threshold energy required to break three ore types at a range of particle sizes using single-particle compression breakage. An energy efficiency benchmark was determined by dividing the actual energy consumed by the energy required for breakage.

2.3 Attrition in Geological Environments

In sedimentology the term maturity is used to describe the degree of sorting and rounding resultant of the weathering process during transport. “Immature” is used to describe clasts with a high degree of angularity and a broad grain size distribution. These clasts are relatively young and angular and have undergone little movement from their source. “Mature” clasts in contrast have a narrow grain size distribution and a high degree of rounding. The implication is that these clasts have been abraded and sorted through the transport process. In nature there is a vast number of processes capable of transforming particle morphologies from angular to round, including the forces of ice, wind, and water. Beach environments contain rock fragments which typically show remarkable rounding produced by continuous wave action over the course of thousands of years (Figure 2-4). Due to complexities of natural surficial environments, it is rare that one process is solely responsible for the rounding of particles. Nevertheless, the ability to interpret morphologies and surface features out of geological context greatly enhances our ability to interpret paleoenvironments.

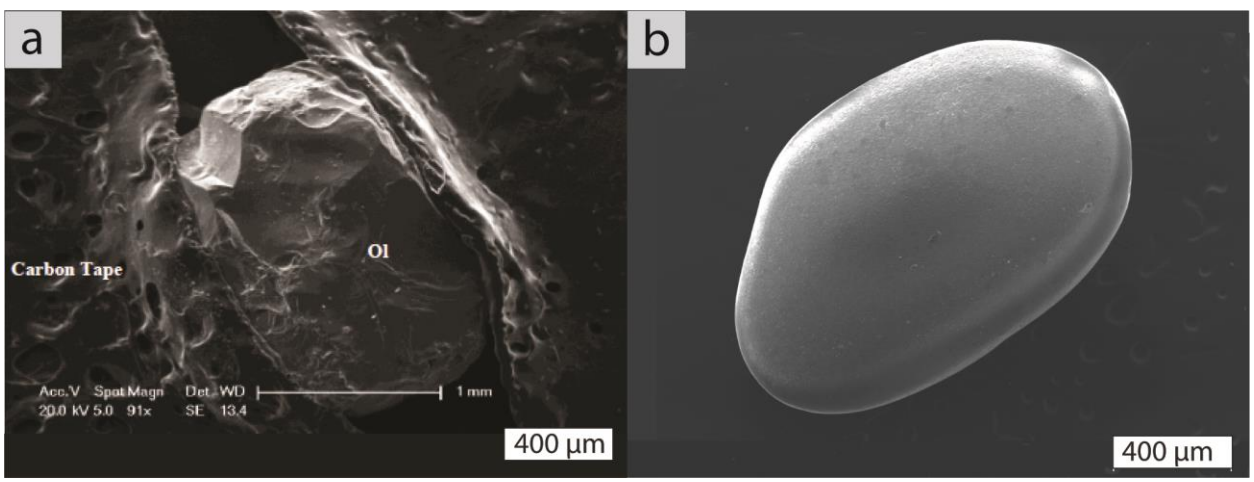

Figure 2-4. a) Angular olivine phenocryst imaged by Jones et al. (2014). b) Rounded and polished olivine sand grain from Punalu’u Black Sand Beach, Hawaii.

2.4 Applications in Volcanology

Volcanic environments are host to some of the most energetic processes on the planet, capable of moving large volumes of material at several meters per second for sustained periods of time. These turbulent, high energy, particle laden environments (Figure 2-5) provide ideal conditions for efficient particle-particle interactions (Cagnoli and Manga, 2003; Campbell et al., 2013; Dufek et al., 2012, 2009; Dufek and Manga, 2008; Jones et al., 2016; Jones and Russell, 2017; Kueppers et al., 2012; Mueller et al., 2015).

During a volcanic eruption, the rapid expansion of volatiles leads to magma fragmentation in which an initial size distribution of juvenile clasts is produced and released into the particle rich gas jet. Dufek et al. (2012) argue that the confined nature of the conduit in combination with high particle concentrations and velocities leads to a high probability of disruptive collisions (defined as losing >25% of the original clast volume). This causes modification of the original pumice size distribution produced at the fragmentation front. In their study, experiment data was used in conjunction with numerical simulations to illustrate that large particles are unlikely to exit the vent without undergoing a disruptive collision. Jones and Russell (2017) illustrated, using grain attrition experiments that fine ash production through attrition operates on short timescales (< 15 minutes) within conduits and plumes, rapidly increasing surface area generation. The authors used Entropy of Information as a metric to quantify the degree of attrition in natural and experimentally produced total grain size distributions (TGSDs). Specifically, a TGSD with a low EOI has likely undergone substantial milling and attrition whereas a low EOI would indicate a population yet to be attritted.

Within the conduit, wall rocks termed accidental lithics (Campbell et al., 2013; Wilson et al., 1980) are violently entrained into the stream of erupting material and subjected to ash

blasting (Campbell et al., 2013), a process whereby a rock is milled by a jet of hot ash. Campbell et al. (2013) produced the first detailed morphological data set of accessory lithics. It was suggested that the morphology of the accessory lithics is controlled by ash blasting, flaking of exterior surfaces (driven by rapid heating) and disruptive collisions. Deeper sourced (~2 km depth) monzogranite clasts were postulated to have rounded morphologies and smoother surfaces owing to longer residence times (up to ~1h) in the conduit. Shallow-seated dacite clasts, in stark contrast were found to have angular morphologies as a result of short (<2 min) milling durations.

As the eruption column becomes unstable, it can be subject to collapse, forming rapid pyroclastic flows and surges. Within these propagating granular mass movements, particles become fluidized (Sparks, 1976) undergoing energetic collisions (Kueppers et al., 2012; Manga et al., 2011). Using a tumbling mill, Kueppers et al. (2012) performed experiments at ambient (room temperature and pressure) conditions on volcanic samples from Unzen, Santorini and Bezymianni, recording the evolving grain size distributions over time. It was found that in all cases the production of fine ash was rapid at short durations (<30 min) and then decayed with increasing timescales. This finding is an agreement with the results of Manga et al. (2011) who performed experimental measurements to determine an empirical relationship between particle shape and mass loss through milling of pumice from four different localities. Using roundness as a shape metric it was found that a steady state roundness was achieved between 15-60% mass loss for milled samples. Jones et al. (2016) performed fragmentation experiments on pumice from Soufriere Hills Volcano through milling, decompression and impact experiments. Ash shape analysis revealed that the axial ratio increases during milling and particle convexity increases with repeated impacts. The authors also found that all three methods of fragmentation produced fractal breakage patterns where the fractal dimension increased from a minimum of

~2.1 through decompression (primary fragmentation) to a maximum of ~2.7 for repeated impacts (secondary fragmentation). A summary schematic of where and how attrition operates in volcanic systems is presented in Figure 2-5.

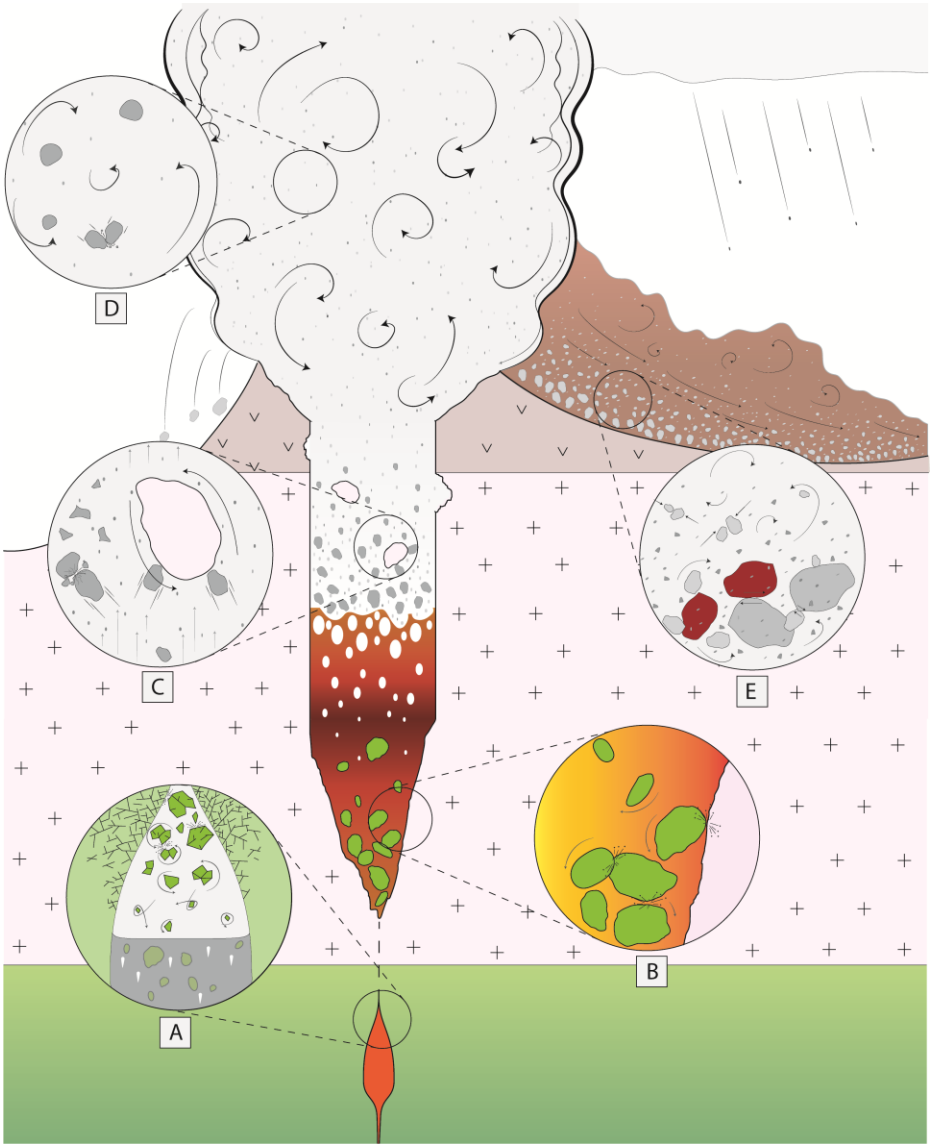

Figure 2-5. A) Attrition of mantle cargo after being picked up by the ascending dyke. B) Abrasion of xenoliths as they collide with themselves and dyke walls during settling. C) High energy disruptive collisions of juvenile volcanic clasts. Xenolith wall rocks are fluidized and milled in the particle rich gas jet. D) Lower energy collisions take place in the plume resulting in attrition primarily by abrasion and secondary ash production. E) Particles are fluidized in pyroclastic density currents where rounding takes place through abrasion.

2.5 Attrition in Kimberlites

Kimberlite magmas form at depth in excess of 150 km and transit the relatively cool cratonic mantle on a timescale of hours to days (Sparks, 2013; Sparks et al., 2006; Wilson and Head, 2007). Through the assimilation of orthopyroxene, the silica undersaturated magma exsolves CO_2 rich fluids and quickly adopts turbulent flow (Brett et al., 2015; Kamenetsky et al., 2008; Russell et al., 2012; Wilson and Head, 2007). The buoyant nature of the magma provides the foundation of the "kimberlite factory" model presented by Brett et al. (2015) whereby the driving pressure of the dyke causes fracturing of the overlying mantle and entrainment of xenoliths into the fluid rich bulbous head of the magma (Figure 2-6). This region was estimated to range in length from 4.5 km to 1.5 km depending on the density contrast relative to the lithospheric mantle (Brett et al., 2015). Importantly, this fluidized multiphase mixture encourages frequent particle-particle collisions resulting in rounding and surface modification of xenocrysts (Arndt et al., 2010; Brett et al., 2015; Jones et al., 2019, 2014; Jones and Russell, 2018). Jones et al. (2014) observed hemispherical features on the surfaces of xenocrystic olivine from Igwisi Hills which was attributed to impact during attrition. In the same study, textures derived from 'chemical' (i.e. crystallization and dissolution) processes were compared with that of 'mechanical' (i.e. attrition) processes. It was concluded that the textures observed on the surfaces of olivine xenocrysts were dominantly mechanical in nature. Jones et al. (2019) suggests that the early stages of kimberlite ascent are dominated by chemical dissolution as xenocrysts are out of equilibrium with the melt. The process of attrition first becomes relevant during the onset of turbulent ascent. As silica saturation is reached by the magma, the xenocrysts can develop phenocrystic rims (Arndt et al., 2010; Brett et al., 2015, 2009; Kamenetsky et al., 2008) during which chemical and physical

modification are in constant competition. This competition is alluded to in Arndt et al. (2010) who noted stripping of phenocrystic rims around xenocrysts and depressions on the rim exteriors.

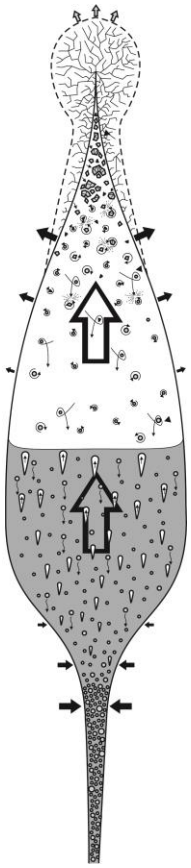

Figure 2-6. Stratified kimberlite dyke modified from Brett et al. (2015). Xenoliths are sampled by the crack tip into the fluid/gas rich head of the dyke where they are disaggregated and the liberated xenocrysts are milled. They then settle into the volatile-poor tail where they are preserved.

Analogue experiments studying attrition during kimberlite ascent were first performed by Jones and Russell (2018) who conducted fluidized experiments on olivine grains at various residence times. It was found that the attrition rate was high at low residence times and then plateaued at longer timescales after grains became rounded. This process was quantified by

assessing the ratio of daughter particles (produced by attrition) to the total initial particles (m_d / m_0) after Jones et al. (2017):

$$\frac{m_d}{m_0} = a(1 - e^{-bt}) \qquad [2.1]$$

Where a represents the infinite attrition limit (i.e. plateauing value) and b represents the rate at which the limit is reached. Jones et al. (2019) studied the influence of particle concentration and input energy on the attrition process by varying input mass and gas flux. It was concluded that the attrition limit (a) is dependent on the amount of energy that the suspended particles have, and the attrition rate (b) depends on both the probability for a collision to occur and that collisions are at or above the threshold for breakage. Importantly, olivine was efficiently reshaped at short timescales (< 5 h) relevant to kimberlite ascent. A comparison between the attrition experiment products and natural olivine xenocrysts from Diavik revealed a remarkable resemblance in both morphology and surface features. Specifically, both particles showed rounded morphologies and rough pitted surfaces.

In the final stages of ascent when kimberlite magmas reach within a few hundred meters of the surface, choked flow conditions can lead to explosive cratering initiating pipe formation (Sparks et al., 2006; Walters et al., 2006). This is followed by deep pipe excavation to form a diatreme as well as decreasing exit velocity. During the waning of gas flow, wall rocks and erupted mantle cargo (i.e. xenoliths and xenocrysts) are no longer elutriated from the pipe and are instead suspended in a turbulent gas-solid mixture (Gernon et al., 2009b, 2008; Sparks et al., 2006; Walters et al., 2006; Woolsey et al., 2019, 1975). This phenomenon takes place when the particle velocities fall between the minimum fluidization velocity (U_{mf}) and terminal velocity (U_t), causing particles to become fluidized (Figure 2-7).

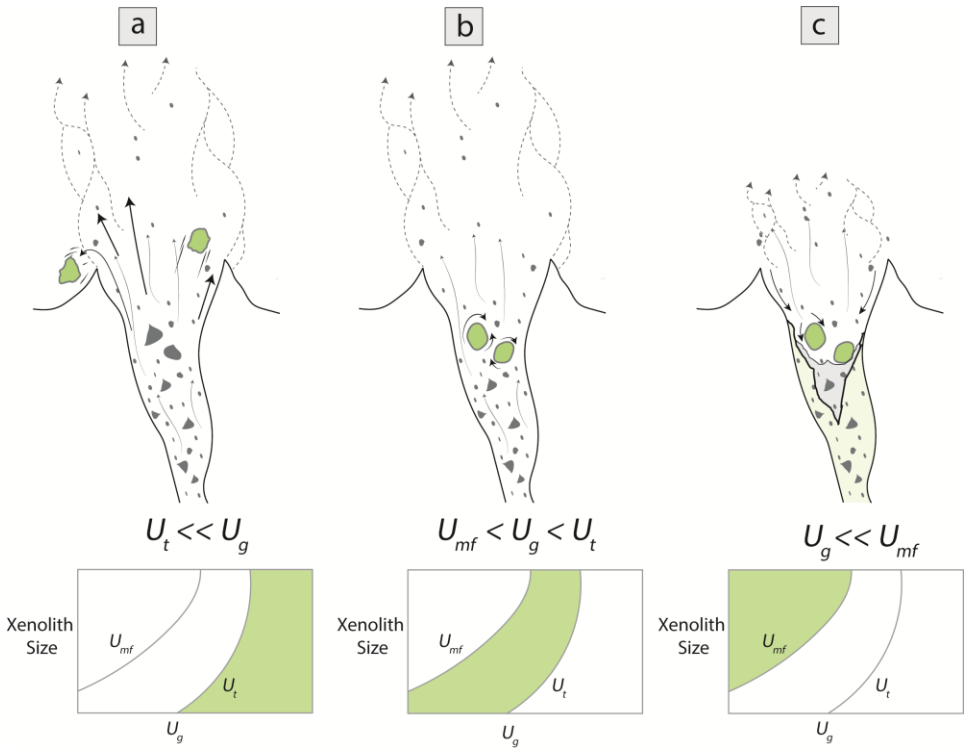

Figure 2-7. a) Gas velocity (U_g) is much greater than the terminal settling velocity (U_t); xenoliths are elutriated. b) Gas velocity falls between the minimum fluidization velocity (U_{mf}) and elutriation velocity; xenoliths are fluidized and milled in the gas jet. c) Gas velocity is much less than minimum fluidization velocity; xenoliths are unable to become fluidized.

During the process of fluidization within the diatreme, xenoliths are subject to vigorous blasting by ash and smaller particles as well as disruptive collisions with larger particles (Campbell et al., 2013; Dufek et al., 2012). Observations of rounded nodule-like xenoliths and wall rocks in kimberlites have been described by many authors (Arndt et al., 2006, 2010; Brown et al., 2007; Kurszlaukis and Barnett, 2003; Peltonen et al., 2002; Smith and Griffin, 2005). These observations and interpretations are summarized in Table 2-1. Importantly, milling within diatremes is a common interpretation for rounding and polished surfaces of clasts, however this process is not well understood due to a lack of literature exploring the timescales and energetics

required. A morphology dataset of eclogite and peridotite xenoliths from the University of Alberta Diavik collection is presented in Appendix D-1.

Source	Xenolith Type	Observation	Interpretation
Peltonen et al. (2002)	Eclogite	Eclogite xenoliths are rounded; surfaces reveal scratches and friction-crack-like markings. Garnet surfaces appear etched	Scratch marks and etch features are mechanically and chemically induced, respectively during magma ascent
Barton Jr and Gerya (2005)	Sheared garnet-harzburgite	sheared peridotites are smaller than non-sheared	Size reflects inferior resistance to abrasion within kimberlite magma
Smith and Griffin (2005)	Garnetite	xenoliths are nearly equant with smooth and polished surfaces	Abrasion and impact during emplacement of diatreme fill
Arndt et al. (2006, 2010)	Dunite	Monomineralic aggregates of olivine, termed 'nodules' are well rounded	Rounding is due to abrasion of nodule during kimberlite magma ascent
Brown et al. (2007)	Dolerite and Gneiss	Clasts are spheroidal, commonly featuring concentric layering	dominantly alteration processes. Abrasion and milling are also likely
Kurszlaukis and Barnett (2003)	Amphibolite Country Rock	Clasts show high degree of sphericity and chip marks	concave chips suggestive of vigorous clast-clast impacts

Table 2-1. Observations and interpretations of rounded xenoliths from kimberlite in the literature.

Kimberlitic eruptions are likely explosive in nature and postulated to feature particle laden, fast moving pyroclastic flows where attrition operates (Dufek et al., 2009; Freundt and Schmincke, 1992; Gernon et al., 2009a; Kueppers et al., 2012). However, due to erosion these deposits are rarely preserved and available for study.

After deposition of a kimberlite body, the pipe is subject to erosion and its contents are re-sedimented and dispersed through transport. The dispersed material forms an 'indicator train' whereby the mantle minerals known as kimberlite indicator minerals (KIMs) are used to trace the source kimberlite pipe (Ozyer and Hicock, 2011). Due to the varying physical properties of the indicator minerals (olivine, garnet, clinopyroxene, ilmenite etc.) they will undergo varying amounts abrasion which can be used as a proxy for distance from the pipe (Afanas'ev et al., 2008; Cummings et al., 2014, 2011; Pokhilenko et al., 2010). To understand physical modification of grains during dispersal, numerous studies have been aimed at determining the relative abrasive susceptibility of the indicator mineral suite. Afanas'ev et al. (2008) used an ultrasonic dispenser to induce abrasion in a mixture containing olivine, pyrope, picroilmenite, apatite, diamond and kimberlite fragments for a total duration of 635 min. The following sequence of mineral abrasive stability was established: pyrope, olivine, picroilmenite, apatite, kimberlite fragments. Diamond virtually underwent no change in the experiment. Cummings et al. (2014) performed comminution of indicator minerals in a tumbling mill using stainless steel shots as an abrasive agent up to 460 hours. Ilmenite was found to be the most stable, followed by chrome diopside and garnet. Garnet broke down in a two-stage process: firstly, by abrasive removal of a kelyphite rim, and then by rapid disintegration. Jones and Russell (2018) performed tumbling mill experiments on olivine up to a duration of 715 hours. Attrition rates were found to decrease substantially after ~5 days once grains had been reduced by ~2.5 wt%. The particle shape metric circularity also followed a trend of initial rapid rise followed by a plateau.

This thesis investigates the attrition of mantle minerals at conditions scaled to match that of ascending kimberlite magmas. The research aims to use the data to inform on ascent timescales and velocities rather than timescales and distances associate with surface re-sedimentation.

Chapter 3: Attrition Apparatus for Experiments

Experiments were performed in an experimental apparatus at standard laboratory conditions wherein minerals grains (i.e. particles) were suspended in an air-jet (Jones et al., 2019; Jones and Russell, 2018; Xiao et al., 2014, 2012). The apparatus (Figure 3-1; Appendix A.1) features a compressed air feed that passes through a calibrated FMA 5526 Omega gas flow meter (measuring gas flux), and into to the base of a 3.5 cm diameter, 120 cm long vertical attrition tube. The gas enters the base of the tube via a distributor plate which features 41 evenly spaced holes (Figure 3-1) to ensure an equally distributed gas flux to suspend the particles. As particle interactions occur within the attrition tube, fine particles are elutriated from the bed, passing up the attrition tube and into a 70 cm long, 20 cm diameter settling chamber which serves two primary purposes. Firstly, a lower gas flux in the settling chamber allows particles 23-135 μm to be recycled back into attrition tube which would otherwise leave the attrition process. Secondly, ultrafine particles (<23 μm) can be elutriated from the settling chamber, passing through an elbow joint, down a tube and finally into a fines collection nylon filter bag with 1 μm openings to ensure minimum loss from the system.

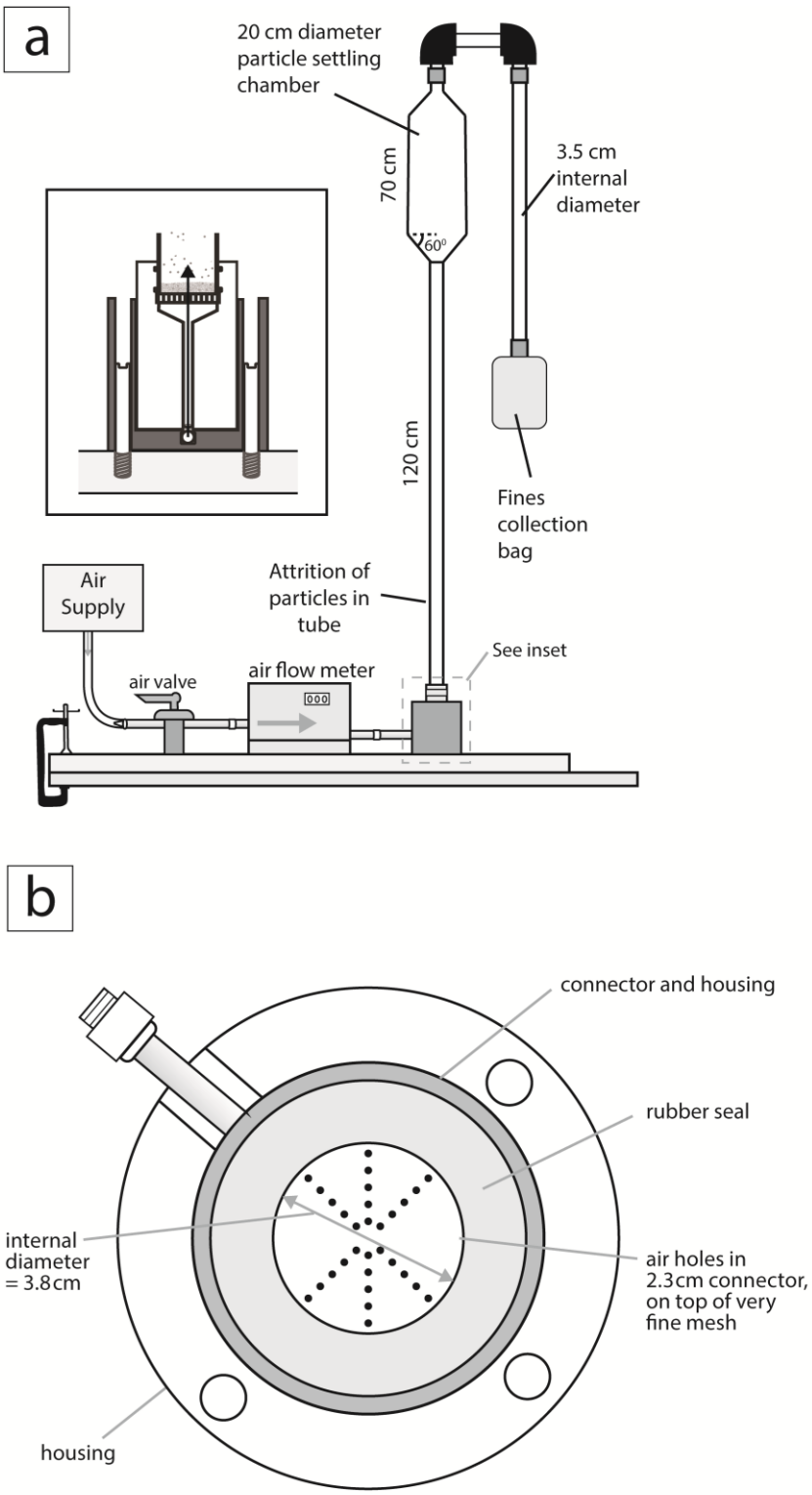

Figure 3-1. a) Schematic diagram of the attrition apparatus used in this study. Inset shows sample resting on the distributer plate and fluidized by the gas jet (solid arrow). b) Distributor plate components.

3.1 Modifications to the Attrition Apparatus

The apparatus of Jones and Russell (2018) and Jones et al. (2019) which was adapted from the ASTM D5757-00 standard experimental apparatus has been improved by modifications. The original device used in Jones and Russell (2018) and Jones et al. (2019), did not include a settling chamber and the gas carrying fine particles exited into a 500 mL water reservoir. The main problem with the water reservoir is that if the tube is too far submersed in water the gas is unable to exit the system and significant overpressure results which supresses the particle bed height. Additionally, fracturing of the acrylic tubes and the distributor plate are more likely with overpressure. Another problem arises after long experimental durations wherein the water level of the reservoir decreases due to continuous mixing of the water and the turbulent gas flow. To resolve these issues, I replaced the previous water collection method with a fines collection filter bag instead.

A settling chamber was also added to the apparatus used in this study. This also allowed experiments to be performed at slightly higher gas fluxes than previous experimental campaigns. Secondly it serves to prevent significantly large daughter fragments from exiting the attrition process early in the experiments. With a large diameter settling chamber, only fine particles can leave the attrition process and larger particles fall down the steep angled flanks at the base of chamber and return to the attrition tube.

My modifications to the apparatus are beneficial since the apparatus is more suited to the experimental campaign designed for this study and more closely resembles the updated standard ASTM D575-11 apparatus used for determining attrition of catalysts by air jets (ASTM, 2017).

The vertical attrition tube and the exit tube connected to the fines collection bag are both made of acrylic. The alternatives considered in the updated design were AISI 316 stainless steel

and polycarbonate. Polycarbonate is very similar to acrylic with the main differences being that polycarbonate has a higher impact strength, scratches easier and is less transparent. Since a high impact strength is not necessary and high-speed filming is utilized in this study, the superior scratch resistance and transparency make acrylic favorable to polycarbonate. AISI 316 stainless steel has a low thermal conductivity and melting point of 16.3 W/mK and 1370 ^{0}C respectively, which was considered for future work studying the effects of temperature on the attrition rates. However, temperature effects were not investigated in this work and a stainless-steel pipe would not allow for filming of the experiments.

3.2 Experimental Conditions

In order to understand how the particles would interact with the gas flux, the basic principles of fluidization were applied. As gas flux increases, there will be a point at which the particle bed no longer acts as a coherent mass, instead adopting a fluid-like appearance, and is said to become fluidized. The velocity of the gas at which this phenomenon takes place is known as the minimum fluidization velocity, U_{mf}. A general solution to predict U_{mf} is presented by Kunii & Levenspiel (1969), known as the Ergun Equation:

$$\frac{1.75}{\varepsilon\phi}\left(\frac{d_p U_{mf}\mathrm{g}}{\mu}\right)^2 + \frac{150(1-\varepsilon)}{\varepsilon^3\phi^2} \times \frac{d_p U_{mf}\mathrm{g}}{\mu} = \frac{{d_p}^3\rho_\mathrm{g}(\rho_\mathrm{p}-\rho_\mathrm{g})\mathrm{g}}{\mu^2} \qquad [3.1]$$

Where μ is the fluid viscosity, d_p is the particle diameter, ρ_g is the fluid density, ρ_p is the particle density, ε is the void space of the bed, ϕ is the particle sphericity, and g is the acceleration due to gravity.

If the gas flux is further increased, the terminal settling velocity U_t of the particles is overcome and particles will be elutriated and carried out of the fluidized bed. The terminal fall

velocity changes depending on the Reynolds Number (Re) of system (Kunii & Levenspiel., 1969):

$$U_t = \frac{g(\rho_p - \rho_g){d_p}^2}{18\mu} \qquad (\mathrm{Re} < 0.4) \qquad [3.2]$$

$$U_t = \left(\frac{4(\rho_p - \rho_g)^2 g^2}{225\rho_g\mu}\right)^{\frac{1}{3}} \times d_p \qquad (0.4 < \mathrm{Re} < 500) \qquad [3.3]$$

$$U_t = \left(3.1g\,\frac{(\rho_p - \rho_g)}{\rho_g}d_p\right)^{\frac{1}{2}} \qquad (500 < \mathrm{Re} < 200{,}000) \qquad [3.4]$$

where Re < 0.4 is considered laminar, 0.4 < Re < 500 is transitional and 500 < Re < 200,000 is turbulent flow in a fluidized bed (Kunii et al., 1969). Particle attrition requires superficial fluid velocities between minimum fluidization and terminal settling velocity such that particles are sufficiently fluidized and can interact without being elutriated (Figure 3-2).

In the attrition apparatus there are three regions of interest in which gas velocities differ due to the varying diameter of the pipe the gas flows through. Firstly, the distributor plate (jet velocity) which has 41 holes each 0.795 mm in diameter, secondly the attrition tube (bed velocity) which has a diameter of 3.5 cm, and lastly the settling chamber (chamber velocity) which has a 20 cm maximum diameter. Superficial gas velocities at varying gas fluxes present in these regions of the apparatus are summarized in Table 3-1.

Gas Flux (L min^{-1})	**Jet Velocity (m s^{-1})**	**Bed Velocity (m s^{-1})**	**Settling Chamber Velocity (m s^{-1})**
105	**21**	**1.8**	**0.054**

150	32	2.7	0.081
200	43	3.5	0.11
250	54	4.4	0.14

Table 3-1. The calculated superficial velocity present within different areas of the attrition apparatus at different gas fluxes. Highlighted conditions are those used in this study.

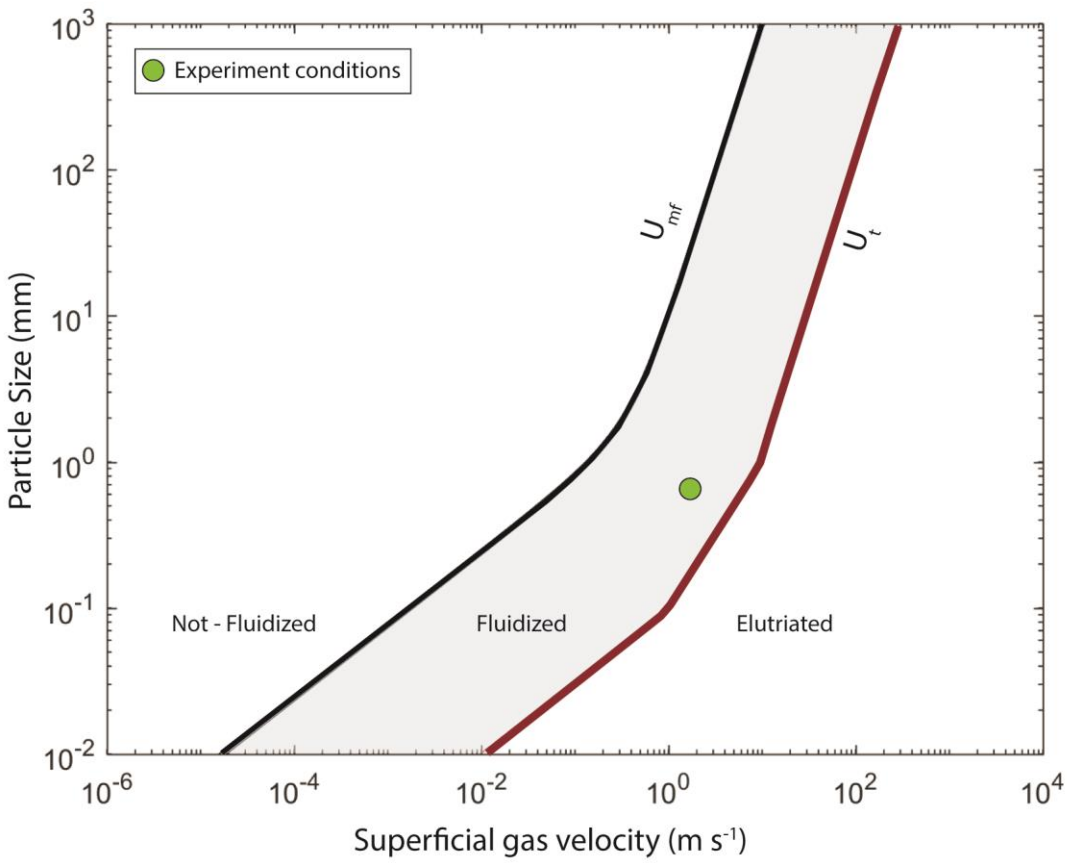

Figure 3-2. Minimum fluidization and elutriation velocities of olivine. Green marker represents the starting conditions of 105 L min^{-1} gas flux (1.8 m s^{-1} in the attrition tube) and 610-710 µm (655 µm mean) used for all experiments. Shaded region represents region of fluidization possible for attrition experiments on olivine. Parameters used: ρ_g = 1.225 kg m^{-3}, ρ_p = 3246 kg m^{-3}, µ = 1.82 × 10^{-5}, ε = 0.58, ϕ = 1.

Particle interactions (i.e. collisions) take place primarily in the attrition tube, therefore gas velocity here is of most importance when choosing the appropriate gas flux. The minimum fluidization velocity and terminal settling velocity of olivine used in this study are graphically shown in Figure 3-2 at the 105 L min^{-1} gas flux (1.8 m s^{-1} in the attrition tube) and 610-710 µm (655µm mean) starting condition. The figure shows that the starting conditions chosen for this study were sufficient to fluidize all mineral suites in the attrition tube. After performing these initial calculations, the conditions were empirically (i.e. through observation) tested using a gas flux of 105 L min^{-1}, a particle mass of 15 g and a size of 600-710 µm to ensure that the nature of fluidization was constant for all mineral types.

3.3 Scaling the Experiments to the Natural System

The conditions (gas flux and host fluid) at which the experiments were performed were carefully chosen such that the flow regime falls in the same regime (i.e. laminar or turbulent) as that expected during the ascent of kimberlite magma. Here I use a range of inputs from the literature to constrain the Reynolds number, Re of kimberlite dykes during ascent. Specifically, a dyke width (D) of 0.1 – 10 m (Jankovics et al., 2013; Jones et al., 2019; Kavanagh and Sparks, 2011; Petcovic and Dufek, 2005; Sparks et al., 2006; Wilson and Head, 2007), a dyke ascent velocity (v) of 1 – 20 m s^{-1} (Brett et al., 2015; Jones et al., 2019; Kavanagh and Sparks, 2009; Russell et al., 2012; Sparks, 2013; Sparks et al., 2006; Wilson and Head, 2007), a magma viscosity (µ) of 0.01 – 50 Pa s (Brett et al., 2015; Chepurov et al., 2018; Moss and Russell, 2011; Persikov et al., 2015; Sparks et al., 2006), a magma density (for a range of exsolved fluid proportions) (ρ) of 2000 – 3000 kg m^{-3} (Brett et al., 2015; Jones et al., 2019; Kavanagh and

Sparks, 2009; Moss and Russell, 2011; Russell et al., 2012; Sparks, 2013; Sparks et al., 2006; Wilson and Head, 2007) to arrive at $Re_k \sim 1 \times 10^2 - 1 \times 10^6$ using:

$$\mathrm{Re_k} = \frac{\mathrm{D}v\rho}{\mu} \qquad [3.5]$$

Then, using a gas flux of 105 L min^{-1}, a pipe diameter of 0.035 m and the viscosity of air, 1.82 x 10^{-5} Pa s, the Reynolds number calculated for flow within the attrition apparatus is 4.28 x 10^3. Therefore, the gas flux (105 L min^{-1}) and fluid (air) chosen for this experimental campaign produces a Reynolds number which falls within the range of conditions attending to kimberlite transport, and the results quantified in this study can be compared to the natural system. It should be noted however that the Reynolds numbers calculated for the natural system represent a conservative lower estimate. At shallower depths, CO_2 is liberated as a supercritical fluid (and later a gaseous phase), decreasing the density of the kimberlite and increasing the ascent velocity (Russell et al., 2012; Wilson and Head, 2007), further supporting attrition. The process and its implications are further discussed in more detail in the discussion chapter of this thesis. Furthermore, a more detailed scaling analysis is also performed in the discussion chapter.

3.4 Data Collection During and After Experiments

Before each experiment, air was passed through the apparatus to check for potential leaks. After no leaks were detected, particles were loaded onto the distributor plate and a stream of compressed gas was fed into the vertical attrition tube (Figure 3-1), fluidizing the particle bed of height h_0 to h_p (Figure 3-3). The h_p measurement was taken two minutes after the gas flux was initiated for each experiment.

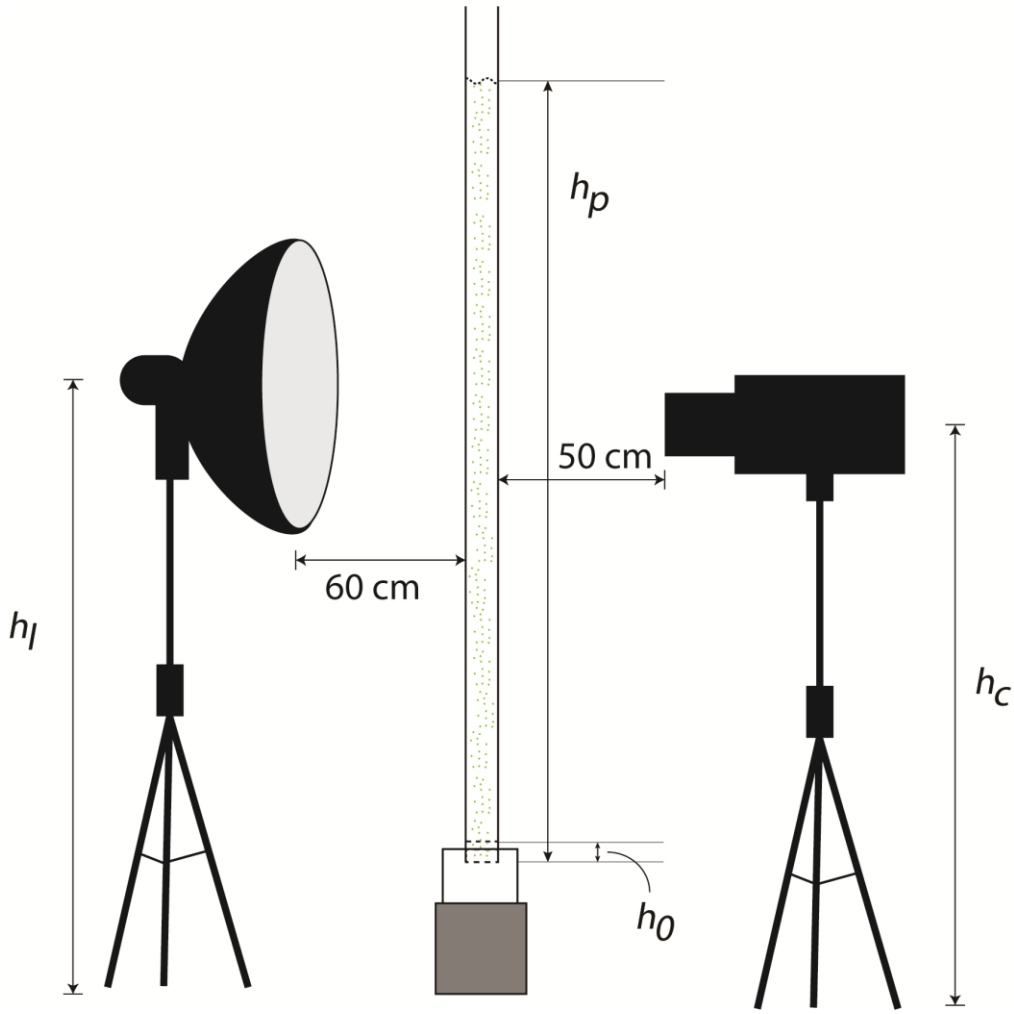

Figure 3-3. Cartoon illustration of data collected during an experiment. h_0 is the initial bed height, h_p is the height of the fluidized column. Select experiments of each mineral were filmed using a high-speed camera and a strobe light. The height of the strobe light (h_l) and the height of the camera (h_c) changed for each mineral.

As particle beds become fluidized, the nature and extent of fluidization varies as a function of experimental conditions. From the engineering sciences these factors include the particle properties (density, size), gas composition and the flow velocity (Grace, 1986). To document the nature of fluidization and particle interactions, a Chronos 1.4 high-speed camera recorded 20 seconds of select experiments at 1,050 frames per second during the beginning stages of an

experiment (two minutes after the gas flux was initiated). To ensure that individual particles could be tracked with accuracy, a Godox QT600II high speed flash strobe light was used to visually brighten and enhance the footage captured. Although the absolute heights of the strobe light and camera (h_l and h_c respectively) were scaled and changed for each mineral, the distance from the attrition tube was consistent at 60 cm for the strobe light and 50 cm for the high-speed camera (Figure 3-3).

Here I adopt the same, simplified classification scheme of flow regimes documented within the attrition apparatus used by Jones et al. (2019). These regimes are found to vary mainly as a function of particle concentration and gas flux and include fountaining, transitional and pneumatic (Figure 3-4). Fountaining behavior is generally observed if particle concentrations are high. In this regime, particles move as a coherent mass and the bed height (h_f) pulsates with time. The other end member regime is pneumatic wherein particle concentrations are low. Here particles are homogeneously distributed throughout the fluidized column, moving independently of each other and enclosed by a stable column height, h_p. A transitional regime was found to exist between the two members where a stable column of particles is seen above a fountaining particle bed.

Since the fluidization regime influences particle collision efficiency, it was important to make sure this was kept constant for each mineral. Before starting the experimental campaign, the proposed starting mass (15 g) and gas flux (105 L min^{-1}) was tested for each mineral and the fluidization was subsequently documented. To make sure that the conditions weren't directly bordering another flow regime, the gas flux was also tested at +/- 10 L min^{-1}. Using these preliminary observations, it was found that all minerals at the chosen conditions were fluidized in a pneumatic style.

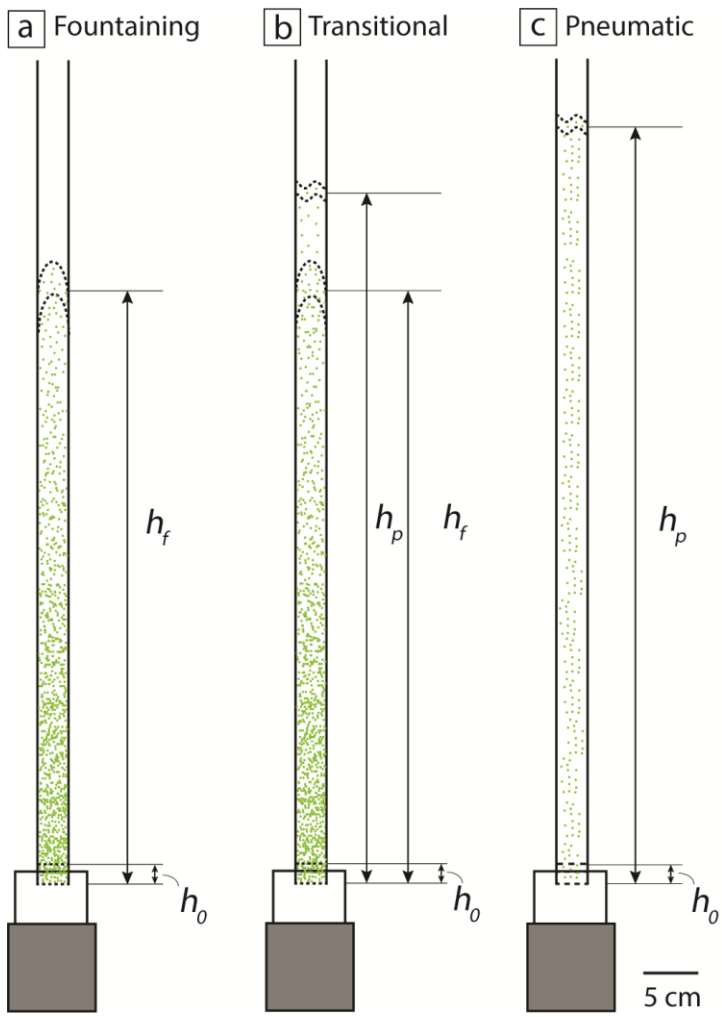

Figure 3-4. Experimental flow regimes in the attrition apparatus taken from Jones et al. (2019).

After ending an experiment (i.e. switching off the gas flow) the apparatus was left for at least 1 hour to ensure fine particles could settle. Then, the attrition apparatus was carefully disassembled and washed with deionized water over a standard stack of ASTM E11 mechanical sieves with a mesh size range of 125 µm to 600 µm and a collection pan below the 125 µm sieve. The sieves were then left to dry in a 70°C slow drying oven overnight. The following day the material was dry sieved for ~ 1 minute and the contents of each sieve were weighed using an analytical balance correct to four decimal places. Due to problems with sieving fine particles

such as agglomeration and lofting, material caught in the pan (i.e. <125 µm) had a grain size distribution measured using Laser Particle Size Analysis (LPSA). This technique has become standard in measuring the size distribution of powders (Jones et al., 2019, 2017; Jones and Russell, 2018, 2017; Kang et al., 2017; Kim et al., 2019; Xiao et al., 2014, 2011). A Malvern Mastersizer 2000 laser diffraction device with a hydro 2000 Mu water dispersion module attached was used for LPSA in this study. The pump speed, absorption coefficient and refractive index was varied for each mineral and can be found in Table 3-2 below. For each sample, an aliquot was added to the dispersion module and measured three times. To prevent particle aggregation, an ultrasonic pulse was applied immediately before measurement for 2 seconds. This process was repeated three times for a total of nine measurements. To obtain the final particle size distribution of the powder, the nine measurements were averaged for a mean grain size distribution.

Mineral	Pump Speed (rpm)	Absorption Coefficient	Refractive Index
Olivine	2600	0.1	1.70
Orthopyroxene	2600	0.1	1.59
Clinopyroxene	2600	0.1	1.70
Garnet	2900	0.1	1.74
Diamond	2800	0.1	2.42

Table 3-2. Mastersizer settings used for each mineral.

3.5 Experimental Grid

A total of 45 experiments (Table 3-3) were performed in which mineral type and experiment duration were varied. Five minerals including olivine (Ol), orthopyroxene (Opx), clinopyroxene (Cpx), garnet (Grt) and diamond (Dia) were all independently studied through 5 sets of single

mineral experiments. The effects of binary mineral mixtures were studied using a combination of olivine + garnet (Ol + Grt) and olivine + clinopyroxene (Ol + Cpx). The experimental duration varied from 0.5 h to 48 h. Gas flux, *Q* input mass, *m* and input mineral size, *d* were kept consistent across all experiments. Specifically, I used a gas flux of 105 L min^{-1}, an input mass of 15 g and an input size of 600-710 µm. For the binary mixture experiments, 7.5 g of each mineral was used for a total of 15 g. The experiments performed are summarized below in Table 3-3.

	time (h)										
Experiment No.	0.5	1	2	4	6	8	12	16	24	36	48
1:A-K	x	x	x	x	x	x	x	x	x	x	
2:A-F			x		x		x		x		x
3:A-L	x	x	x	x	x	x	x	x	x	x	x
4:A-K	x	x	x	x	x	x	x	x	x	x	
5:A-H	x	x	x		x		x		x		x
	time (h)										
Experiment No.	0.5	1	2	4	6	8	12	16	24	36	48
6:A-C		x			x				x		
7:A-C		x			x				x		

* All experiments performed at a gas flux of 105 L min-1, a grain size of 600 - 710 µm and a mass of 15 g

Table 3-3. Experimental grid showing the 49 experiments performed in this study. X denotes that an experiment was performed at the noted time. Series 1, 2, 3, 4, 5 are single mineral experiments on the minerals: olivine, orthopyroxene, clinopyroxene, garnet and diamond respectively. Series 6 and 7 are mineral mixture experiments with series 6 representing an olivine-garnet mixture and series 7 representing an olivine-clinopyroxene mixture.

Chapter 4: Sample Characterization

4.1 Sample Characterization

Fresh (i.e. unaltered) minerals for this project were sourced from a variety of companies mostly specializing in abrasives or gemstone sales (photographs of minerals in Appendix B.1). Forsterite (olivine) sand derived from crushed dunite was obtained from Ashwani Industrial Minerals Corp.; pyrope (garnet) sand from Zhangjiakou Xuanhua Ju Hong Abrasion Resistant Material Distribution Co., Ltd.; chrome diopside (clinopyroxene) from Sovtube, an unaffiliated seller; and natural rough diamond sand from CDL FINESHINE. The clinopyroxene and orthopyroxene could only be obtained as large (i.e. >5 mm) crystals and were manually crushed using a corundum mortar and pestle. Before using the minerals for experiments for experimental purposes, all mineral sands were sieved to the desired, restricted grain size of 600-710 µm and washed using deionized water to remove any adhering fine particles.

4.1.1 Density Measurements

Densities of each mineral (reported in Table 4-1) were calculated using an analytical balance to measure mass and a Micrometrics Accuppyc II 1340 Helium pycnometer to measure volume. Three aliquots of the sample were measured for mass and volume, then plotted as mass [g] against volume [cm^3]. A linear regression was fitted through the three data points and the origin, with the slope being the density [g cm^{-3}] of the mineral (Figure 4-1).

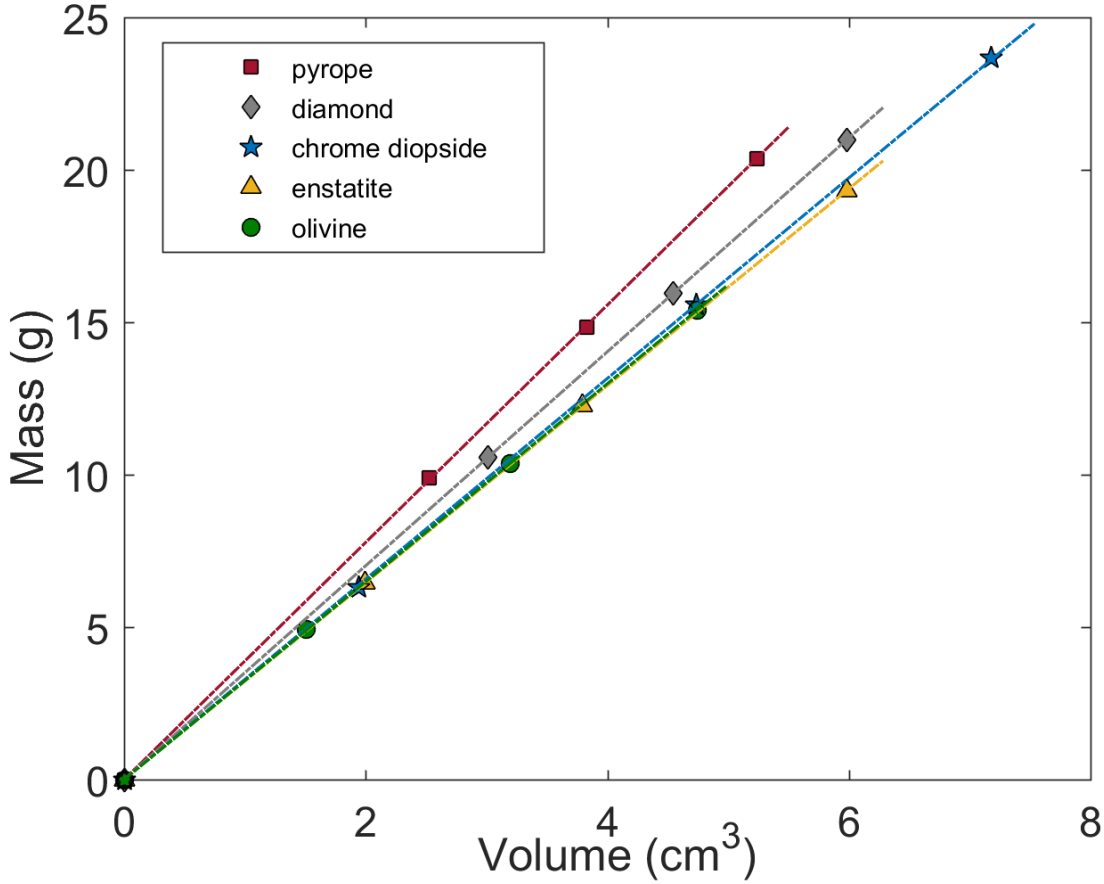

Figure 4-1. Mass plotted against volume for three aliquots measured of each mineral. A linear curve is fitted through the data points and the origin to obtain the best approximation of density.

	Forsterite	Enstatite	Chrome Diopside	Pyrope	Diamond
Density (g cm^{-3})	3.246	3.230	3.290	3.891	3.508

Table 4-1. Reported densities obtained for each mineral.

4.1.2 2D Shape Characterization

From the starting products and select experiments (Table 4-2), 100-110 grains from the parent grain size fraction (600-710 µm) were randomly selected and individually photographed under a binocular microscope with an intense backlight. For orthopyroxene, grains were often too translucent for outlines to be seen clearly. On that basis, the grains were imaged on a flatbed scanner using 1200 dpi resolution. Adopting similar methodology outlined in Jones and Russell (2018), the images were imported into the software, ImageJ (https://imagej.nih.gov/ij/) and a threshold was applied to the images to convert to a binary image. Since the minerals inherently have different colours, the threshold value applied to the images varied for each mineral. Specifically, the threshold values for olivine, orthopyroxene, clinopyroxene, garnet and diamond were 140,125,170,140 and 180 respectively. After the threshold was applied, each image was checked, and if the automated thresholded image did not match the outline of the grain seen in the original image, the threshold was manually adjusted by +/- 10. This process is summarized visually below in Figure 4-2.

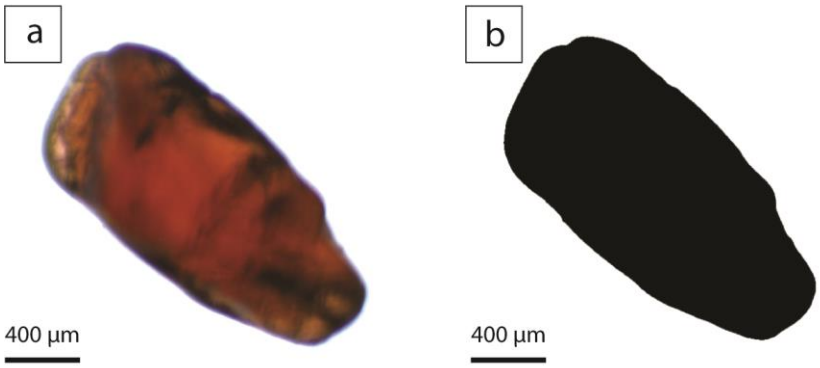

Figure 4-2. a) An image of a garnet grain taken with the binocular microscope. b) The grain thresholded and converted to binary.

In order to quantify the shape evolutions of the 2D binary mineral projections through time, the images were imported into Matlab and analyzed using a shape analysis script (Appendix E) that I modified from Campbell et al. (2013). The Matlab script detects all black areas larger than a specified pixel area of 2000 (to avoid capturing random particles) and computes the projected area, perimeter, major axis, minor axis, convex hull area and convex hull perimeter. One feature of the script is that the perimeter is constructed by connecting every fourth pixel that lies along the outline of the mineral. This was found to produce the most accurate approximate when applying the script to shapes with known perimeters (squares, circles, triangles, etc.). These shape parameters area visualized in Figure 4-3.

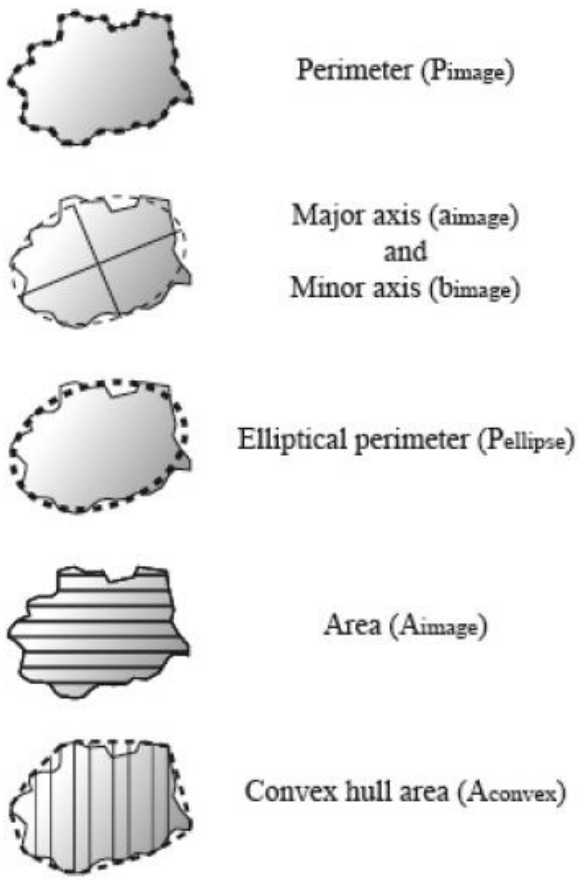

Figure 4-3. Visualization of parameters used to quantify shape metrics from Campbell (2012).

The major and minor axes are scalars that correspond to the length of the major and minor axes of the best-fit ellipse to the mineral's outline. The convex hull refers to the smallest convex polygon that can enclose the outline of the mineral grain. The computed parameters are in units of pixels but may be converted into absolute values if the conversion factor is known (i.e. a photo of a scale bar taken under the same conditions). In this study photos were taken at a consistent scale and dimensionless metrics were chosen thereby avoiding the need to convert between pixels and absolute units.

4.1.3 Scanning Electron Microscopy

To ensure that no fragments or fine particles were adhering to the surfaces, the experiment products were washed with deionized water and dried before analysis of grain features. Images of the overall morphology and the surfaces of representative grains were assessed at various magnifications using a Philips XL30 scanning electron microscope (SEM) in scanning electron mode with a 15-kV accelerating voltage and a 35 µA beam current.

4.1.4 Summary of Experiments Chosen for Analysis

Experiment No.	Mineral	Time (h)	Sieve down to 125 µm	LPSA on <125 µm	Bincocular image of parent grains	SEM images of products
1-A	Ol	0			x	x
1-B	Ol	0.5	x	x	x	x
1-C	Ol	1	x	x		
1-D	Ol	2	x	x	x	
1-E	Ol	4	x	x		
1-F	Ol	6	x	x	x	x
1-G	Ol	8	x	x		
1-H	Ol	12	x	x	x	x

1-I	Ol	16	x	x		
1-J	Ol	24	x	x	x	
1-K	Ol	36	x	x		x
2-A	Opx	0			x	x
2-B	Opx	2	x	x	x	x
2-C	Opx	6	x	x	x	x
2-D	Opx	12	x	x	x	x
2-E	Opx	24	x	x	x	
2-F	Opx	48	x	x		x
3-A	Cpx	0			x	x
3-B	Cpx	0.5	x	x		x
3-C	Cpx	1	x	x		
3-D	Cpx	2	x	x	x	
3-E	Cpx	4	x	x		
3-F	Cpx	6	x	x	x	x
3-G	Cpx	8	x	x		
3-H	Cpx	12	x	x	x	x
3-I	Cpx	16	x	x		
3-J	Cpx	24	x	x	x	
3-K	Cpx	36	x	x		x
3-L	Cpx	48	x	x		
4-A	Grt	0			x	x
4-B	Grt	0.5	x	x		x
4-C	Grt	1	x	x		
4-D	Grt	2	x	x	x	
4-E	Grt	4	x	x		
4-F	Grt	6	x	x	x	x
4-G	Grt	8	x	x		
4-H	Grt	12	x	x	x	x
4-I	Grt	16	x	x		
4-J	Grt	24	x	x	x	
4-K	Grt	36	x	x		x
5-A	Dia	0			x	x
5-B	Dia	0.5	x	x		x
5-C	Dia	1	x	x		
5-D	Dia	2	x	x	x	
5-E	Dia	6	x	x	x	x
5-F	Dia	12	x	x	x	x
5-G	Dia	24	x	x	x	
5-H	Dia	48	x	x		x

6-A	Ol + Grt	1	x	x
6-B	Ol + Grt	6	x	x
6-C	Ol + Grt	24	x	x
7-A	Ol + Cpx	1	x	x
7-B	Ol + Cpx	6	x	x
7-C	Ol + Cpx	24	x	x

Table 4-2. Post-experiment measurements of run products for each experiment. X represents measurements which were completed for each experiment series.

4.1.5 Mineral Properties Summary

Mineral Property	Forsterite	Enstatite	Chrome Diopside	Pyrope	Diamond
Density (g cm^{-3})	3.246	3.230	3.290	3.891	3.508
Hardness	5.0-6.0	5.0-6.0	5.5-6.5	7.0-7.5	10
Chemical Formula	$MgSiO_4$	$Mg_2Si_2O_6$	$Ca(Mg,Cr)Si_2O_6$	$Mg_3Al_2(SiO_4)_3$	C
Crystal System	Orthorhombic	Orthorhombic	Monoclinic	Cubic	Cubic
Cleavage	Poor	Well Developed	Well Developed	Absent	Perfect
Fracture	Conchoidal	Uneven	Uneven	Absent	Conchoidal
Hardness (GPa)	7.1	9	7.7	15	105
Tensile Strength (Mpa)	500	-	23	-	3750
Bulk Modulus (GPa)	-	105	114	172.4	442
Young's Modulus (GPa)	195	232	160.5	590	1050
Fracture toughness (MPa $m^{1/2}$)	1.1	-	3.5	1.4	3.4-4.8
Fracture Surface Energy (J m^{-2})	0.98	-	-	3.674	5.5

Table 4-3. Summary of physical properties of all minerals analyzed in this study. References can be found in Appendix F.

Chapter 5: Results and Analysis

5.1 Attrition of Individual Minerals

5.1.1 Fines Production Datasets

The products of each experiment were sieved and masses in each grain size interval were weighed. The smallest size fraction (<125 µm) was measured with a laser particle size analyzer as outlined in Section 3.4. Results are summarized in Table 5-1 as the initial mass (m_0), the total mass collected (m_r), the mass of daughter products (m_d i.e. mass below the 600-710 µm sieve) and the mass loss (m_l) defined as $m_l = m_0 - m_r$.

Mineral Series	Mineral	Time (h)	m_0 (g)	m_r (g)	m_d (g)	m_l (g)
1-A	Ol	0	15.0000	15.0000	0.0000	0.0000
1-B	Ol	0.5	15.0002	14.7730	3.2971	0.2272
1-C	Ol	1	15.0003	14.7514	5.1949	0.2489
1-D	Ol	2	15.0004	14.6861	6.4649	0.3143
1-E	Ol	4	15.0000	14.6203	8.4198	0.3797
1-F1	Ol	6	15.0004	14.6233	9.8665	0.3771
1-F2	Ol	6	15.0007	14.6468	8.6357	0.3539
1-F3	Ol	6	15.0008	14.5582	9.5495	0.4426
1-G	Ol	8	15.0011	14.5016	11.4637	0.4995
1-H	Ol	12	15.0003	14.4200	12.2867	0.5803
1-I	Ol	16	15.0003	14.6044	13.0698	0.3959
1-J	Ol	24	15.0000	14.1312	13.4116	0.8688
1-K	Ol	36	15.0000	14.3159	14.2273	0.6841
2-A	Opx	0	15.0000	15.0000	0.0000	0.0000
2-B	Opx	2	15.0009	14.5199	5.0700	0.4810
2-C	Opx	6	15.0009	14.4197	7.4700	0.5812
2-D	Opx	12	15.0008	13.9648	9.3359	1.0360

2-E	Opx	24	15.0008	13.8712	13.1100	1.1296
2-F	Opx	48	15.0000	13.8923	13.1900	1.1077
3-A	Cpx	0	15.0000	15.0000	0.0000	0.0000
3-B	Cpx	0.5	15.0006	14.8986	1.2183	0.1020
3-C	Cpx	1	15.0000	14.8501	1.4914	0.1499
3-D	Cpx	2	15.0007	14.7975	2.7769	0.2032
3-E	Cpx	4	15.0003	14.7557	3.6162	0.2446
3-F	Cpx	6	15.0000	14.7112	5.4378	0.2888
3-G	Cpx	8	15.0005	14.5912	8.0012	0.4093
3-H	Cpx	12	15.0000	14.5162	9.6691	0.4838
3-I	Cpx	16	15.0005	14.4372	10.8935	0.5633
3-J	Cpx	24	15.0000	14.4295	12.1299	0.5705
3-K	Cpx	36	15.0003	14.4623	13.4087	0.5380
3-L	Cpx	48	15.0005	13.9942	13.0112	1.0063
4-A	Grt	0	15.0000	15.0000	0.0000	0.0000
4-B	Grt	0.5	15.0010	14.8704	1.3331	0.1306
4-C	Grt	1	15.0001	14.8733	2.4727	0.1268
4-D	Grt	2	15.0011	14.7822	3.3694	0.2189
4-E	Grt	4	15.0005	14.5115	4.1867	0.4890
4-F	Grt	6	15.0005	14.5139	5.0056	0.4866
4-G	Grt	8	15.0008	14.6539	6.2334	0.3469
4-H	Grt	12	15.0004	14.5964	7.5080	0.4040
4-I	Grt	16	15.0013	13.8182	7.1561	1.1831
4-J	Grt	24	15.0011	14.3412	7.9238	0.6599
4-K	Grt	36	15.0008	14.4833	8.8299	0.5175
5-A	Dia	0	15.0000	15.0000	0.0000	0.0000
5-B	Dia	0.5	15.0003	14.8747	1.9859	0.1256
5-C	Dia	1	15.0000	14.805	2.8511	0.1950
5-D	Dia	2	15.0004	14.8199	3.1298	0.1805
5-E	Dia	6	15.0004	14.8272	3.9542	0.1732
5-F	Dia	12	15.0000	14.7642	4.0111	0.2358
5-G	Dia	24	15.0004	14.9255	4.1216	0.0749
5-H	Dia	48	15.0001	14.799	4.6798	0.2011

Table 5-1. Table of masses (g) recorded for each experiment: m_0 is the initial mass, m_r is the total mass recovered after the experiment, m_d is the mass of daughter products and m_l is the difference between the starting and the recovered mass.

The mass loss for each experiment is plotted against time in Figure 5-1. Uncertainty is represented as one relative standard deviation obtained from repeating experiment 1-F three times with a relative standard deviation of 6.8%. For all mineral series, m_l increases initially and then plateaus at longer durations. As noted in previous attrition studies, the loss of particles is inevitable and is a function of the experimental apparatus, attrition rate, particle size, particle material and the post-experiment collection method (Chen et al., 2007; Kang et al., 2017; Kim et al., 2019).

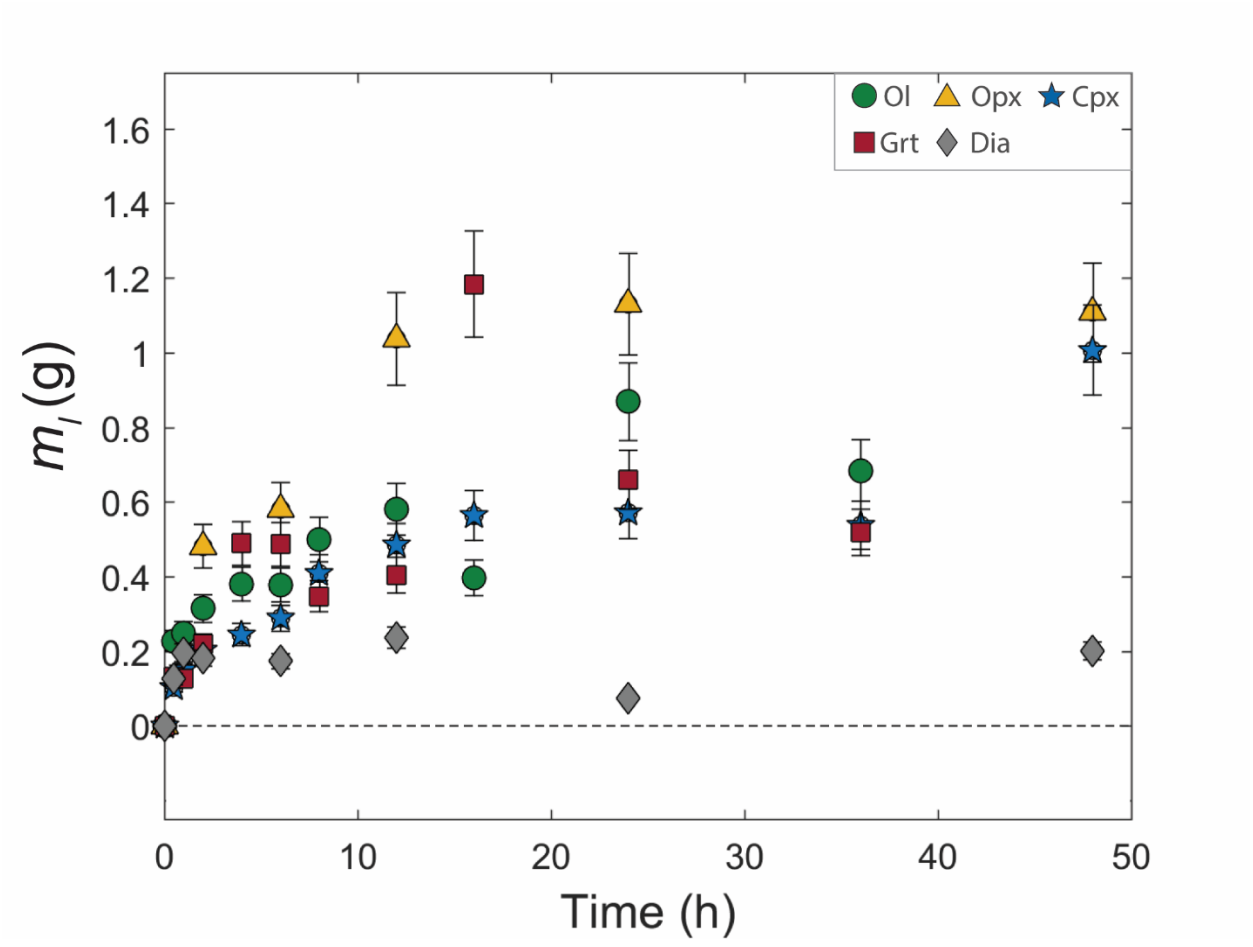

Figure 5-1. Mass loss (m_l) plotted against time for each mineral series. Uncertainty is represented as one relative standard deviation obtained from repeating experiment 1-F three times.

In this study most of the material lost is thought to be < 1 µm since the nylon filter bag mesh had a screen size (i.e. 'rating') of 1 µm. Material loss could also occur during sieving and weighing. For future studies it is recommended that a filter bag of 0.5 µm rating or lower is used and additional measures such as enclosing the filter in a case as done by Xiao et al. (2011;2012) are implemented. At the time of modifying the apparatus used by Jones & Russell (2018) and Jones et al. (2019) nylon filter bags with a rating lower than 1 µm were not available to be purchased.

The production of daughter particles serves as an effective and simple measure to quantify the attrition process (Bemrose and Bridgwater, 1987; Gwyn, 1969; Jones et al., 2019, 2017; Xiao et al., 2012). I have plotted the mass of daughter particles (m_d) relative to the total mass recovered (m_r), as a function of time t (h) for each mineral (Figure 5-2a). As in Figure 5-1, Experimental uncertainty is shown as two standard deviations obtained from repeating experiment 1-F three times (highlighted in Figure 5-2a) and applying the coefficient of variation (i.e. relative standard deviation) to all experiments.

Each set of experiments show an initial, rapid rise in production of daughter particles followed by a highly reduced rate ultimately forming a plateau, indicating little attrition. In the literature this plateau has been attributed to a stable state whereby further production of daughter particles becomes limited with increased residence time (Jones et al., 2017; Knight et al., 2014). These two key attributes of the attiriton data (initial rapid attrition followed by stable plateau) have formed the basis of an empirical model (Jones et al., 2017) with two adjustable parameters a and b:

$$\frac{m_d}{m_r} = a(1 - e^{-bt}) \qquad [5.1]$$

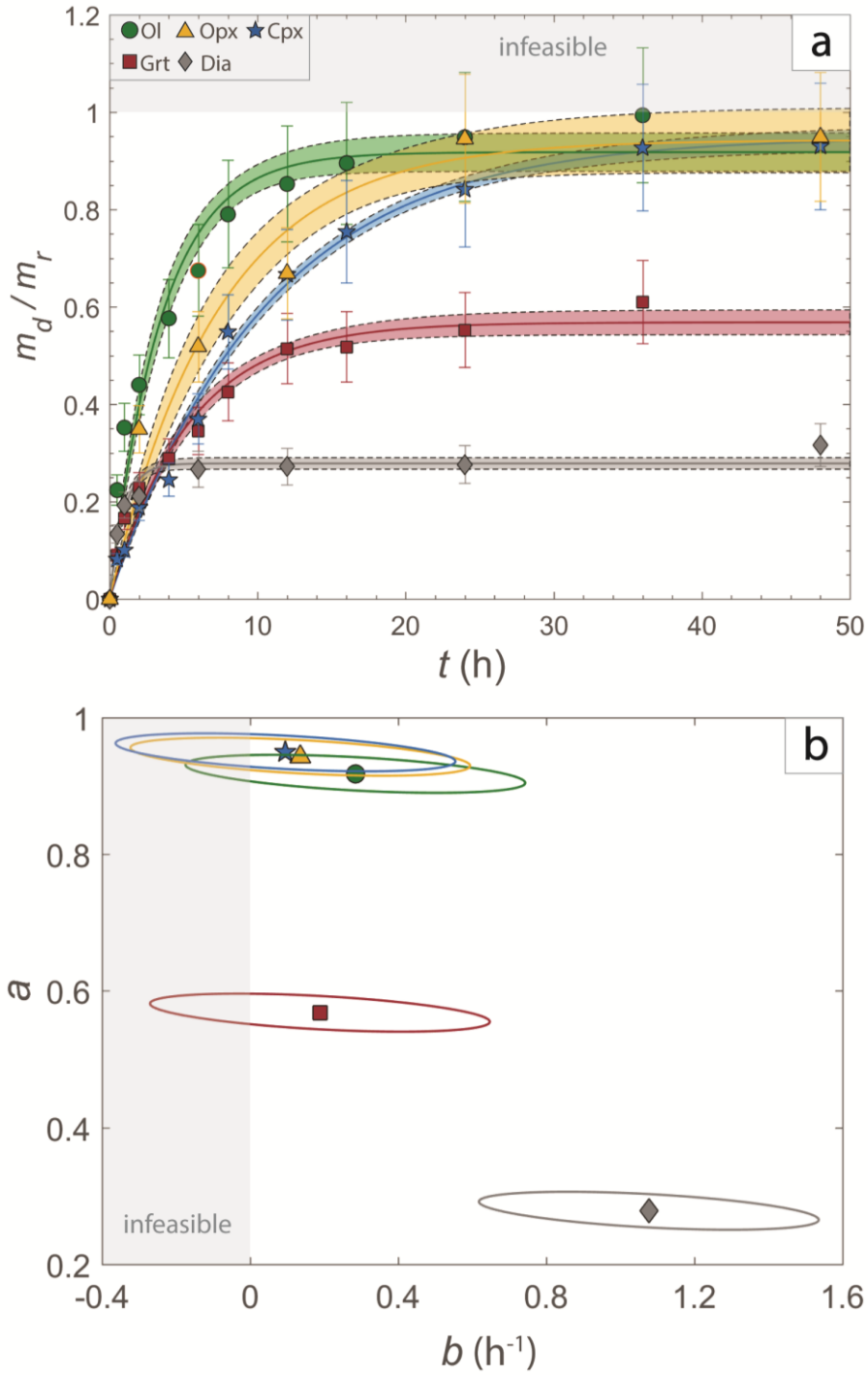

Figure 5-2. a) Proportion of daughter products (m_d) normalized to the mass recovered (m_r) plotted against time for each mineral series. Experiment 1-F is highlighted as it is used to calculate relative standard deviation. b) Model values of *a*, the infinite time limit of attrition and *b*, the attrition rate constant for all minerals. The ellipses represent a 95% confidence envelope based on the fit of equation 5-1 to the data.

The variable *a* represents the dimensionless infinite attrition time limit defining the plateau value and *b* [h^{-1}], is the attrition rate constant dictating the rate at which the limit is reached. Here I adopt this model and have fitted solid lines denote the optimal fit of equation 5.1 to each mineral series (see Table 5-2).

Mineral	***a***	***b* (h^{-1})**	**RMSE of fit**
Olivine	0.9179	0.2840	0.0708
Orthopyroxene	0.9427	0.1355	0.0793
Clinopyroxene	0.9492	0.0955	0.0312
Garnet	0.5682	0.1884	0.0381
Diamond	0.2784	1.0770	0.0231

Table 5-2. Table of model fit parameters for each mineral series. RMSE = Root Mean Square Error.

The empirical model (Equation 5.1) describes the experiment data well and confidence limits on the model enclose the dataset. Olivine, garnet and diamond have similar shaped trends, however, are clearly characterized by different attrition limits (*a*) and attrition rates (*b*). Specifically, olivine has the highest *a* value of 0.9179 followed by garnet and diamond with values of 0.5682 and 0.2784 respectively. Diamond approaches its attrition limit the fastest indicated a *b* value of 1.077 h^{-1} followed by olivine and garnet with values of 0.2840 and 0.1884 respectively. The experiment data for the two pyroxene minerals, orthopyroxene and clinopyroxene, define model fits of different shapes relative to the other minerals. The model equations have similar *a* values of 0.9427 and 0.9492 but approach the attrition limit more slowly as indicated by the lowest *b* values of 0.1355 h^{-1} and 0.09554 h^{-1} respectively.

The modelled curves proved to be better fits for some mineral series than others demonstrated by differing Root Mean Square Error (RMSE) values. Specifically, diamond has the lowest RMSE of 0.02316, followed by clinopyroxene, garnet, olivine and orthopyroxene with values of 0.0312, 0.0381, 0.0708, 0.0793 respectively.

The relationship between *a* and *b* is explored in Figure 5-2b where these parameters have been plotted against each other for each mineral with ellipses representing a 95% confidence envelope based on the fit of Equation 5.1 to the mineral series. There is no clear correlation between the attrition limit (*a*) and rate (*b*) at which this value is approached. The relationship between the *a* and *b* and the physical properties of the minerals is explored in the discussion section of this thesis.

5.1.2 Grain Size Distributions

For all minerals the parent population (grey mode; Figure 5-3) exhibits a rapid drop in abundance at early experiment durations that slows with increased time. This rapid drop in parent population is accompanied by the development of secondary modes (representing the daughter products) for each mineral. Interestingly, each mineral type has a grain size distribution with the number of modes and mode positions unique to that mineral. These characteristic distributions directly reflect the varying physical properties of each mineral.

The olivine (Figure 5-3a) parent mode decreases from 655 µm to 500 µm with increased residence time up to 6 h. At the longest duration (36 h), the mode position changes again, located at 463 µm. After 6 h a secondary daughter mode at 275 µm begins to form. Two finer modes below 100 µm at 3 µm and 65 µm exist (see inset) for a total of four modes. Orthopyroxene shows an initial rapid decline in the parent mode which moves towards a mode position of 463

µm at 24 h. At 24 h a secondary mode at 328 µm becomes very noticeable. Unlike the other minerals, orthopyroxene below 100 µm is characterized by a broad unimodal distribution centered on 6 µm for a total of three modes. I hypothesize that another peak may occur at 26 µm but given the distribution breadth it is not possible to distinguish multiple modes. Clinopyroxene shows a parent population that shifts towards a peak position of 500 µm with increased residence time. Development of a secondary mode at 275 µm is evident after 24 h. At long times (> 24 h) the parent mode broadens and is skewed to the finer grain sizes indicating possible emergence of another mode at 463 µm. Below 100 µm, two modes are identified, one at 3 µm and another at 31µm. The latter migrates towards 48 µm at long times (> 16 h). A total of four modes are identified for clinopyroxene. Garnet shows a declining parent peak which unlike the other minerals discussed does not shift. A secondary mode is observed at 275 µm starting at 16 h. Below 100 µm there exists a bimodal fines population with modes at 3 µm and 52 µm for a total of four modes. Lastly, diamond shows far less attrition than the other minerals. This is indicated by a persistent parent mode which like garnet does not shift towards a smaller mode. No notable secondary mode is observed and a relatively low volume of fines (<100 µm) is produced (note that the inset volume % scale has been lowered by an order of magnitude to see the population). Below 100 µm a bimodal population is observed, with one peak at 4 µm and another at 31µm shifting towards 78 µm at longer (24 h) residence times. A total of three modes are noted for diamond.

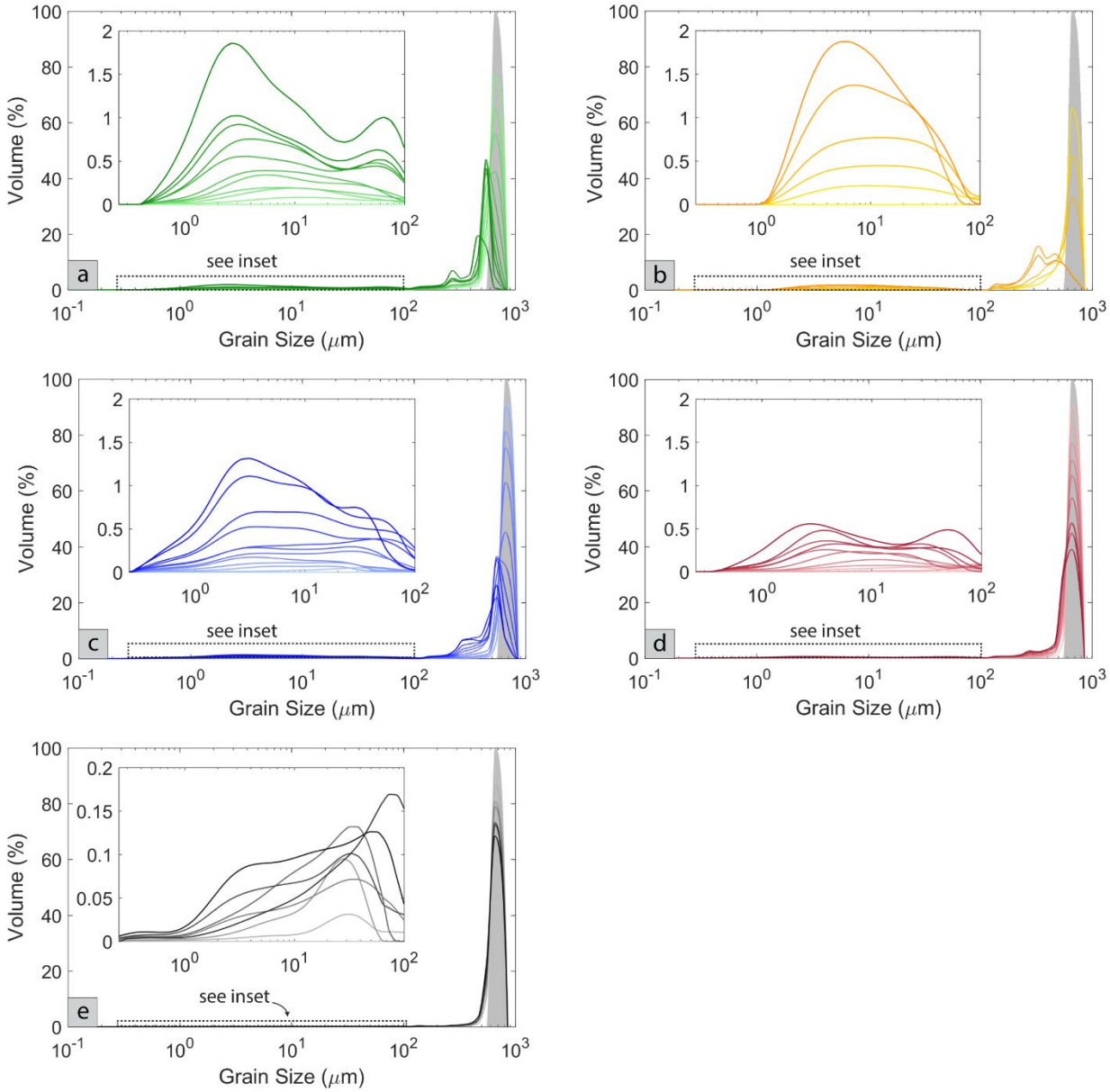

Figure 5-3. Grain size distributions for each mineral series: (a) Olivine; (b) Orthopyroxene; (c) Clinopyroxene; (d) Garnet; (e) Diamond. The starting (input) distribution is shaded in grey and the experiment run products are plotted as continuous lines which become darker with increasing experiment duration. Insets show the finer daughter products measured by laser particle size analysis (LPSA), at an enlarged scale. For the readers ease the diamond inset y-axis scale is an order of magnitude lower than the other plots to account for the low abundances of diamond daughter products. The complete particle size dataset can be found in Appendix C.1.

5.1.3 Experiment Observations / Videography

Highspeed videography confirms that the individual minerals were subject to the same dynamic conditions in each experiment. Specifically, particles were homogeneously distributed throughout the column and able to move freely relative to neighboring particles. These observations are consistent with a pneumatic flow regime (Bi and Grace, 1995; Grace, 1986; Jones et al., 2019; Kunii et al., 1969) operating under turbulent flow conditions. The initial bed height (h_0), the column height (h_p) and particle concentration (φ_{Jones}, φ) were recorded and are reported (Table 5-3). In this study, particle concentration (φ) is derived using a calculated initial bed height ($h_{0\ calc}$). This is done by converting the initial mass [g] to a bed height [mm] by using the mineral density and cross-sectional area of the attrition tube. To arrive at a dimensionless measure of particle concentration, the bed height is divided by the measured fluidized bed height (h_p). φ_{Jones} is provided for reference and is calculated by dividing the measured bed height ($h_{0\ meas}$) by h_p.

Experiment Series	Mineral	Time (h)	$h_{0\ meas}$ (mm)	$h_{0\ calc}$ (mm)	h_p (mm)	φ_{Jones}	φ
1-A	Ol	0					
1-B	Ol	0.5	8.260	4.803	210.0	0.03933	0.02287
1-C	Ol	1	8.260	4.803	205.0	0.04029	0.02343
1-D	Ol	2	8.260	4.803	220.0	0.03755	0.02183
1-E	Ol	4	8.260	4.803	215.0	0.03842	0.02234
1-F1	Ol	6	8.260	4.803	205.0	0.04029	0.02343
1-F2	Ol	6	8.260	4.803	212.5	0.03887	0.02260
1-F3	Ol	6	8.260	4.803	210.0	0.03933	0.02287
1-G	Ol	8	8.260	4.803	212.5	0.03887	0.02260
1-H	Ol	12	8.260	4.803	210.0	0.03933	0.02287
1-I	Ol	16	8.260	4.803	200.0	0.0413	0.02401
1-J	Ol	24	8.260	4.803	205.0	0.04029	0.02343
1-K	Ol	36	8.260	4.803	207.5	0.03981	0.02314

2-A	Opx	0					
2-B	Opx	2	8.279	4.826	215.0	0.03851	0.02245
2-C	Opx	6	8.279	4.826	220.0	0.03763	0.02194
2-D	Opx	12	8.279	4.826	220.0	0.03763	0.02194
2-E	Opx	24	8.279	4.826	215.0	0.03851	0.02245
2-F	Opx	48	8.279	4.826	220.0	0.03763	0.02194
3-A	Cpx	0					
3-B	Cpx	0.5	8.273	4.739	210.0	0.0394	0.02257
3-C	Cpx	1	8.273	4.739	205.0	0.04036	0.02312
3-D	Cpx	2	8.273	4.739	210.0	0.0394	0.02257
3-E	Cpx	4	8.273	4.739	207.5	0.03987	0.02284
3-F	Cpx	6	8.273	4.739	212.5	0.03893	0.02230
3-G	Cpx	8	8.273	4.739	200.0	0.04137	0.02369
3-H	Cpx	12	8.273	4.739	210.0	0.0394	0.02257
3-I	Cpx	16	8.273	4.739	210.0	0.0394	0.02257
3-J	Cpx	24	8.273	4.739	212.5	0.03893	0.02230
3-K	Cpx	36	8.273	4.739	212.5	0.03893	0.02230
3-L	Cpx	48	8.273	4.739	212.5	0.03893	0.02230
4-A	Grt	0					
4-B	Grt	0.5	7.223	4.007	175.0	0.04127	0.02290
4-C	Grt	1	7.223	4.007	175.0	0.04127	0.02290
4-D	Grt	2	7.223	4.007	175.0	0.04127	0.02290
4-E	Grt	4	7.223	4.007	175.0	0.04127	0.02290
4-F	Grt	6	7.223	4.007	172.5	0.04187	0.02323
4-G	Grt	8	7.223	4.007	170.0	0.04249	0.02357
4-H	Grt	12	7.223	4.007	170.0	0.04249	0.02357
4-I	Grt	16	7.223	4.007	175.0	0.04127	0.02290
4-J	Grt	24	7.223	4.007	170.0	0.04249	0.02357
4-K	Grt	36	7.223	4.007	165.0	0.04378	0.02429
5-A	Dia	0					
5-B	Dia	0.5	7.824	4.444	185.0	0.04229	0.02402
5-C	Dia	1	7.824	4.444	190.0	0.04118	0.02339
5-D	Dia	2	7.824	4.444	190.0	0.04118	0.02339
5-E	Dia	6	7.824	4.444	185.0	0.04229	0.02402
5-F	Dia	12	7.824	4.444	190.0	0.04118	0.02339
5-G	Dia	24	7.824	4.444	190.0	0.04118	0.02339
5-H	Dia	48	7.824	4.444	195.0	0.04012	0.02279

Table 5-3. Height data collected from each experiment. h_0 is the initial bed height, h_p is the height of the fluidized column and φ, a metric for particle concentration is calculated as h_0/h_p.

Average h_p and φ values are plotted against mineral density in Figure 5-4a,b revealing a negative correlation between column height and density (Figure 5-4a) and a positive correlation between particle concentration and density (Figure 5-4b). Specifically, orthopyroxene had the largest column height of 209.4 ± 5.3 mm, followed by olivine, clinopyroxene, diamond and garnet with h_p values of 218.0 ± 2.7, 209.3 ± 3.9, 189.3 ± 3.5 and 172.3 ± 3.4 mm respectively. This resulted in average particle concentrations (Figure 5-4b) of, 0.02214 ± 0.00028, 0.02295 ± 0.00058, 0.02265± 0.00043, 0.02348 ± 0.00043 and 0.02327 ± 0.00047.

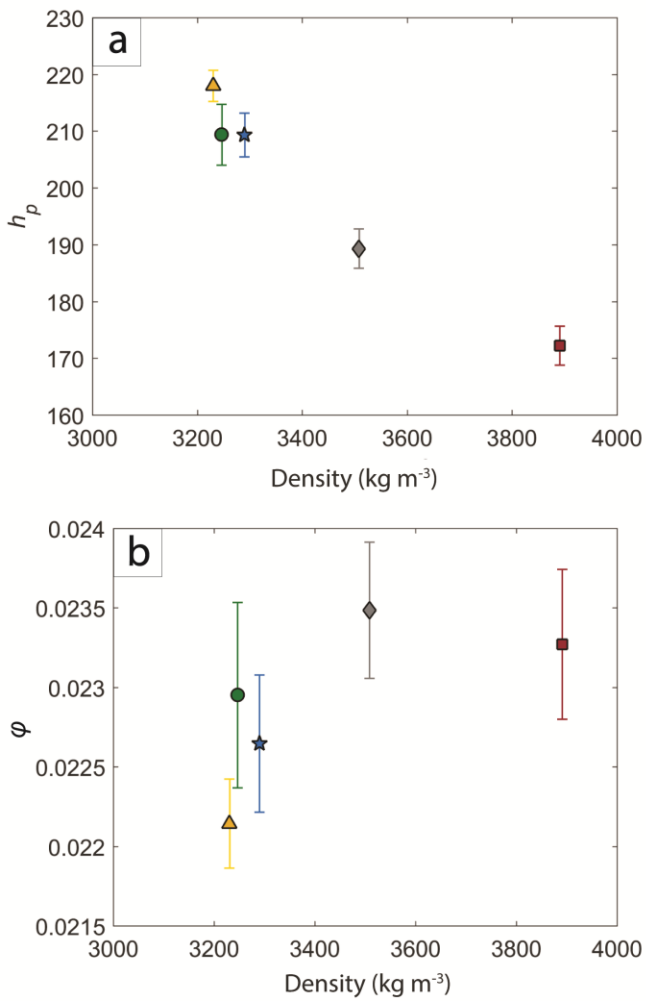

Figure 5-4. a) Column height (h_p) plotted against mineral density for each mineral. b) Particle concentration (φ) plotted against density for each mineral. Symbology is consistent with that used in previous figures.

Upon detailed examination of the high-speed videography, particle motion within the tube is not entirely random. Specifically, the central region of the tube is dominated by an upward stream of relatively fast-moving particles, which contrasts particle motion at the tube margins where particles travel predominantly downwards at slower velocities.

Between 142 and 166 particles were tracked over 2-10 frames for a representative experiment from each mineral type with roughly 120 particles tracked in the central region and 30 particles tracked at the margins of the attrition tube. This ratio of particles tracked in the central to the margins is proportional to the particle volume observed across the width of the tube whereby approximately 70% of the particle volume lies in the upward moving jet and 30% at the margins. The particle tracking results for each mineral are visualized in Figure 5-5a-e which includes a plot of particle velocity for each tracked particle, a histogram plot binning the raw velocity data in bins with a width of 0.2 m s^{-1} and a contour plot of velocity distribution within the tube. The histogram plots for each mineral show a bimodal distribution with one mode at a positive velocity and another mode at a negative velocity. The velocity contours for each mineral show a central jet characterized by relatively large, positive velocities (‘hot’ colors) and negative velocities (‘cold’ colors) at the margins of the tube.

Results are summarized in Table 5-4 which includes, differential velocity (Δv) and an approximate maximum differential velocity. Average velocities are similar between the mineral types and have a maximum difference of 13%.

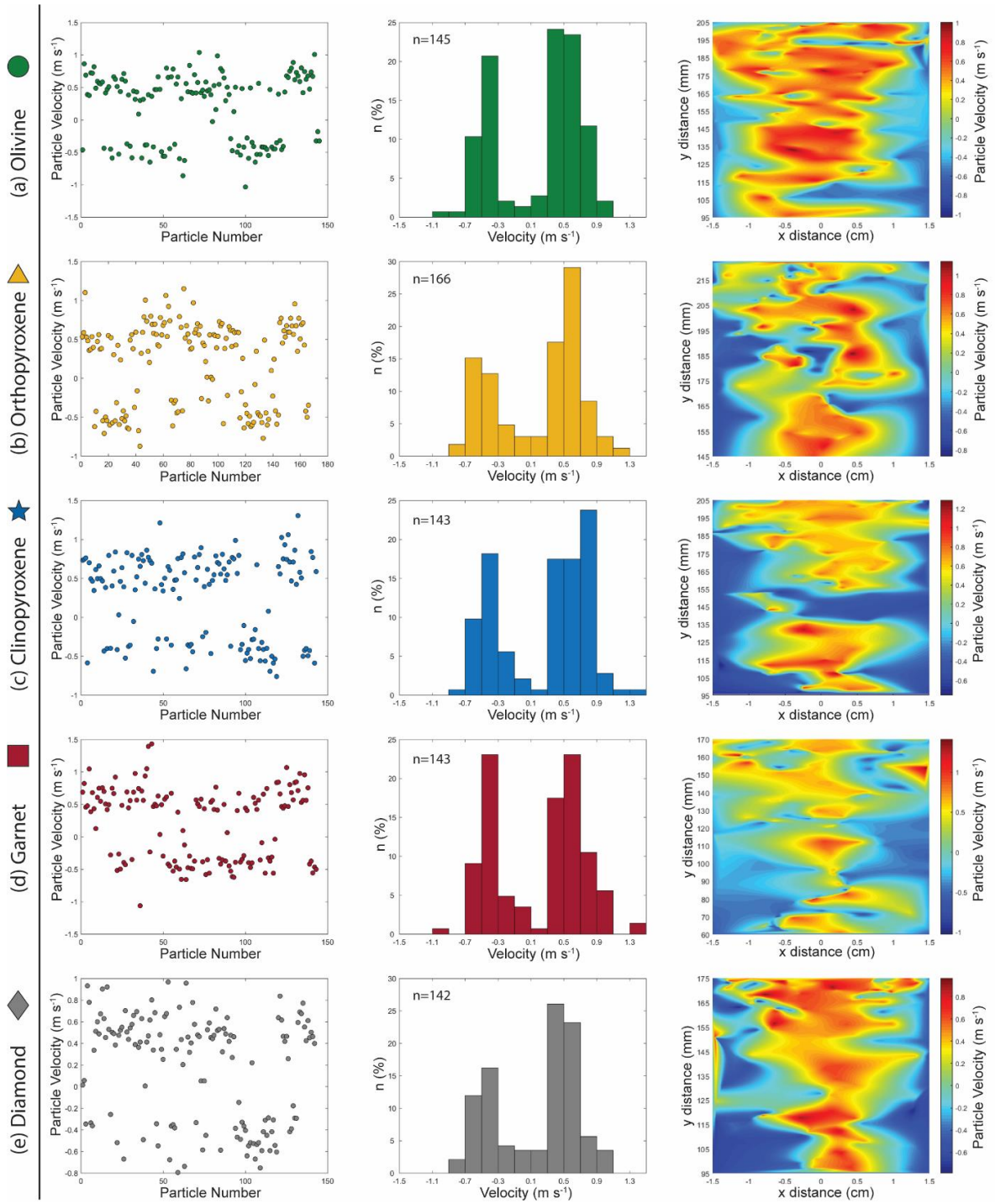

Figure 5-5. Particle tracking results for a) Olivine, b) Orthopyroxene, c) Clinopyroxene, d) Garnet, e) Diamond. Left: Raw particle velocity values for each particle tracked. Center: Velocity values plotted as histograms with 0.2 m s^{-1} bin width. Right: Velocity distribution within the attrition tube, y is the distance above the base of the tube (mm) and x is the distance across the tube.

	n	v_{ave} (m s^{-1})	v_{mode} [peak 1, peak 2] (m s^{-1})	Δv [peak 2 – peak 1] (m s^{-1})	Max Diff. Velocity (m s^{-1})
Olivine	145	0.526±0.179	-0.4, 0.4	1.0	2.2
Orthopyroxene	166	0.527±0.196	-0.6, 0.6	1.0	2.2
Clinopyroxene	143	0.561±0.216	-0.4, 0.8	1.2	2.4
Garnet	143	0.542±0.229	-0.4, 0.6	1.0	2.6
Diamond	142	0.493±0.184	-0.4, 0.4	1.0	2.0

Table 5-4. Particle tracking results for each mineral: n, the number of particles tracked, the average of the absolute value of all particle velocities (v_{ave}), the mode velocities of the histogram data (v_{mode}) presented in Figure 5-5, differential velocity (Δv) which is approximated by taking the difference between the two peak velocities and maximum differential is taken as the range of the histogram distribution

A common metric of interest in fluidized bed experiments is the dimensionless slip ratio (Clift R., Grace J.R., 1999; Smolders and Baeyens, 1998; Zhang et al., 2017), s:

$$s = \frac{v_p}{U} \qquad [5.2]$$

where U is the superficial gas velocity and v_p is the particle velocity. A value of 1 implies that the particles and gas are perfectly coupled and anything lower results from lower particle velocities relative to the gas. The slip ratio has been used to approximate velocities when they cannot be measured directly. In my experiments that use a superficial gas velocity of 1.819 m s^{-1}, and have average particle velocities reported in Table 5-4, the slip ratios for olivine, orthopyroxene, clinopyroxene, garnet and diamond are calculated as 0.289 ± 0.098, 0.290 ± 0.108, 0.308 ± 0.119, 0.298 ± 0.126, 0.27 ± 0.101. I attribute this poor coupling to the high mineral densities characteristic of mantle origin.

5.1.4 Grain Shapes and Surfaces

Representative 2-D parent particle binary images for each mineral are shown in Figure 5-6 for select experiment durations of 0 h, 0.5 h, 2 h, 6 h, 12 h, 24 h. Irrespective of mineral type, the input particles (0 h) have a high degree of angularity and an irregular shape.

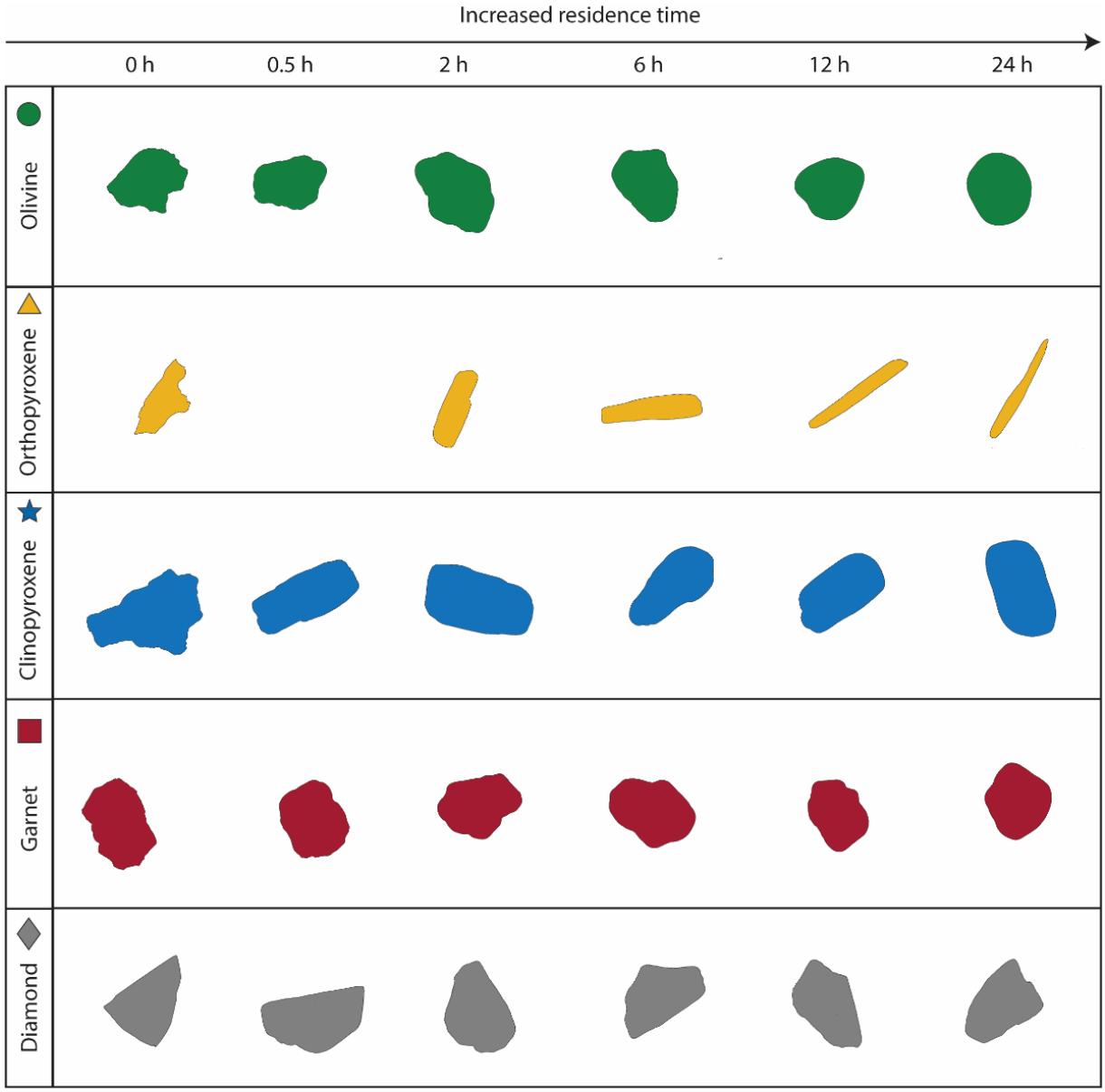

Figure 5-6. Representative parent particle binary images for each mineral at select experiment durations ranging from 0 h to 24 h. Note that no experiment was conducted at 0.5 h for orthopyroxene.

In the first two hours of attrition, the particles rapidly lose asperities and the overall morphologies become increasingly convex. Changes in particle shape decrease as residence time increases. Olivine and garnet become more circular in shape with an axial ratio close to 1 whereas clinopyroxene and orthopyroxene develop more uneven axes lengths and thus have a lower axial ratio. Diamond undergoes the lowest degree of modification, with a slight increase in convexity being the only notable change.

Particle irregularity is observed at two scales: textural roughness (a perimeter based approached that is sensitive to asperities along edges) and a morphological roughness (an area-based approach that is sensitive to corner asperities). Two metrics were chosen to quantify these observations.

The first metric utilized was solidity (S):

$$S = \frac{A_{image}}{A_{CH}} \qquad [5.3]$$

Solidity is an area scale measure of roughness, bounded by 0 and 1 (Buckland et al., 2018; Campbell et al., 2013; Cioni et al., 2014; Liu et al., 2015). Shapes whose areas can completely fill the area bounded by the convex hull have solidity, $S = 1$ and irregular shapes with numerous large asperities will have $S << 1$. Solidity serves as a preferred metric to assess the overall roundness of a particle since rounded, elongate particles can have a low circularity value but a high solidity.

The second metric employed was convexity (C_{vx}):

$$C_{vx} = \frac{P_{CH}}{P_{image}} \qquad [5.4]$$

Convexity is a perimeter scale measure of roughness bounded by 0 and 1 where values close to 1 indicate a highly convex object (Buckland et al., 2018; Jones et al., 2016; Liu et al., 2015). Particles with rough, irregular surfaces will have a larger perimeter relative to that of the convex hull and therefore a lower convexity.

Additionally, to aid further comparison with other studies I also calculated the shape factor: circularity (*C*), a measure of how close the shape mathematically approximates a circle and commonly referred to as a particle's form factor (Buckland et al., 2018; Liu et al., 2015; Manga et al., 2011):

$$C = \frac{4\,\pi\,A_{image}}{\left(P_{image}\right)^2} \qquad [5.5]$$

C is bounded by 0 and 1 where $C = 1$ represents a perfect circular object and $C << 1$ denotes irregular, angular, or highly elongate objects. This metric was partly chosen due to its wide spread use a shape metric to assess the extent of rounding in nature, i.e. volcanic systems (Andronico et al., 2014; Coltelli et al., 2008; Jones and Russell, 2018; Liu et al., 2015; Manga et al., 2011) and sedimentological processes (Cox, 1927; Novák-Szabó et al., 2018; Polakowski et al., 2014; Takashimizu and Iiyoshi, 2016). On that basis the results can be compared with data obtained from other natural systems where attrition operates.

These metrics are plotted against time in Figure 5-7a-c (marker symbology is consistent with previous figures) and summarized in Table 5-5. As with the trend of daughter particle production presented in Figure 5-2, change is rapid at shorter timescales and substantially slows at longer residence times. For certain metrics orthopyroxene seems to defy this trend which is further explored in Figure 5-8.

For solidity (Figure 5-7a), all values initially increase followed by a plateau. As morphology becomes more uniform, lower standard deviations are recorded at 24 h for all minerals except diamond. Both olivine and garnet are observed to dip in value at 2 h which rises again at the next recorded time (6 h). Orthopyroxene's solidity value decreases after 6 h and at 12 h plateaus to the same value as time 0 h. Higher convexities and lower standard deviations are noted at 24 h for all minerals (Figure 5-7b). Diamond loses convexity at short residence times (< 2 h) which begins increasing again after 2 h. All minerals became more circular with time with a rapid increase occurring after just 0.5 h which then gradually stabilizes (Figure 5-7c). Standard deviations decrease for all minerals at 24 h other than orthopyroxene. Orthopyroxene's circularity begins to change after 2 h, then plateaus at a lower value. Interestingly, as with convexity, at 2 h both olivine and garnet circularity values drop slightly.

The fact that almost all minerals end with higher solidity (except orthopyroxene) and convexity shows that through attrition parent particles become rounded. The reduction in convexity at early residence times (< 6 h) while increasing solidity values is attributed to particles losing edge asperities (at the area-scale) however gaining surface roughness as impacts cause smaller scale (perimeter-scale) indentations. This effect is particularly noticeable with diamond which starts with very straight edges (Figure 5-6) and in the process of becoming rounded, the surface appears more irregular. However, as the corners are removed, increases in convexity occur with longer residence times.

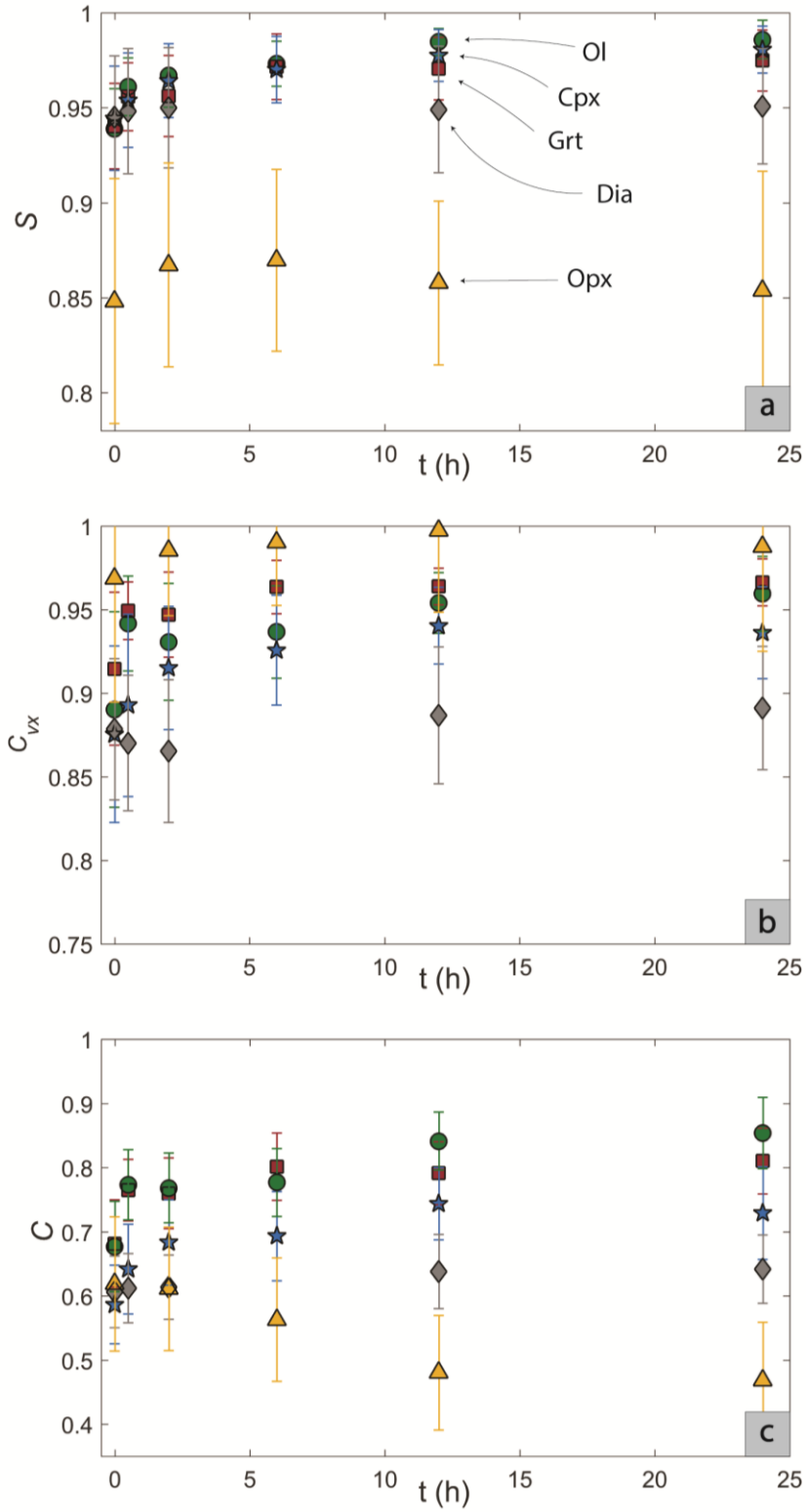

Figure 5-7. a) Solidity, b) Convexity, c) Circularity plotted against time (h). Colors and symbology are consistent with previous figures.

		C	S	C_{vx}
Olivine	0 h 24 h	0.68 ± 0.10, 0.85 ± 0.06	0.94 ± 0.02, 0.99 ± 0.01	0.89 ± 0.07, 0.96 ± 0.02
Orthopyroxene	0 h 24 h	0.62 ± 0.17, 0.47 ± 0.19	0.85 ± 0.08, 0.85 ± 0.07	0.97 ± 0.08, 0.99 ± 0.06
Clinopyroxene	0 h 24 h	0.59 ± 0.10, 0.73 ± 0.10	0.94 ± 0.03, 0.98 ± 0.01	0.88 ± 0.06, 0.94 ± 0.03
Garnet	0 h 24 h	0.68 ± 0.10, 0.81 ± 0.06	0.94 ± 0.02, 0.97 ± 0.02	0.91 ± 0.05, 0.97 ± 0.01
Diamond	0 h 24 h	0.61 ± 0.09, 0.64 ± 0.09	0.94 ± 0.03, 0.95 ± 0.04	0.88 ± 0.05, 0.89 ± 0.05

Table 5-5. Summary of the change in circularity (*C*), solidity (*S*) and convexity (C_{vx}) for each mineral from 0 h to 24 h

Orthopyroxene shows the most difference compared to the other mineral trends in circularity which is attributed to a combination of preferred breakage along cleavage planes and a lamellar, acicular habit causing elongation with increased attrition. The degree of elongation can be quantified using the axial ratio (*A*):

$$A = \frac{b_{image}}{a_{image}} \qquad [5.6]$$

Where b_{image} is the minor (short) axis and a_{image} is the major (long) axis of the mineral's binary image. The ratio is bounded from 0 to 1 where values close to 1 indicate a highly equant object and elongated objects will have $A << 1$. The relationship between circularity (*C*) and axial ratio (*A*) is visualized and applied to orthopyroxene and olivine in Figure 5-8. Olivine and orthopyroxene show contrasting trends whereby olivine responds to attrition by becoming more circular, thereby also attaining a higher axial ratio. Orthopyroxene shows a dramatic drop in axial ratio as the particles break along cleavage planes and therefore also become less circular.

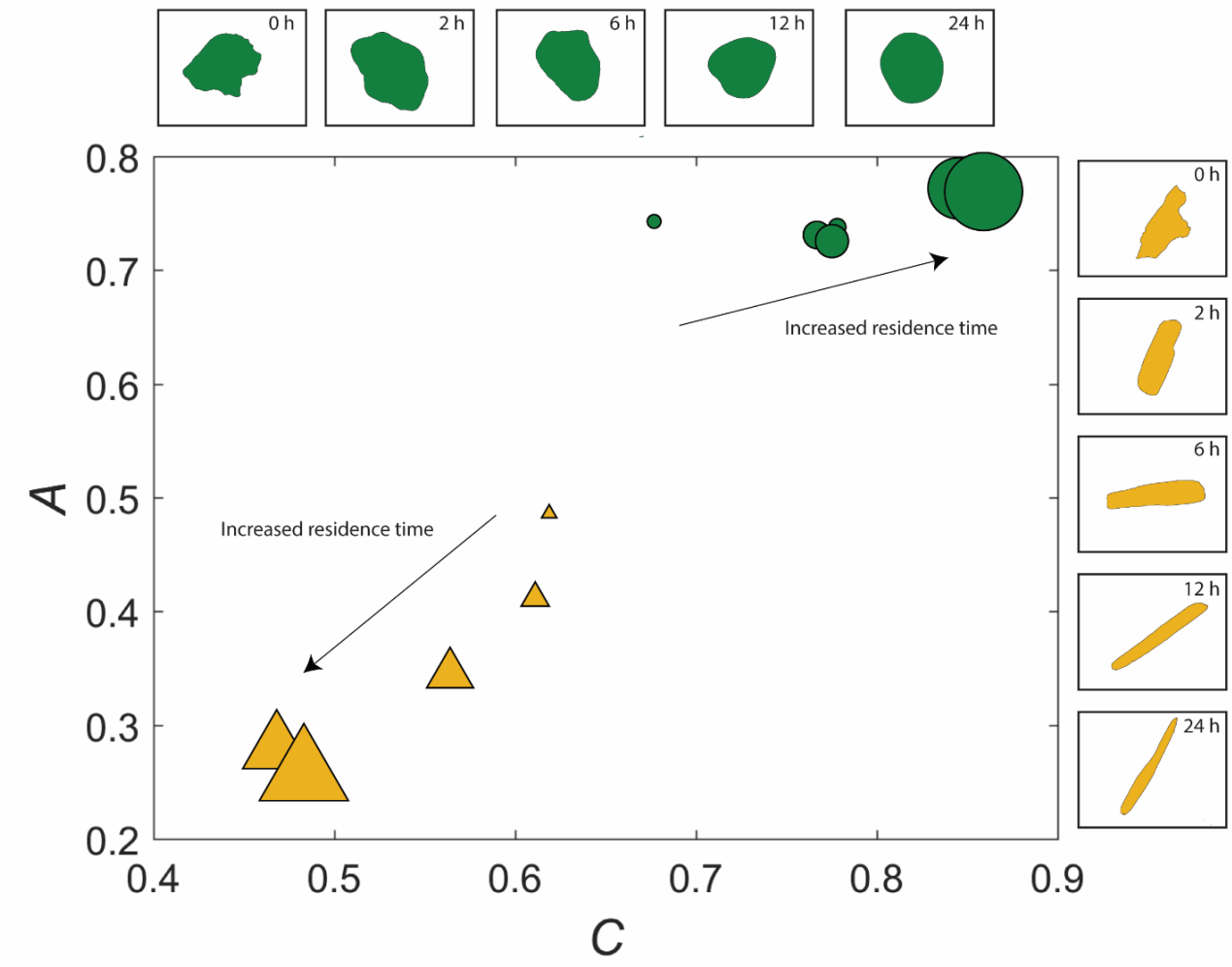

Figure 5-8. Axial ratio (*A*) plotted against circularity (*C*) for olivine (green) and orthopyroxene (yellow). Marker size is proportional to experiment duration, larger symbols denote longer experiments. Colors and symbols are consistent with previous figures. Representative binary images of the experiments are shown for reference.

Expanding upon the 2-D shape results, SEM images of parent grain morphologies and surfaces are presented in Figure 5-9 and Figure 5-10 respectively, where the rows represent the mineral type and columns indicate the experiment duration (h).

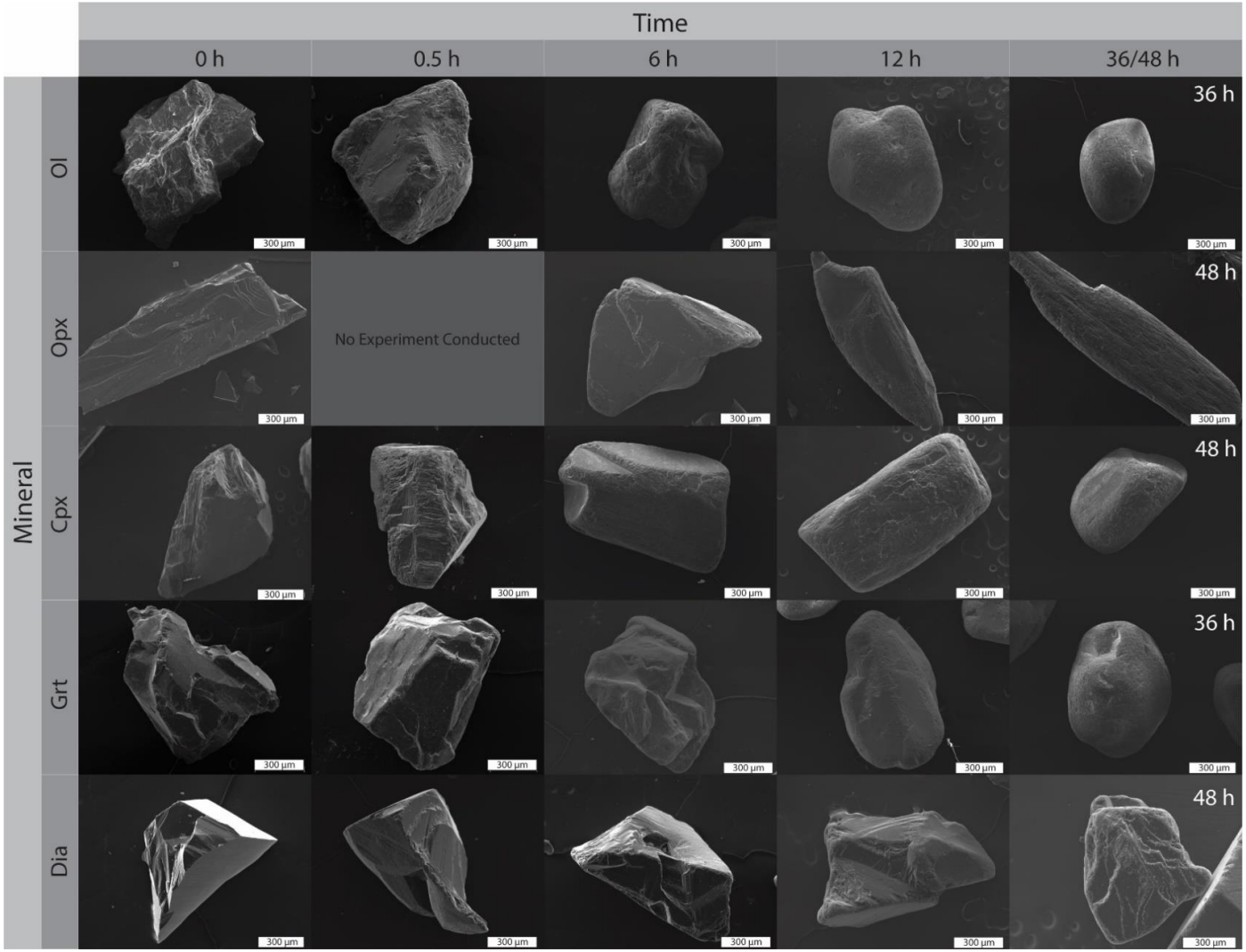

Figure 5-9. SEM images (in Secondary Electron mode) of representative parent particle morphology at select experiment durations. Rows represent different minerals and columns denote experiment duration.

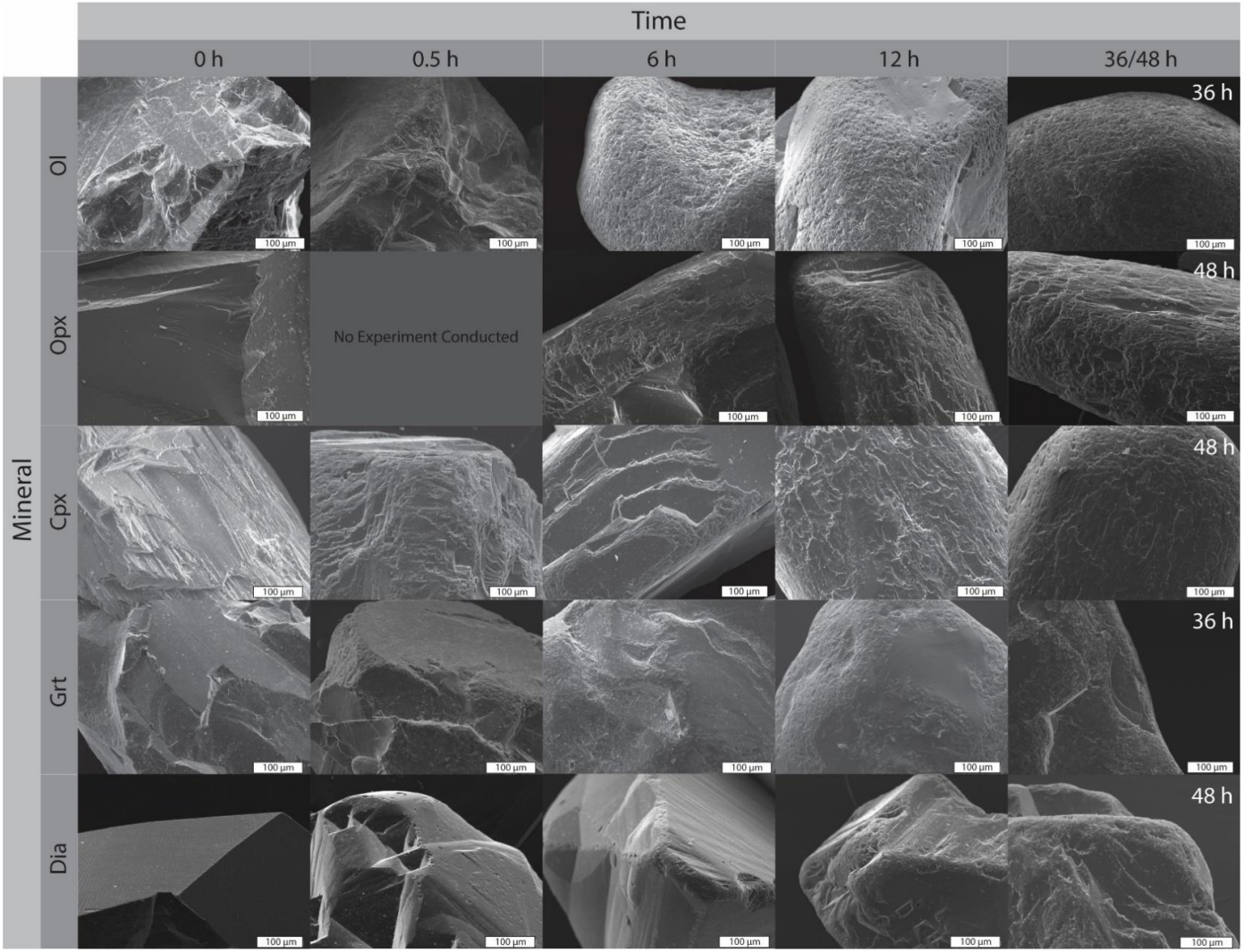

Figure 5-10. SEM images of representative parent particle surfaces at select experiment duration. Rows represent different minerals and columns denote experiment duration.

All mineral grains begin with angular morphologies and smooth surfaces which transition towards rounded morphologies with rough surfaces. Olivine undergoes the most efficient modification as shown by the roughest surfaces and highly convex morphologies. Orthopyroxene and clinopyroxene show distinct cleavage-controlled disruption with planar breakage planes (Figure 5-10) and a low axial ratio (Figure 5-9). Garnet shows clear conchoidal fracture and a morphology at 24 h like that of olivine, however with less pronounced convexity and surface roughness. Starting diamond particles show perfectly straight edges and flawless surfaces controlled by the mineral's perfect cleavage. The rounding of diamond is much less evident than the other minerals and surfaces appear less rough.

To analyze the surface features left behind by particle impacts (i.e. attrition), Figure 5-11(left) shows smaller scale (<20 µm) surface depressions that result from lower energy, but more frequent collisions (Jones et al., 2019, 2014; Kueppers et al., 2012; Xiao et al., 2012, 2011) and Figure 5-11(right) shows larger scale (>100 µm) impact features interpreted to result from higher energy collisions (Campbell et al., 2013; Dufek et al., 2012; Jones et al., 2014). The nature of the impact features shown in Figure 5-11 vary by mineral type and to an extent are controlled by cleavage. For example, olivine and garnet have impact depressions and excavations categorized by hemispherical morphologies with a smooth interior and a seemingly random orientation. By contrast, orthopyroxene, clinopyroxene and diamond show a higher degree of flaking and layering with impact pits appearing more elongated. Flaking at and beneath the exterior surface is not restricted to cleavage and is also observed, although less frequently, in both olivine and garnet. Other authors have identified these subsurface textures and flaky surfaces as a stress release mechanism in response to either decompression or heating (Campbell et al., 2013; Jones et al., 2014; Little et al., 2017). This feature is most common in diamond and

has been documented in natural diamonds and interpreted as brittle fracturing during syn and post transport within the kimberlite magma (Win et al., 2001). Impact features observed in Figure 5-11 (right) are characterized by smooth interiors as noted with Figure 5-11 (left) although have more angular morphologies, straight edges and often reveal breakage planes beneath the surface. At this scale (100 µm), the conchoidal fracture of garnet characterized by curved surfaces becomes particularity noticeable.

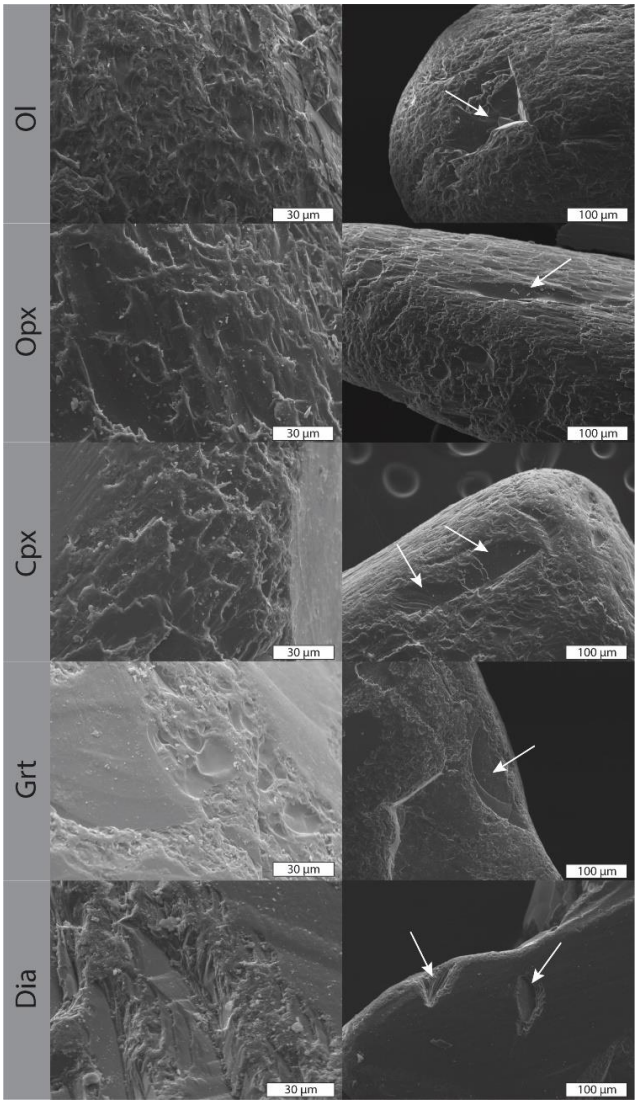

Figure 5-11. Left: Smaller scale impact features (< 20 µm) associated with surface roughness. Right: Arrows pointing at larger impact features (> 100 µm) interpreted to result from higher energy collisions.

The characteristics of the daughter particles (i.e. size and morphology) that form as a result of fragmentation and abrasion is dependent upon the mineral type and the collisional energy. The grain size distributions (Section 5.1.2) showed unique distributions for each mineral, distinguishable by the number of modes, mode shapes and mode positions. To gain further insight into the nature of these particles, for each mineral, daughter modes identified in the grain size distributions (Figure 5-3; Table 5-6) were analyzed using SEM imagery.

Olivine	Orthopyroxene	Clinopyroxene	Garnet	Diamond
<125, 250, 425, 500	<125, 125, 300, 425	<125, 250, 425, 500	<125, 250	<125

Table 5-6. Sieve fraction sizes (µm) selected for SEM imagery of daughter particles.

The images of the daughter modes are presented in Figure 5-12 and Figure 5-13 for short and long experiment durations respectively. The images are valuable in that they give insight into the likely formation of the particles. For instance, for the shortest duration (0.5 h), regardless of the mineral type, both the 500 – 600 µm and the 425 – 500 µm modes of olivine, orthopyroxene and garnet closely resemble the parent particles shown in Figure 5-9 in terms of morphology and surface features. On that basis, these particles are interpreted to be parent particles which, in the process of rounding have lost corners, reducing their diameter by ~100 - 200 µm. The orthopyroxene grains within the 300 – 355 µm sieve also contain fragmentation products since the grains begin showing fresh fracture surfaces across the long axis of the grain indicating wholesale fracturing (i.e. fragmentation). This feature becomes ubiquitous in the 250 – 300 µm and the 125-150 µm sieve fractions suggesting that these modes formed as a result of early fragmentation of parent particles. The particle images below 125 µm show larger chips and

fines and are interpreted to form as a result of abrasion of parent and daughter particles. This agrees with the grain size distributions which all show a bimodal distribution and confirms the hypothesis made earlier that the wide fine (< 100 µm) distribution of orthopyroxene is likely two merged distributions.

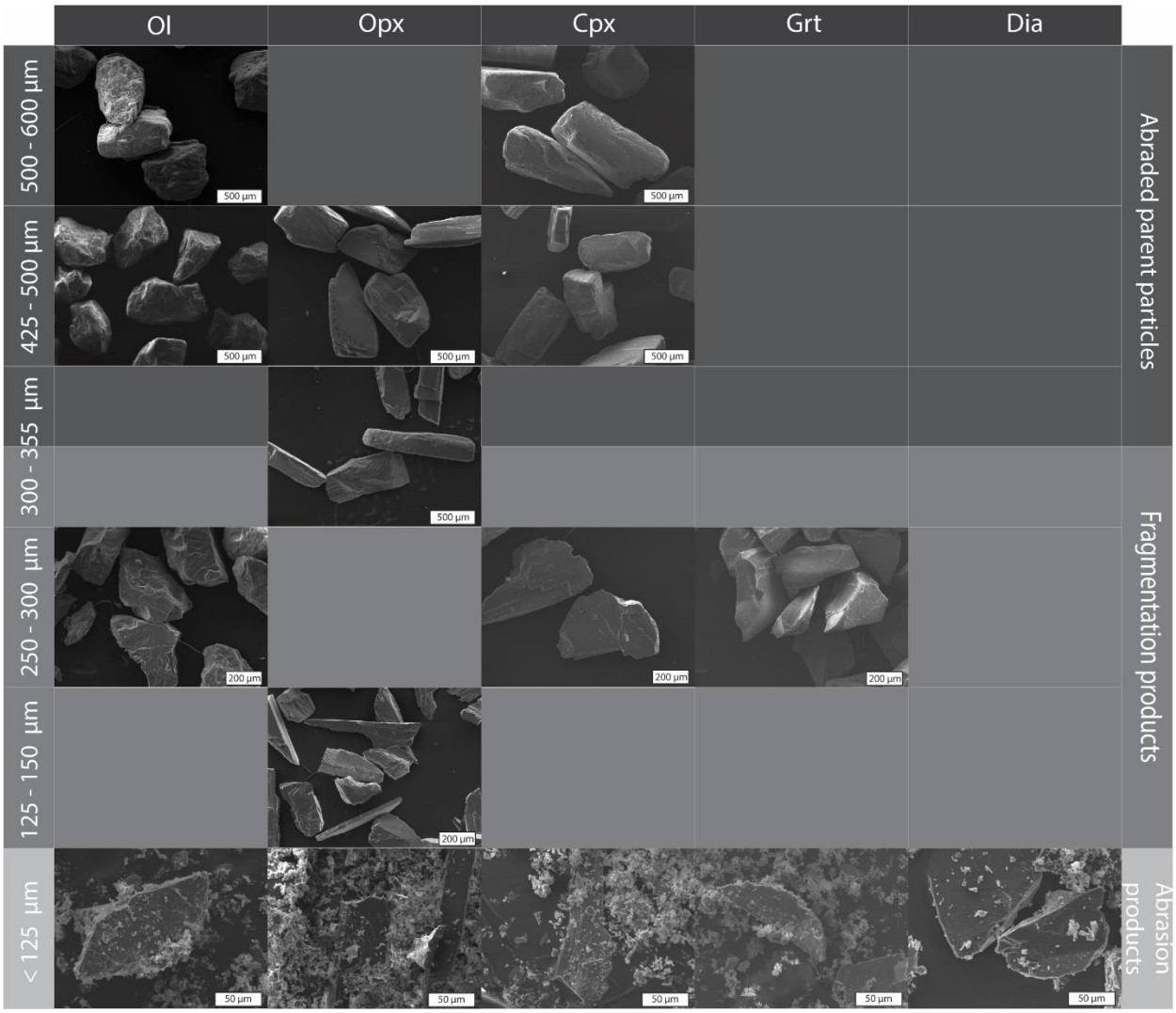

Figure 5-12. Daughter products from individual sieve fractions (see Table 5-6) for each mineral for the shortest experiment times. Rows show sieve fraction size and columns show mineral type. All images taken at 0.5 h except Opx whose shortest experiment is 2 h. Sieve fractions are classified by formation: Abraded parent particles, fragmentation products and abrasion products. Opx was found to have both fragmented parent and abraded parent particles in the 300 – 355 µm bin.

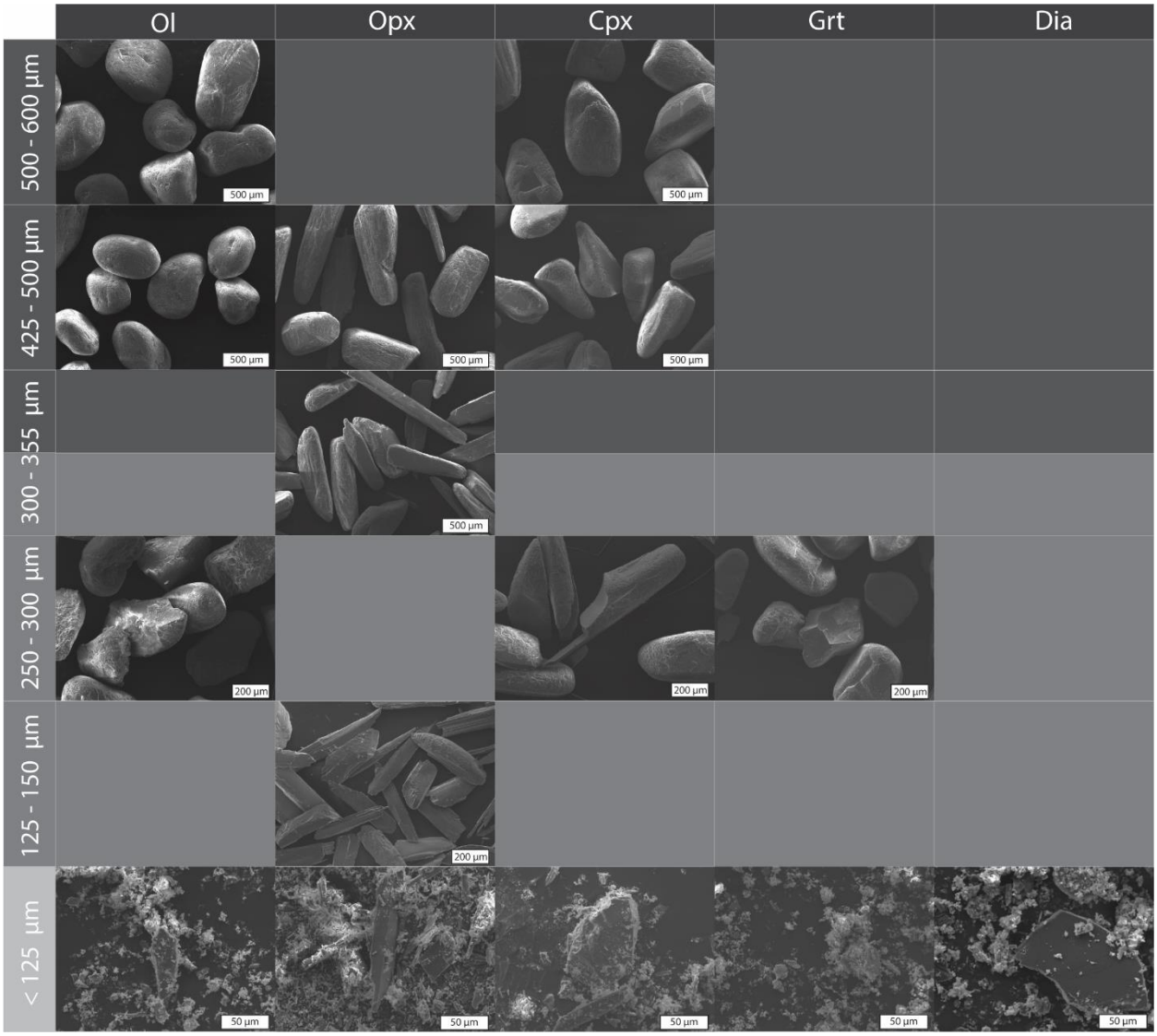

Figure 5-13. Daughter products from mode sieve fractions for each mineral for the longest common experiment duration of 24 h. Shading is consistent with that in Figure 5-12.

For the long duration (24 h; Figure 5-13) it is observed that rounding is most pronounced in grains measuring 425 to 600 µm. In the 125 – 300 µm range multiple generations of fracturing are visible, noted by breakage planes displaying varying degrees of overprinting impact features. Late fracturing is also observed on numerous particles whereby well-rounded particles display fresh breakage surfaces cross cutting the particle axis. The fines fraction (<125 µm) undergoes

no observable change in morphology. The reason is because these particles are elutriated from the system at inception and do not have time to be further modified.

5.2 Attrition of Mineral Mixtures

In the engineering sciences, it has been shown that the attrition of binary mixtures is influenced by the contrasting physical properties of each particulate solid and their relative proportions (Gravina et al., 2004; Kim et al., 2019; Marzocchella et al., 2000; Ray et al., 1987). Most geological systems, including the natural kimberlite dyke host multiphase mineral mixtures (Brett et al., 2015; Scott Smith et al., 2013) with initial proportions governed by the modal distribution present in the sampled mantle. On that basis, I performed two sets of binary mixture experiments to investigate the influence of contrasting physical properties on multiphase mineral attrition. The two sets of experiments included an olivine-garnet series and an olivine-clinopyroxene series with both minerals in equal mass proportions. Olivine was used for both sets of experiments since it is the dominant mineral phase in kimberlites (Giuliani, 2018; Moss et al., 2010; Scott Smith, 2008). Garnet (no cleavage) and clinopyroxene (two sets of cleavage) were chosen to investigate if the presence of cleavage in mixtures influences breakage. The results are presented in Figure 5-14a and Figure 5-14b for the olivine-garnet and olivine-clinopyroxene binary mixtures respectively, where the ratio of daughter products to the total (m_d / m_r) is plotted against time for a short, medium and long experiment duration.

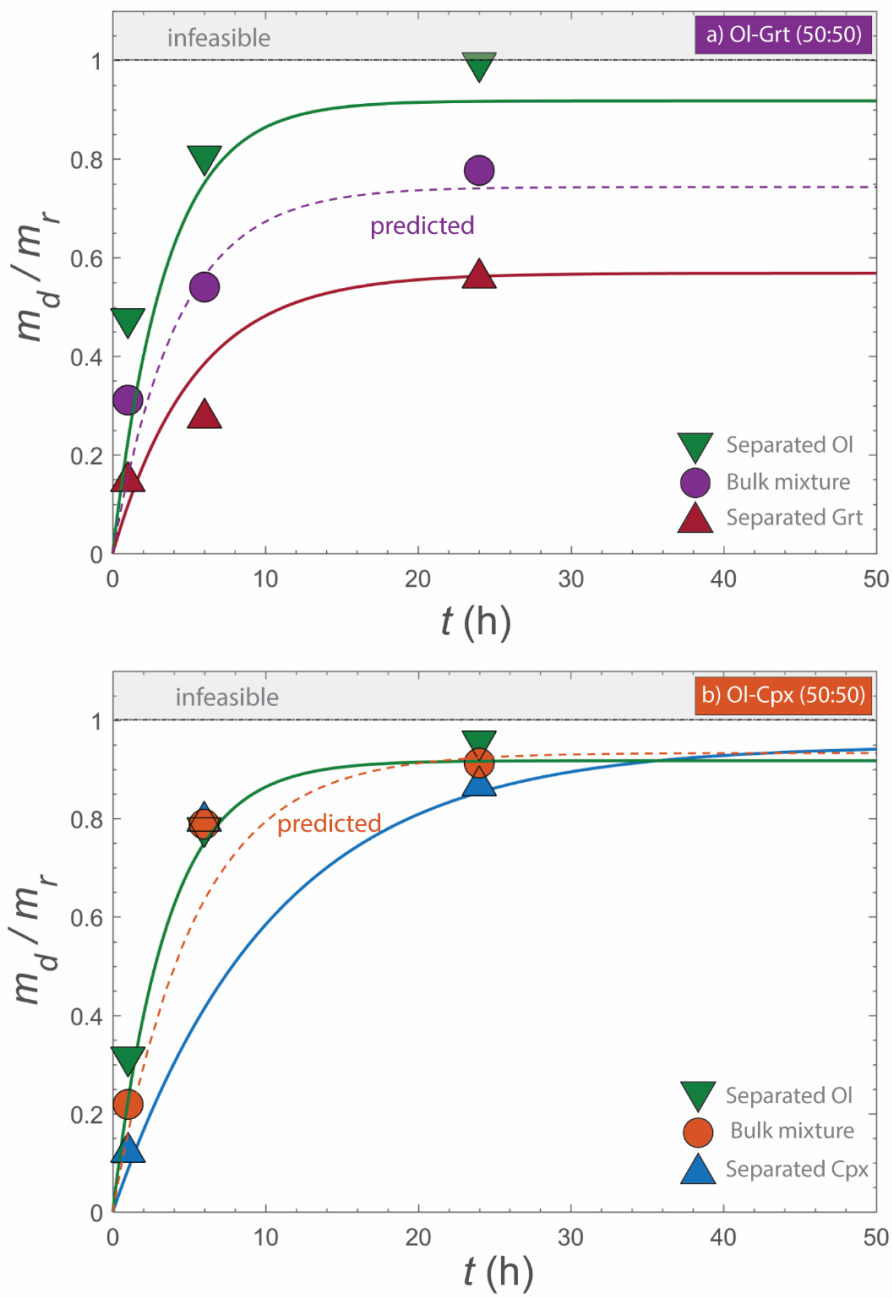

Figure 5-14. Ratio of daughter particles to the total (m_d / m_r) against time for a short (1 h) medium (6 h) and long (24 h) duration for a) Olivine-garnet and b) Olivine-clinopyroxene. Circles represent the m_d / m_r bulk mixture and triangles the m_d / m_r of the individual minerals obtained from separating the minerals from the bulk mixture. Solid lines are for the single mineral experiments taken from Figure 5-2 and dashed lines are an average of these two curves. The bulk mixture should plot along the predicted dashed line if the attrition rates and limits do not change for each mineral.

To determine the m_d / m_r of the minerals within the mixture, the mineral grains of the parent fraction (600 – 710 µm) were separated by hand, weighed and subtracted from the total recovered mass to finally arrive at the mass of the individual minerals.

The bulk mixture of olivine-garnet is observed to plot very close to the predicted average and the separated olivine and garnet plot close to their respective single mineral curves. Garnet underwent no change compared to the single mineral experiment. Olivine in comparison had no change in the attrition limit, however experienced a slightly enhanced rate of attrition at low (1 h) residence times. The bulk mixture matched the linear 50/50 average as hypothesized.

The bulk mixture of olivine-clinopyroxene plots along the predicted line at the earliest (1 h) and the latest (24 h) time, however at 6 h plots quite far above the 50/50 linear prediction. For clinopyroxene a drastic change is noticed at the 6 h mark where the rate more than doubles that of the individual mineral experiment. Neither of the attrition limits seem to have been affected for either mineral, however the attrition rate of clinopyroxene was considerably enhanced at intermediate residence times. The bulk mixture does not match the hypothesized linear 50/50 average.

Chapter 6: Discussion

6.1 Transport Duration and Velocity of Kimberlite Ascent

Kimberlite magmas are able to rapidly transit the cratonic mantle lithosphere from source depths in excess of 150 km (Russell et al., 2012; Sparks et al., 2006; Wilson and Head, 2007). At depth the dyke propagates towards the surface by dyke tip propagation whereby the overlying mantle is fractured and entrained into the dyke tip (Brett et al., 2015; Russell et al., 2017; Spera, 1984). Due to the silica undersaturated nature of the initial melt, orthopyroxene is preferentially assimilated (Mitchell, 1973), resulting in deep-seated CO_2 exsolution, generating buoyancy through density reduction and triggering the onset of rapid ascent (Russell et al., 2012; Wilson and Head, 2007). Rapid transport (10's of m s^{-1}) of kimberlite through the cratonic lithosphere has been discussed by many authors (Brett et al., 2015; Jones et al., 2019; Kavanagh and Sparks, 2009; McGetchin and Ullrich, 1973; Russell et al., 2012; Sparks, 2013; Sparks et al., 2006; Wilson and Head, 2007), however the dynamics still remain a hotly debated topic. Specifically, the timescales and velocities associated with magma ascent are poorly constrained with velocity with estimates ranging from 1-20 m s^{-1} (Sparks et al., 2006; Wilson and Head, 2007) resulting in transport timescales of hours-days. Ultimately, the fast moving, low viscosity, cargo laden nature of kimberlite magma provides an ideal environment for attrition of mantle cargo (Arndt et al., 2006, 2010; Brett et al., 2015; Jones et al., 2019, 2014; Jones and Russell, 2018).

The flow regime in my experiments fall in the same range as nature which allows me to relate the experiments to the natural system (Section 3.3). Flow regimes are quantified by using the Reynolds number (Re) which has a range in kimberlites, Re_k of ~ $1 \times 10^2 – 1 \times 10^6$ (see Section 3.3). This is calculated by:

$$\mathrm{Re_k} = \frac{\mathrm{D}v\rho}{\mu} \qquad [6.1]$$

where D [m] is the dyke diameter, v [m s^{-1}] is the velocity of the ascending magma, ρ [kg m^{-3}] is the bulk density and μ [Pa s] is the bulk viscosity of the three phase fluidized mixture (melt, crystal, volatiles). Using the ranges of estimates given in Section 3.3, reasonable values are assigned to each parameter. Specifically, a dyke diameter (D) of 1.5 m, a magma velocity (v) of 4 m s^{-1}, a bulk density (ρ) of 2100 kg m^{-3} and a bulk viscosity (μ) of 0.05 Pa s which relates to $\mathrm{Re_k} = 2.52 \times 10^5$.

Similarly, the Reynolds number of the experiments ($\mathrm{Re_{exp}}$) is given by:

$$\mathrm{Re_{exp}} = \frac{\mathrm{L}v^*\rho^*}{\mu^*} \qquad [6.2]$$

Where L is the attrition tube internal diameter [m], v^* [m s^{-1}] is the bulk velocity [m s^{-1}], ρ^* is the bulk density [kg m^{-3}] and μ^* [Pa s] is the bulk viscosity. Here I have chosen to adopt a mixture-based approach (Weit et al., 2019, 2018) for calculation of velocity, density and viscosity of the fluidized mixture of gas and particles. The velocity (v^*) is given by:

$$v^* = \varphi v_\mathrm{p} + (1 - \varphi) v_\mathrm{g} \qquad [6.3]$$

Where φ is the particle concentration, v_p [m s^{-1}] is the particle velocity and v_g [m s^{-1}] is the superficial gas velocity. Particle concentration (φ) is calculated using:

$$\varphi = \frac{h_{0\ calc}}{h_p} \qquad [6.4]$$

Where $h_{0\ calc}$ [mm] is the initial bed height and h_p is the column height of the fluidized bed (Section 3.4). The bulk density (solid + gas) of the mixture (ρ^*) is given by:

$$\rho^* = \varphi \rho_\mathrm{p} + (1 - \varphi) \rho_\mathrm{g} \qquad [6.5]$$

Where ρ_p [kg m^{-3}] is the particle density and ρ_g [kg m^{-3}] is the gas density. Finally, the bulk (as above, sold + gas) viscosity (μ^*) is given by:

$$\mu^* = \mu_g(1 + \frac{5}{2}\varphi) \qquad [6.6]$$

where μ_g [Pa s] is the gas viscosity. Since the parameters (i.e. φ, ρ_p, v_p) of the mixture metrics vary for each mineral series, the Re_{exp} will vary slightly. The Re_{exp} calculated for olivine, orthopyroxene, clinopyroxene, garnet and diamond were 2.46×10^5, 2.37×10^5, 2.47×10^5, 2.98×10^5 and 2.72×10^5 respectively. Now I equate Re_k and Re_{exp} for each mineral series to find the velocity of the kimberlite magma (v) by:

$$v = \frac{Re_{exp}\mu}{\rho D} \qquad [6.7]$$

Using this approach, velocities calculated for olivine, orthopyroxene, clinopyroxene, garnet and diamond were 3.91, 3.77, 3.91, 4.73 and 4.31 m s^{-1}, respectively.

To relate the model attrition rates (Figure 5-2a) to kimberlite ascent, the x-axis is converted from time [h] to distance [km] by multiplying by the velocities calculated above (Figure 6-1a). The resulting curves now show attrition as a function of distance when the kimberlite magma is in a fluidized, turbulent state. This Figure can now be used to inform on mantle cargo mass loss during dyke ascent and as a proxy for xenocryst source depth. For example, mantle material sourced at 100 km will likely not be as well rounded as material sourced from 150 – 200 km depth. Additionally, each of the mantle minerals can be assessed individually in kimberlite deposits and used collectively to suggest ascent rates and source depths. However, other factors contributing to mass loss or mass addition should also be considered before applying this concept. For example, dissolution of the mineral will contribute to mass loss and crystallization around the mineral rim will contribute to mass gain.

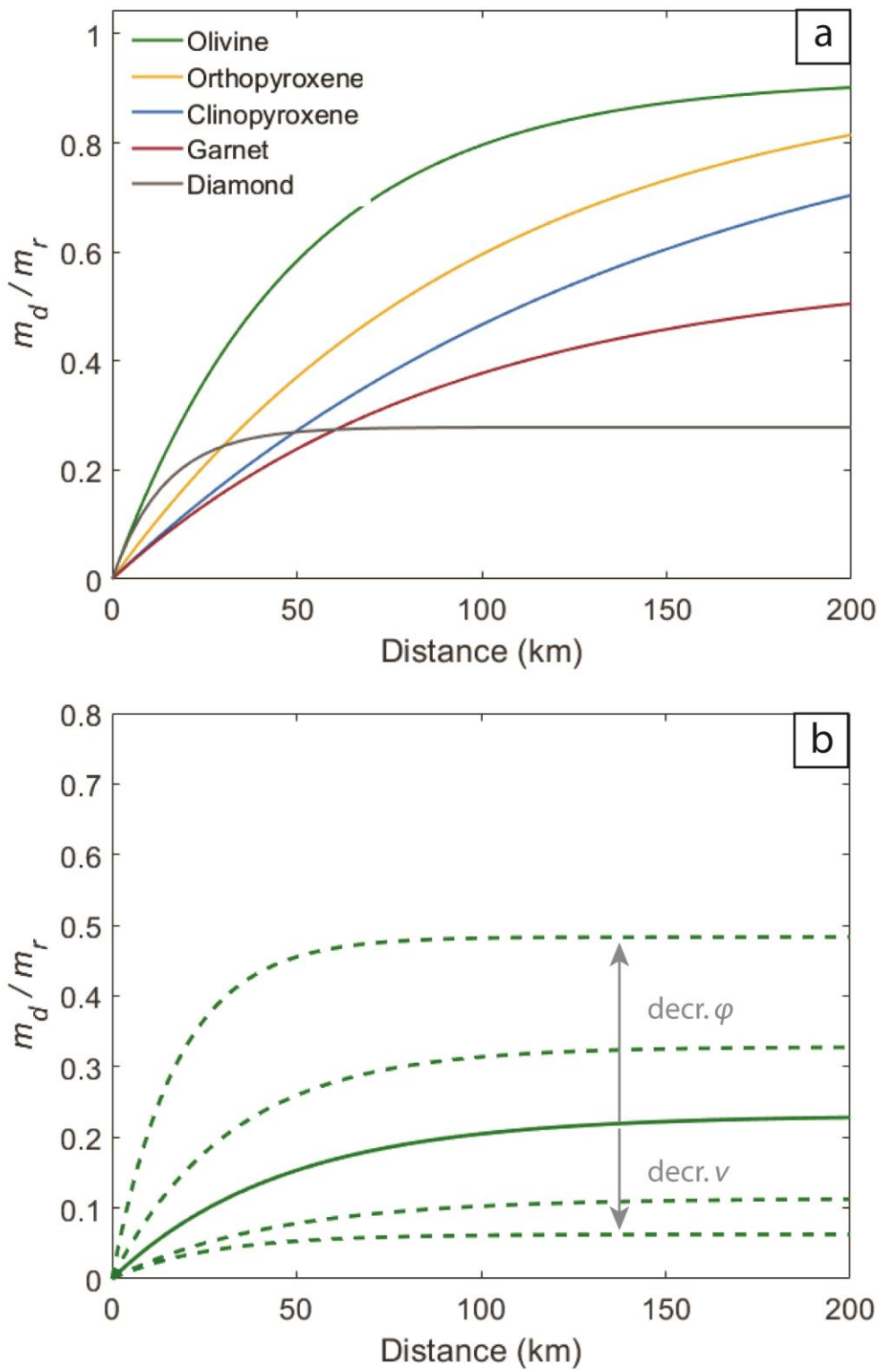

Figure 6-1. a) Mineral series attrition curves where the x-axis is converted to distance using calculated ascent velocities. b) Olivine curves from Jones et al. (2019) showing the effects of changing input mass and gas flux.

These attrition curves are also dependent on the gas flux and mass input used in the experiments (Jones et al., 2019). This is illustrated in Figure 6-1b where the attrition curves presented in Jones et al. 2019 are scaled in the same way as presented above to convert the time axis to distance. Although it is impossible to know the true particle concentrations in the dyke, the *a* and *b* parameters are sensitive to the amount energy in the system and the particle concentration. This means that in application of these models to the ascending kimberlite dyke, the choice of particle concentrations and energy (velocity) needs to be chosen with caution. It is recommended a range of possible energy levels and particle concentrations are considered.

6.2 Morphology and Surface Features of Coherent Kimberlite Xenocrysts

Olivine, clinopyroxene and garnet grains were carefully extracted from coherent Diavik A154N drill core to study the morphology and surface features of xenocrysts. The Diavik pipes are late Cretaceous and Eocene in age and are located in the Northwest Territories, Canada, part of an economic ore body within the Lac de Gras kimberlite field (Heaman et al., 2004). The xenocrysts imaged in this study were extracted firstly by using a diamond drill tip to extract an area of groundmass encasing the grain. Then, the grain was rinsed under water to remove the attached groundmass. The grains were imaged using scanning electron microscopy at various magnifications.

The images of the kimberlitic xenocyrsts reveal a remarkable resemblance to the experiment products (Figure 6-2). Specifically, the kimberlitic xenocrysts display rounded morphologies and rough surfaces dominated by impact pits. These features have been interpreted to result from abrasion during ascent of kimberlite magma. In the engineering sciences, impact features have been linked to collisional energetics and are used to inform on impact velocities (Bayham et al.,

2016; Fulchini et al., 2019; Ghadiri and Zhang, 2002; Novák-Szabó et al., 2018; Scala et al., 2013). Diavik olivine and garnet show discernable hemispherical impact pits with measurable dimensions.

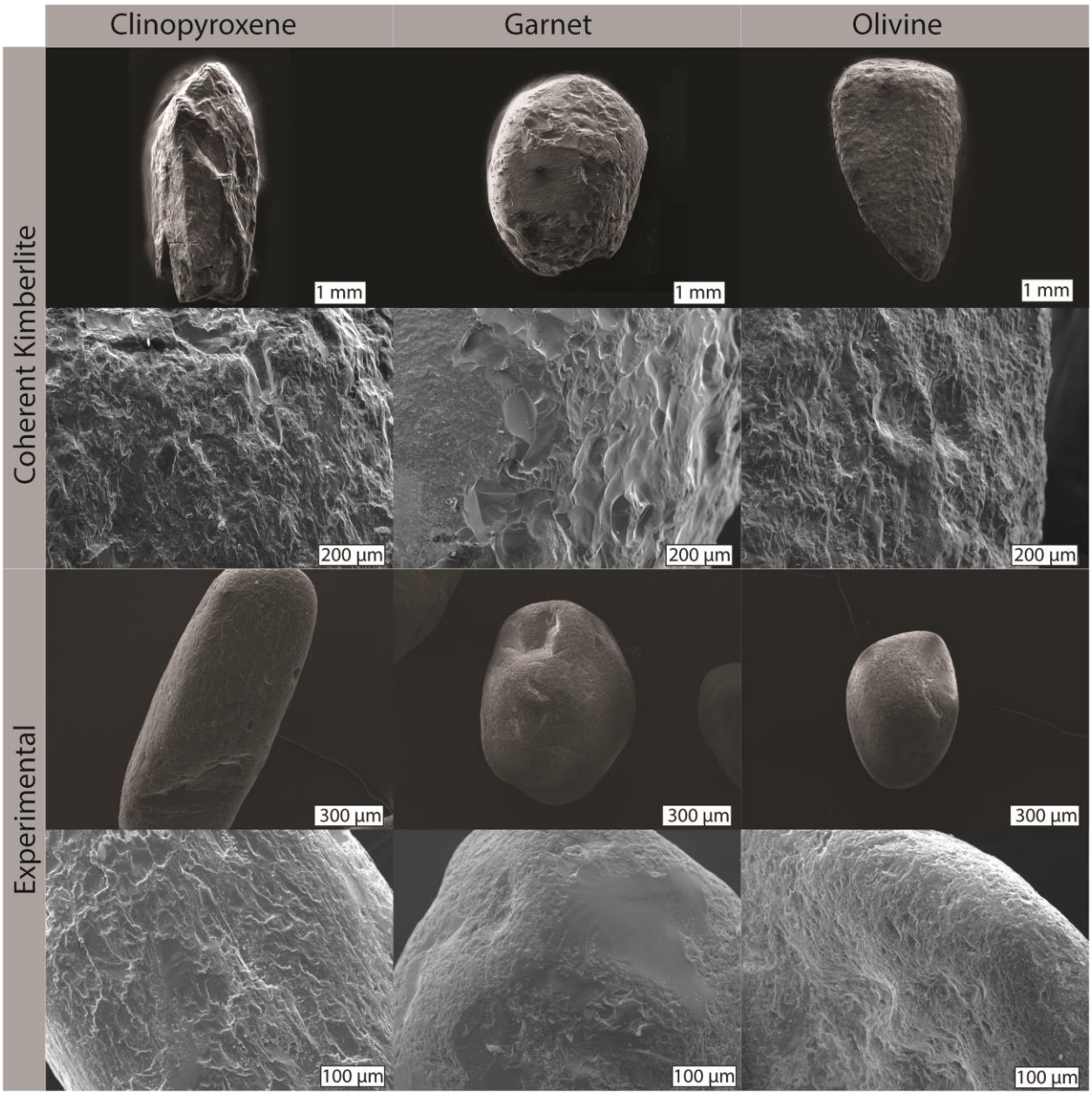

Figure 6-2. Morphology and surface features of clinopyroxene, garnet and olivine grains extracted from Diavik coherent kimberlite compared with experiment products.

As described in 5.1.4, the impact features of clinopyroxene show more flaking rather than hemispherical pits. This texture forms when the impact zone penetrates through cleavage planes, resulting in brittle breakage and flaking. For this reason, impact pits on clinopyroxene are difficult to discern and not further analyzed. Due to the complex and dynamic environment present in the ascending dyke, impact pits often appear to overprint former roughness features.

In natural kimberlite, rough surfaces and cavities are also observed which are not consistent with that of attrition. The creation of surface textures in kimberlite can broadly be divided into ‘chemical’ and ‘mechanical’ processes (Jones et al., 2019, 2014). Chemical textures originate from assimilation and crystallization (Giuliani, 2018; Kamenetsky et al., 2008; Pilbeam et al., 2013) whereas mechanical textures originate from particle-particle collisions (Arndt et al., 2006, 2010; Brett et al., 2015; Jones et al., 2019, 2014; Russell et al., 2012). The appearance of these contrasting modes of surface modification are illustrated in Figure 6-3. Importantly, the features observed on the xenocrysts are pervasively mechanical in nature. Cavities formed by chemical etching appear strongly controlled by crystallography, having sharp edges and regular geometry (Figure 6-3). Impact pits by contrast have convex outlines and hemispherical morphologies (Figure 6-2; 6-3). Roughness is also observed on clinopyroxene and garnet (Figure 6-3) which is more likely to have formed under chemical controls. Clinopyroxene often shows globular formations <10 μm in size on the surfaces of exposed cleavage planes and garnet is observed to have a fibrous kelyphite reaction rim (Figure 6-3). Mechanically and chemically derived features have controls and formation conditions which are largely independent of another, acting during different stages of ascent (Arndt et al., 2010; Brett et al., 2015; Jones et al., 2019). Since the surface features observed on xenocrysts from Diavik (Figure 6-2) are dominantly mechanical in nature, at a minimum, mechanical processes dominate during the final stages of ascent.

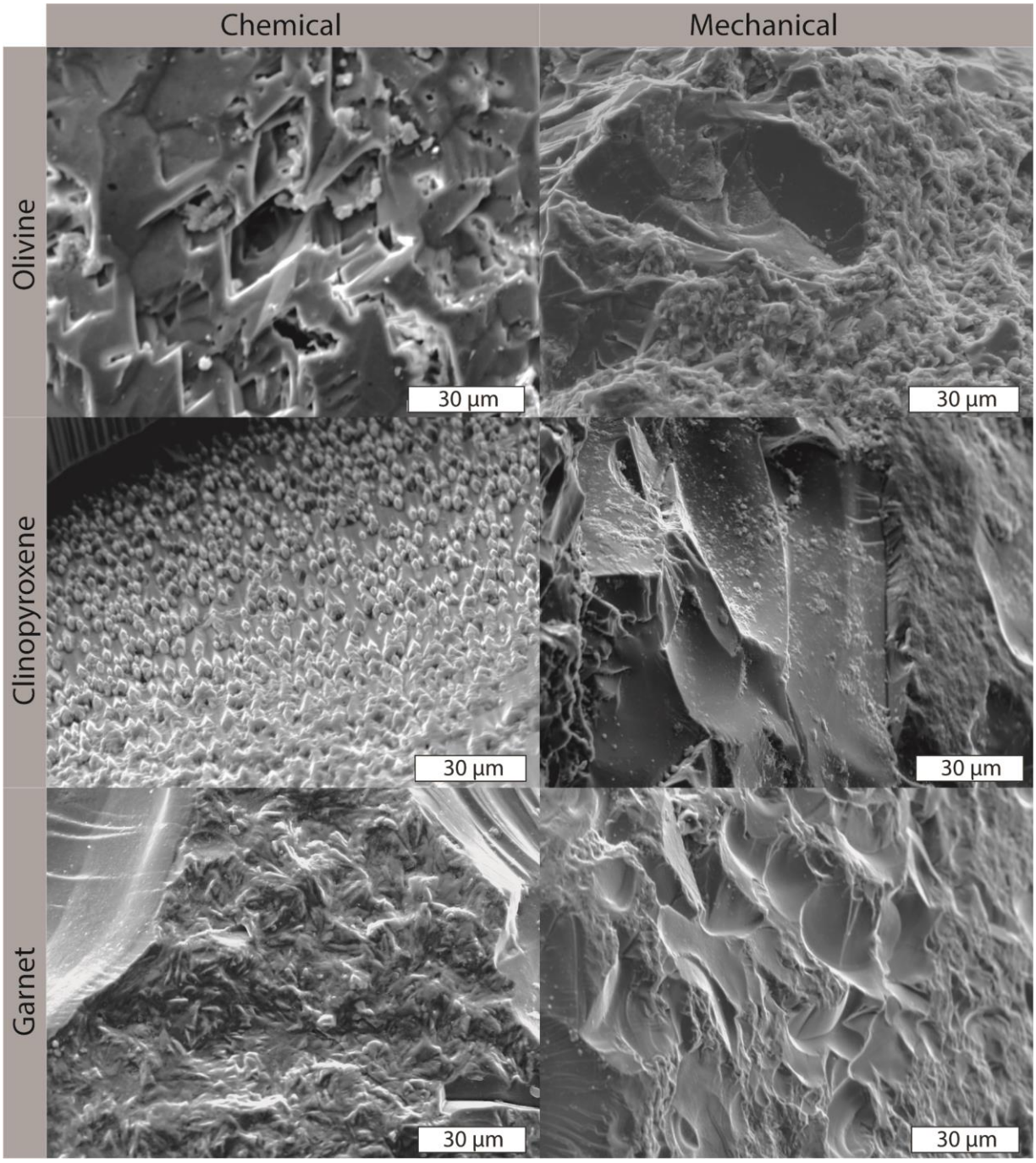

Figure 6-3. Comparison of chemical and mechanical surface features on natural Diavik xenocrysts of olivine, clinopyroxene and garnet. Olivine: Left: Dissolution feature showing straight edges. Right: Hemispherical impact pit overprinting a rough surface. Clinopyroxene: Left: Globular formations on exposed cleavage planes. Right: Cleavage controlled breakage. Garnet: Left: Layer of fibrous kelyphite rim on garnet. Right: Conchoidal fractures from repeated impacts.

Diamonds from the experiments also revealed surface features which are unlikely a product of attrition (Figure 6-4).

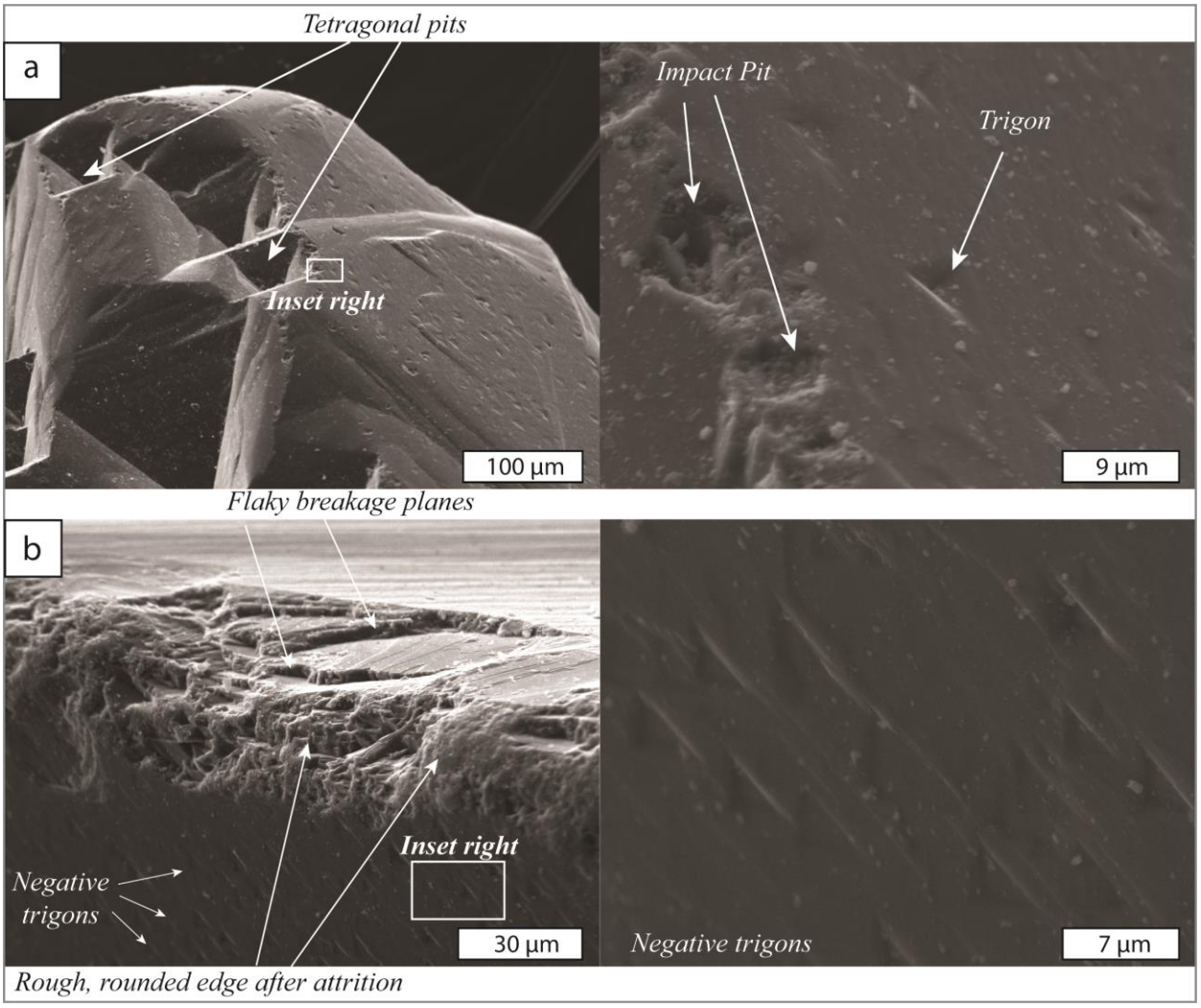

Figure 6-4. a) Left: Diamond showing equant tetragonal pits. Right: Inset highlighting difference between impact pit and trigon. b) Left: Rough edge of an attrited diamond with one surface showing cleavage-controlled breakage and another surface with trigons. Right: Inset of trigons.

For instance, some diamonds showed deep tetragonal pits (Fedortchouk, 2019; Win et al., 2001) with straight edges and uniform, near perfect geometry. Smaller scale trigons (Fedortchouk, 2019) are also noted on surfaces (Figure 6-4a,b) with consistent size, depth and a regular triangle

shape. Importantly, the tetragonal pits and trigons observed on some of the diamond experiment products are pre-existent and did not form during the attrition experiments. Proximal to the trigons, impact pits are observed (Figure 6-4a), which are often hemispherical and have a range of diameters, depths and morphologies. As with the other minerals discussed, the conditions controlling formation of mechanical and chemical modification vary for diamond. Specifically, The depth and size of the impact pits are attributed to the mineral size, physical properties and the collision energy (Ghadiri and Zhang, 2002; Salman et al., 2002; Zhang and Ghadiri, 2002) whereas the depth, size and geometry of etch features in diamond reflects the crystallography and nature of the conditions (temperature, pressure, H_2O:CO_2, composition, etc.) in the reacting solvent (Fedortchouk, 2019; Khokhryakakov and Pal'Yanov, 2010; Zhang et al., 2015).

6.3 Mineral Physical Properties Related to Attrition Susceptibility and Mechanisms

In a fluidized system the infinite attrition limit, *a*, depends on the physical properties of the solid particles and the energy that the particles have (environmental factor). The attrition rate constant, *b* depends on both the probability for a collision to occur and the likelihood that collisions are at, or above, the threshold velocity for breakage. This is further controlled by the mineral's initial shape. For example, highly irregular grains that have more asperities are more susceptible to chipping and mass loss (Bemrose and Bridgwater, 1987; Fulchini et al., 2019; Jones et al., 2019).

Previous studies have shown that mineral properties influence the attrition susceptibility of particulate solids (Bemrose and Bridgwater, 1987; Boerefijn et al., 2007; Bridgwater, 2007; Frye, 2007; Ghadiri and Zhang, 2002; Scala et al., 2013).

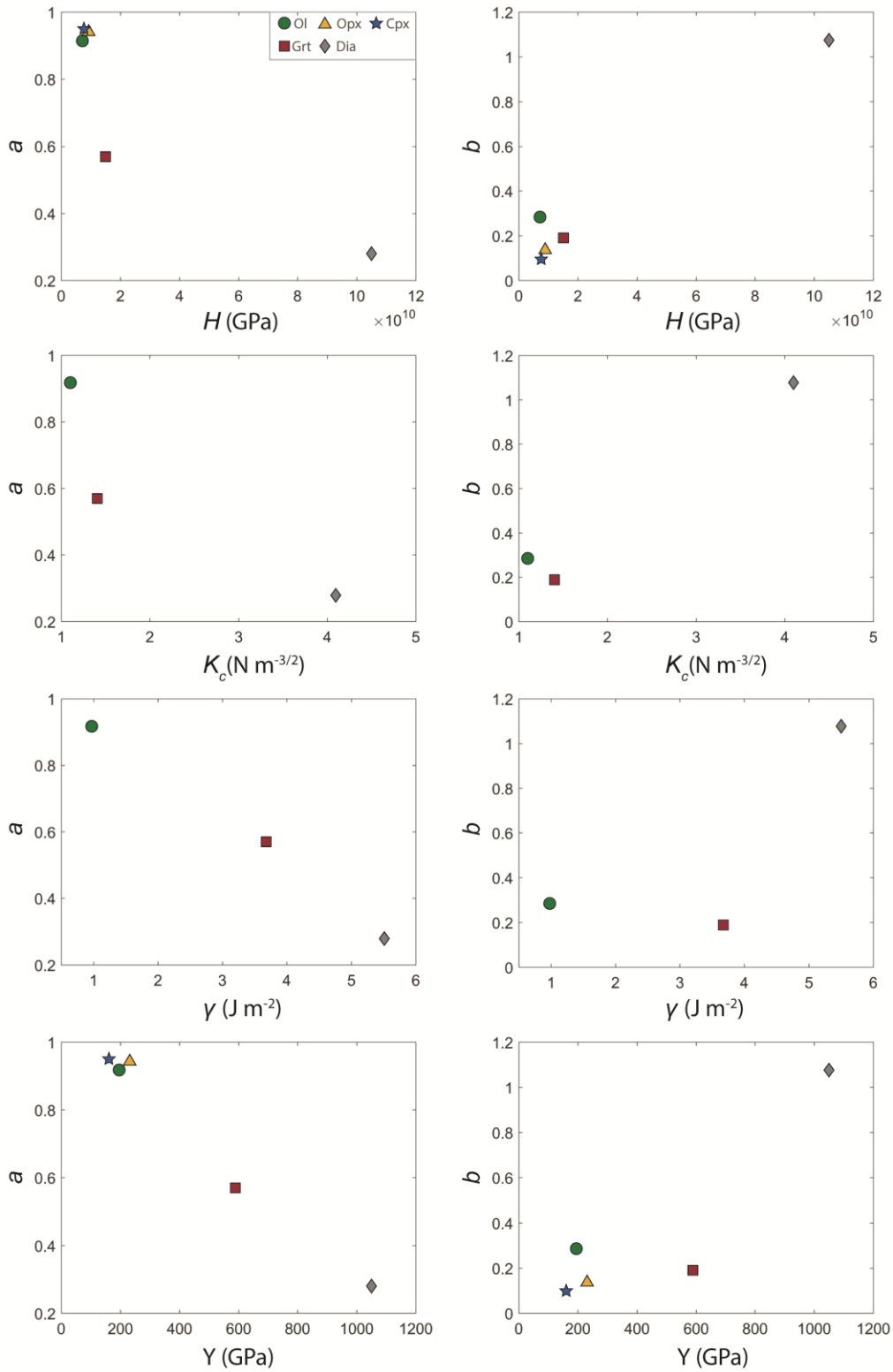

Figure 6-5. Model *a* and *b* values plotted against mineral physical properties where *H* is hardness, K_c is fracture toughness, *γ* is the fracture surface energy and Y is the Young's modulus.

The mineral properties chosen for analysis in this study reflect the ability to sustain impact stress and are consistent with those used for analysis in other studies (Bayham et al., 2016; Bridgwater, 2007; Frye, 2007). These properties include: Hardness (*H*), a measure of the resistance to localized plastic deformation induced by mechanical indentation, fracture surface energy (γ) a measure of the energy required to create a new surface, fracture toughness (K_c), a measure of material resistance to crack propagation when a flaw is present and Young's modulus (Y) which is a measure of stiffness during elastic deformation. To relate the attrition rates and limits of the minerals studied to their physical properties, the *a* and *b* model parameters of each mineral have been plotted against the physical properties (listed in Table 4-2) discussed above (Figure 6-5).

Figure 6-5 reveals a negative correlation between *a*, the attrition limit and all physical properties. In comparison, no apparent correlation between *b* and the physical properties is observed. As previously mentioned, the attrition rate is more dependent upon particle concentrations (i.e. frequency of collisions) and initial particle morphology. Due to the complex nature of attrition, engineering studies correlating attrition rates with material properties have been met with limited success due to a poor understanding of the role that particle concentration and morphology plays (Bayham et al., 2016; Frye, 2007). Once again, it is important to note that the *a* and *b* values are dependent on the energy conditions in the system (Jones et al., 2019) and therefore only valid for the conditions present in this study.

6.4 Attrition Mechanics

Subpopulation modes in particle size distributions are created either by fragmentation or abrasion (Bayham et al., 2016; Jones et al., 2019; Jones and Russell, 2017; Scala et al., 2013;

Xiao et al., 2014). Fragmentation is a high energy process resulting in wholesale breakage of the parent particles (Chen et al., 2007; Sadrai et al., 2006). Abrasion is a lower energy process causing rounding of particles and the generation of chips and fines (Cagnoli and Manga, 2003; Dufek and Manga, 2008; Freundt and Schmincke, 1992; Jones and Russell, 2017; Kueppers et al., 2012; Manga et al., 2011; Mueller et al., 2015).

Ultimately, the attrition process characterized by the breakage of particulate solids is the mechanism in which particles respond to collisional stress. The mechanisms operating for fragmentation and abrasion are notably different which will now be explored in the following sections that deal with abrasion and fragmentation respectively.

6.4.1 Abrasion Mechanics

Abrasion is a localized stress release mechanism and can be further divided into surface wear and chipping (Bayham et al., 2016; Boerefijn et al., 2007; Fulchini et al., 2019; Ghadiri and Zhang, 2002). Surface wear takes place at the micron scale and is associated with plastic deformation and shear stress at the surface of the grain (Hutchings, 1993; Scala, 2013), releasing ultrafine particles. In the case of chipping, brittle failure takes place whereby a fracture propagates from the site of impact, extending laterally and curving to towards the surface (Fulchini et al., 2019; Ghadiri and Zhang, 2002; Scala et al., 2013). This results in release of chips, often larger in size than that produced by surface wear. The relative extent of each process is revealed in the grain sizes below <100 µm (Figure 5-3) and through SEM imagery (Figure 5-11). Specifically, the abrasion products typically show a bimodal distribution in which the mode at the larger grain size is produced by chipping exclusively and mode at the smaller grain size can be produced by both chipping and surface wear, although likely dominated by the latter.

Abrasive wear of materials is associated with plastic deformation and therefore has typically been linked to hardness (Archard, 1953; Eyre, 1976; Hutchings, 1992). The model proposed by Archard (1953) relates the extent of breakage by wear (ζ_{wear}) to the normal compressive force acting on the particle (F [mN]), the sliding distance (Δs [m]) and the material hardness (H [Pa]):

$$\zeta_{wear} = \alpha_w \frac{\mathrm{F}\Delta\mathrm{s}}{H} \qquad [6.8]$$

Where α_w [m^{-3}] is a material dependent proportionality factor. The implication is that harder minerals such as diamond are less prone to abrasion in comparison to a less hard mineral such as olivine.

The extent of breakage by chipping (ζ_{chip}) has been described by Zhang and Ghadiri (2002):

$$\zeta_{chip} = \alpha_c \frac{H}{{K_c}^2} \rho_\mathrm{p} {v_\mathrm{p}}^2 d_p \qquad [6.9]$$

Where K_c [Pa m$^{-0.5}$] is the fracture toughness, ρ_p [kg m^{-3}] is the particle density, v_p [m s^{-1}] the impact velocity and d_p [µm] is the particle diameter. α_c [kg m$^{-0.5}$ s^2] is a material dependent proportionality factor. The relationship is strongly dependent on the brittleness factor (Ghadiri and Zhang, 2002), a ratio of the hardness to the fracture toughness ($H\,K_c^{-2}$) and implies that materials with a higher fracture toughness are more prone to chipping.

Importantly the above two relationships might explain the relative peak sizes of the abrasion products (<100 µm). For instance, olivine has a relatively low hardness and low brittleness index ($H\,K_c^{-2}$) indicating higher susceptibility to surface wear. Diamond has both a high hardness and a high brittleness index suggesting it is more likely to undergo chipping. The consequences of this are evident in the bimodal daughter products of <100 µm. Surface wear is

limited to the smallest mode (< 20 µm) and chipping contributes to both the larger mode (80 – 100 µm) and the smallest mode.

Breakage in natural materials through chipping is typically semi-brittle (Ghadiri and Zhang, 2002) and zones of plastic deformation in the form of impact pits are usually noted on attrited surfaces (Figure 6-6). In the engineering sciences, the impact pit geometry has been related to the material properties and impact velocity (Ghadiri and Zhang, 2002; Zhang and Ghadiri, 2002):

$$i = klv_{\mathrm{p}}^{\frac{1}{2}}\left(\frac{\rho_{\mathrm{p}}}{H}\right)^{1/4} \qquad [6.10]$$

Where i [m] is the impact pit diameter, k is a proportionality constant and l [m] is the particle diameter. The equation assumes hemispherical impact geometry and an equant particle morphology. k is not readily available for the minerals investigated in this study and was instead constrained using my experiment data for olivine and garnet. This was done by rearranging Equation 6.10 to solve for k using average differential velocities presented in Section 5.1.3 and mineral properties presented in Table 4-3. Specifically, both minerals have the same input size (l) of 0.000655 m and average differential velocities (v_{p}) of 1 m s^{-1}. Density and hardness values for olivine and garnet are 3246 kg m^{-3} and 3890 kg m^{-3} and 7.1 x 10^{9} Pa and 1.5 x 10^{10} Pa, respectively. Impact pit measurements of the experiment products of olivine and garnet parent grains were taken to arrive at average pit diameters of 10.8 ± 3.16 µm and 6.92 ± 1.87 µm, respectively. This was calculated from 52 measurements of each mineral across the surfaces of three grains from random experiment durations. Using these inputs, k values of 0.63 and 0.47 were calculated for olivine and garnet respectively.

Now with the proportionality constant, k, obtained for olivine and garnet, Equation 6.10 can now be rearranged to solve for impact velocity after measuring impact pit diameter:

$$v_{\mathrm{p}} = \left(\frac{i}{kl\left(\frac{\rho_{\mathrm{p}}}{H}\right)^{1/4}} \right)^{2} \qquad [6.11]$$

Using this approach, two carefully extracted olivine grains and two garnet grains from Diavik A154N coherent kimberlite had impact pits measured. The impact pits measured were often overprinting smaller scale textures and had relatively fresh interiors, indicating that they likely derive from collisions during the later stages of ascent (Figure 6-6).

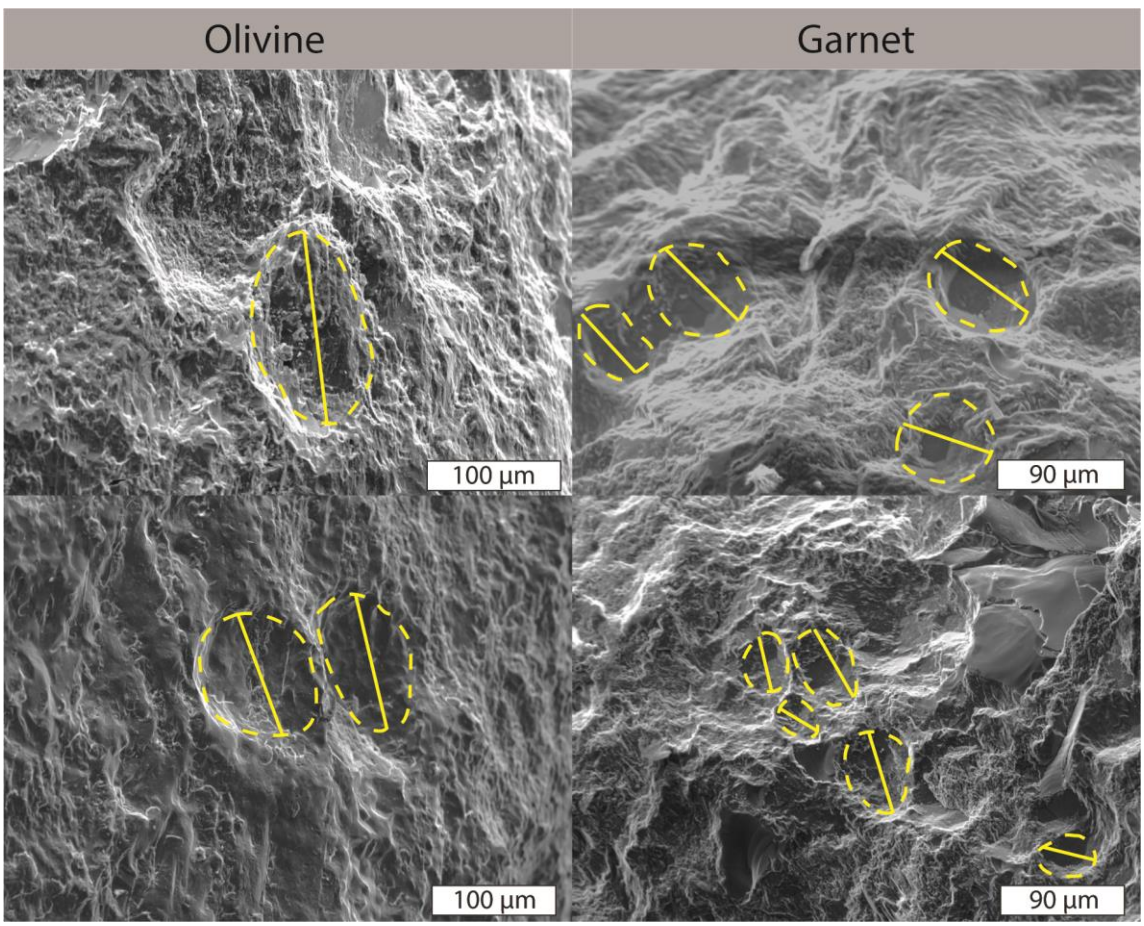

Figure 6-6. Impact pit example are outlined in yellow dashed lines for olivine and garnet on the surface of Diavik xenocrysts. Solid yellow lines show the measurement taken for the impact pit diameter.

For olivine and garnet, a total of 16 and 13 impact pit measurements were made, respectively, across two grains of each mineral. The range of impact pit diameters of the two olivine grains were 101 – 172 µm and for the two garnet grains were 78 – 119 µm. The average computed impact velocity for each olivine grain was 3.38 ± 0.87 and 4.48 ± 0.95 m s^{-1} with a total velocity range of 2.36 – 5.39 m s^{-1}. The average impact velocities for garnet were found to be 3.51 ± 0.54 and 4.81 ± 0.88 m s^{-1} with a range of 2.87 – 6.05 m s^{-1}. The relationship between pit size and impact velocity is visualized in Figure 6-7 for olivine (Figure 6-7a) and garnet (Figure 6-7b). Interestingly, the olivine and garnet from Diavik coherent kimberlite show remarkable agreement in impact velocities of ~ 4 m s^{-1}. The overlapping ranges approximate collisional velocities in the kimberlite magma and can be linked to dyke ascent. The implication is that the kimberlite dyke was traveling at ~ 4 m s^{-1} during late stage ascent. However, this is likely an underestimate since implicit in this statement is the assumption that the fluidized particles are perfectly coupled with the magma.

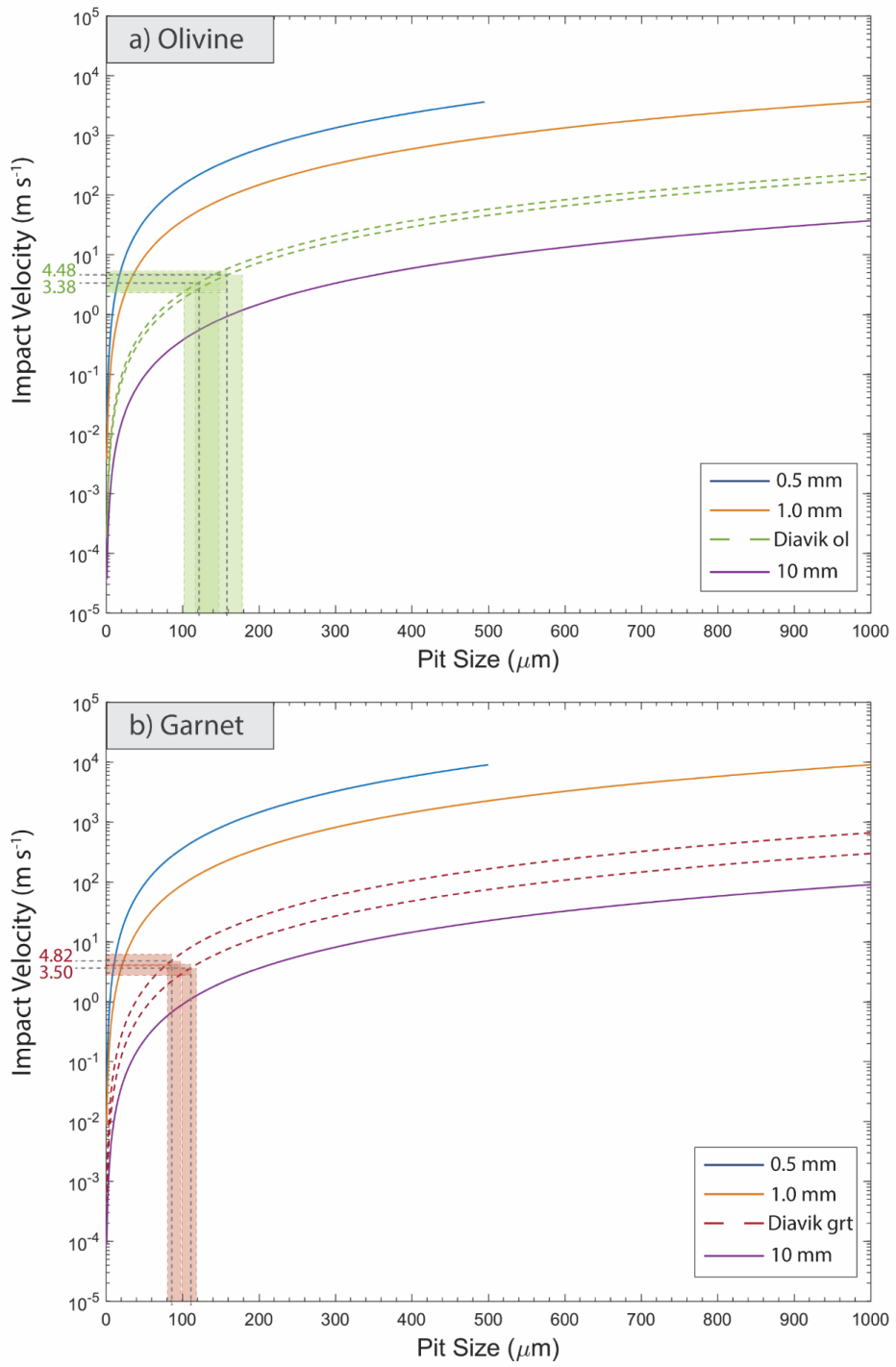

Figure 6-7. Lines showing relationship between impact velocity and pit size for different size grains of a) olivine and b) garnet. Pit sizes were measured for two grains of olivine and two grains of garnet from Diavik (dashed curves show sizes of grains). The average velocities were computed from the average pit diameters (vertical and horizontal dashed lines). The shaded regions denote total range.

6.4.2 Fragmentation Mechanics

During fragmentation cracks develop and radially propagate through the volume of the particle, leading to catastrophic failure and wholesale breakage (Ghadiri and Zhang, 2002; Scala, 2013). Fragmentation susceptibility is largely dependent on energy of a collision and has a threshold that can be determined using the method of Ball and Payne (1976) and adopted by Jones et al. (2019). The stress required (σ_f) to propagate a crack through the diameter of the grain is given by Ball and Payne (1976):

$$\sigma_f = \sqrt{\frac{2\mathrm{Y}\gamma}{\pi l}} \qquad [6.12]$$

Where Y is the Young's modulus [Pa], γ is the fracture surface energy [J m^{-2}] and l is the crack length [m] (take diameter of particle for fragmentation). During a high energy collision, fragmentation occurs when the stress as a result of impact (σ_{im}) exceeds the stress required for crack propagation: $\sigma_{im} > \sigma_f$. The impact stress resulting from impact for an equant particle of length l can be approximated by:

$$\sigma_{im} = v_{\mathrm{p}}\sqrt{\rho_{\mathrm{p}}\mathrm{Y}} \qquad [6.13]$$

Where v_{p} is the impact velocity [m s^{-1}] and ρ_{p} is the particle density [kg m^{-3}]. By equating Equation 6.12 and Equation 6.13 and using parameter values for each mineral listed in Table 4-2, the velocity required for fragmentation was solved for. Olivine, garnet and diamond were found to have fragmentation threshold velocities of 0.54, 0.96 and 1.2 m s^{-1} respectively. Since a measure of the fracture surface energy of diopside and enstatite were not available, they were not calculated. The average differential velocities (i.e. impact velocity) used for each mineral was 1.0 m s^{-1} (Table 5-4). This would imply that olivine and garnet should have sufficient energy to

undergo fragmentation whereas fragmentation of diamond should be rare or unlikely. This is in excellent agreement with my grain size distributions (Figure 5-3) which showed an intermediate daughter mode for both olivine and garnet but not for diamond. The threshold velocity calculations further reinforce the interpretations made in Figure 5-12 that the intermediate sized daughter grains resulted from collisions with sufficient energy to induce fragmentation of parent particles. Although data is missing to calculate the fragmentation thresholds for orthopyroxene and clinopyroxene, the weak physical properties relative to the other minerals imply that the intermediate peaks observed in the pyroxene grain size distributions are a result of fragmentation.

6.5 Implications of Multiphase Mineral Mixtures in Nature

Natural geological systems rarely involve a single type of particulate solid but rather comprise particulate mineral mixtures. This includes river streams, kimberlite mineral indicator trains (Afanas'ev et al., 2008; Cummings et al., 2014, 2011; Jones and Russell, 2018), and volcanic environments such as pyroclastic flows (Freundt and Schmincke, 1992; Jones and Russell, 2018; Kueppers et al., 2012; Manga et al., 2011), conduits (Campbell et al., 2013; Jones and Russell, 2017) and kimberlite diatremes (Gernon et al., 2009b; Smith and Griffin, 2005). Importantly, kimberlite magmas are also host to multiphase mineral mixtures (Brett et al., 2015; Jones et al., 2019; Scott Smith, 2008) with modal proportions of each mineral governed by the mantle xenolith compositions that are disaggregated. The implications of this are numerous.

The varying attrition rates of each mineral means that modal abundances will change as minerals undergo different degrees of fragmentation and abrasion. The modal abundances observed in coherent kimberlite are therefore not representative of that in the mantle and biased

to attrition resistant minerals. Since diamond is the most resistant to attrition, the proportion of parent diamond grains also increases relative to other minerals during the ascent process. The fine daughter products created by attrition are assimilated by the magma and as the magma fragments during eruption, mineral grains are liberated and deposited by hydrodynamic sorting (Harvey et al., 2013; Moss and Russell, 2011; Scott Smith, 2008). This style of pyroclastic infill is common in many Canadian kimberlites including Fort a la Corne, Lac de Gras and Viktor (Scott Smith, 2008). The implication is that this deposit will have an enhanced diamond grade as a result of attrition during ascent when compared to the case if no attrition were to take place.

Diamonds are however not indestructible and still susceptible to fragmentation during the ascent process. A 1 mm diamond has a fragmentation threshold velocity of 1 m s^{-1} and a 10 mm diamond has a fragmentation threshold of 0.3 m s^{-1} (calculated as in Section 6.4.2). Although fragmentation does not lower the diamond grade, it lowers the economic value since diamonds of smaller sizes are less valuable (Chapman and Boxer, 2004; Gurney et al., 2010).

Furthermore, the interaction of minerals with heterogenous physical properties can have profound consequences. It was shown that the presence of cleavage in mineral mixtures may have a strong influence over breakage. The result of olivine interacting with clinopyroxene was that although the attrition rate of olivine remained unchanged relative to its individual case, clinopyroxene's attrition rate was greatly enhanced. When olivine interacted with garnet, both olivine and garnet showed little change in comparison to the olivine-clinopyroxene experiments. These results are surprising because the bulk mechanical properties of olivine and clinopyroxene are very similar (Figure 6-5; Table 4-2) whereas garnet has a superior physical resistance to that of olivine. Presence of cleavage therefore has a very strong control over breakage. This has implications for the onset of turbulent ascent in kimberlites. Specifically, the preferential

assimilation of orthopyroxene by the initially silica-undersaturated melt triggers CO_2 fluid exsolution, increasing buoyancy and thereby supporting rapid ascent (Brett et al., 2015; Russell et al., 2012; Wilson and Head, 2007). Due to physical similarities of clinopyroxene and orthopyroxene, it can be assumed that the behavior of orthopyroxene when interacting with olivine will be the same as clinopyroxene. The consequence of an enhanced attrition rate (*b* value) of orthopyroxene is that assimilation is more efficient due to the newly created surface area by fragmentation and abrasion. This in turn creates a positive feedback cycle in which CO_2 exsolution increases magma ascent velocity, leading to more breakage and assimilation, continually supporting turbulent ascent.

Chapter 7: Conclusion

The particle-laden, high energy flow associated with kimberlite ascent undoubtedly provides the ideal environment for attrition. Given the lack of recent kimberlite eruptions and poorly constrained rheology and parental melt compositions, our understanding of ascent dynamics is limited. Experimental investigation of ascent processes and forensic evidence provided by kimberlite deposits serve as excellent tools to gain insight into the ascent environment.

In this study the mechanical modification of select mantle minerals was explored using analogue attrition experiments. Minerals were fluidized at consistent conditions (starting mass and gas velocity) for controlled durations. Conditions were chosen such that the Reynolds number fell within the range approximated for kimberlite dyke ascent. The attrition model of Jones et al. (2017) was fitted to the data to get the attrition limit (*a*) and the attrition rate (*b*) for each mineral series. I used grain size distributions, high speed videography, shape analysis and SEM imagery to document the effects of attrition on each mineral. Lastly, the implication of cleavage in mineral mixtures was investigated using binary mixtures of olivine-garnet and olivine-clinopyroxene.

Using data collected from the experiments, I conducted a scaling analysis to relate each set of mineral experiments to kimberlite dyke ascent using the Reynolds number to arrive at ascent velocities of ~ 3.8 – 4.7 m s^{-1}. To analyze textural modification during ascent, xenocyrsts were extracted from coherent kimberlite and imaged. Analysis of xenocrysts revealed textures pervasively mechanical in nature and remarkably like products of the attrition experiments. Impact pits on xenocrysts in kimberlite were linked to impact velocity for the first time using a

model adopted from the engineering sciences. I found that impact pits on natural garnet and olivine xenocrysts reveal a range of impact velocities of 2 – 6 m s^{-1} and an average of ~ 4 m s^{-1}.

By looking at experiment data and natural kimberlite xenocrysts, it is evident that the minerals respond differently to attrition. Select physical properties were linked to *a*, the model attrition limit and *b*, the model attrition rate. *a* is well correlated with the physical properties whereby 'stronger' minerals have a lower *a* value. However, there is no observed correlation between the attrition rate and mineral properties likely due to the greater dependence on factors such as particle concentration and particle morphology.

In studying the implications of mineral mixtures for attrition, it was found that the presence of cleavage plays a more important role than other bulk physical properties. Although the physical properties of garnet and olivine are notably different, the attrition rates and limits of each mineral were not significantly changed in the mixture experiments when compared to their individual experiments. In contrast, the physical properties of olivine and clinopyroxene are more similar yet the attrition rate of clinopyroxene was significantly increased when interacting with olivine. In kimberlites the implication of mineral mixtures is that modal proportions of xenocrysts do not reflect that of the mantle since all xenocrysts have different mass loss rates and limits. A consequence of this is that diamond grades are enhanced through attrition and that the high attrition rate of orthopyroxene contributes to the onset of turbulent ascent.

References

Abanades, J.C., Anthony, E.J., Lu, D.Y., Salvador, C., Alvarez, D., 2004. Capture of CO2 from combustion gases in a fluidized bed of CaO. AIChE J. https://doi.org/10.1002/aic.10132

Afanas'ev, V.P., Nikolenko, E.I., Tychkov, N.S., Titov, A.T., Tolstov, A. V., Kornilova, V.P., Sobolev, N. V., 2008. Mechanical abrasion of kimberlite indicator minerals: experimental investigations. Russ. Geol. Geophys. 49, 91–97. https://doi.org/10.1016/j.rgg.2008.01.001

Andronico, D., Scollo, S., Lo Castro, M.D., Cristaldi, A., Lodato, L., Taddeucci, J., 2014. Eruption dynamics and tephra dispersal from the 24 November 2006 paroxysm at South-East Crater, Mt Etna, Italy. J. Volcanol. Geotherm. Res. https://doi.org/10.1016/j.jvolgeores.2014.01.009

Archard, J.F., 1953. Contact and rubbing of flat surfaces. J. Appl. Phys. https://doi.org/10.1063/1.1721448

Arndt, N., Boullier, A.-M., Clement, J.P., Dubois, M., Schissel, D., 2006. What olivine, the neglected mineral, tells us about kimberlite petrogenesis. eEarth 1, 15–21.

Arndt, N.T., Guitreau, M., Boullier, A.M., Le Roex, A., Tommasi, A., Cordier, P., Sobolev, A., 2010. Olivine, and the origin of kimberlite. J. Petrol. 51, 573–602. https://doi.org/10.1093/petrology/egp080

Bayham, S.C., Breault, R., Monazam, E., 2016. Particulate solid attrition in CFB systems – An assessment for emerging technologies. Powder Technol. https://doi.org/10.1016/j.powtec.2016.08.016

Bemrose, C.R., Bridgwater, J., 1987. A review of attrition and attrition test methods. Powder Technol. https://doi.org/10.1016/0032-5910(87)80054-2

Bi, H.T., Grace, J.R., 1995. Flow regime diagrams for gas-solid fluidization and upward

transport. Int. J. Multiph. Flow. https://doi.org/10.1016/0301-9322(95)00037-X

Boerefijn, R., Ghadiri, M., Salatino, P., 2007. Chapter 25 Attrition in Fluidised Beds. Handb. Powder Technol. https://doi.org/10.1016/S0167-3785(07)12028-5

Brett, R.C., Russell, J.K., Andrews, G.D.M., Jones, T.J., 2015. The ascent of kimberlite: Insights from olivine. Earth Planet. Sci. Lett. 424, 119–131. https://doi.org/10.1016/j.epsl.2015.05.024

Brett, R.C., Russell, J.K., Moss, S., 2009. Origin of olivine in kimberlite: Phenocryst or impostor? Lithos. https://doi.org/10.1016/j.lithos.2009.04.030

Bridgwater, J., 2007. Chapter 3 Particle Breakage due to Bulk Shear. Handb. Powder Technol. https://doi.org/10.1016/S0167-3785(07)12006-6

Brown, R.J., Kavanagh, J., Sparks, R.S.J., Tait, M., Field, M., 2007. Mechanically disrupted and chemically weakened zones in segmented dike systems cause vent localization: Evidence from kimberlite volcanic systems. Geology. https://doi.org/10.1130/G23670A.1

Brown, R.J., Valentine, G.A., 2013. Physical characteristics of kimberlite and basaltic intraplate volcanism and implications of a biased kimberlite record. Bull. Geol. Soc. Am. https://doi.org/10.1130/B30749.1

Buckland, H.M., Eychenne, J., Rust, A.C., Cashman, K. V., 2018. Relating the physical properties of volcanic rocks to the characteristics of ash generated by experimental abrasion. J. Volcanol. Geotherm. Res. https://doi.org/10.1016/j.jvolgeores.2017.11.017

Cagnoli, B., Manga, M., 2003. Pumice-pumice collisions and the effect of the impact angle. Geophys. Res. Lett. 30, 22–25. https://doi.org/10.1029/2003GL017421

Campbell, M.E., Russell, J.K., Porritt, L.A., 2013. Thermomechanical milling of accessory lithics in volcanic conduits. Earth Planet. Sci. Lett. 377–378, 276–286.

https://doi.org/10.1016/j.epsl.2013.07.008

Chapman, J.G., Boxer, G.L., 2004. Size distribution analyses for estimating diamond grade and value. Lithos. https://doi.org/10.1016/j.lithos.2004.03.021

Chen, Z., Jim Lim, C., Grace, J.R., 2007. Study of limestone particle impact attrition. Chem. Eng. Sci. 62, 867–877. https://doi.org/10.1016/j.ces.2006.10.022

Chepurov, A.A., Sonin, V.M., Chepurov, A.I., Tomilenko, A.A., 2018. The Effects of the Concentration of Olivine Xenocrysts on the Viscosity of Kimberlite Melts: Experimental Evidence. J. Volcanol. Seismol. https://doi.org/10.1134/S0742046318020033

Cioni, R., Pistolesi, M., Bertagnini, A., Bonadonna, C., Hoskuldsson, A., Scateni, B., 2014. Insights into the dynamics and evolution of the 2010 Eyjafjallajökull summit eruption (Iceland) provided by volcanic ash textures. Earth Planet. Sci. Lett. https://doi.org/10.1016/j.epsl.2014.02.051

Clift R., Grace J.R., W.M.., 1999. “Bubbles, Drops and Particles”, 1978, Academic Press, New York., Journal of Fluid Mechanics. https://doi.org/10.1017/S0022112079221290

Cocco, R., Arrington, Y., Hays, R., Findlay, J., Karri, S.B.R., Knowlton, T.M., 2010. Jet cup attrition testing. Powder Technol. 200, 224–233. https://doi.org/10.1016/j.powtec.2010.02.029

Coltelli, M., Miraglia, L., Scollo, S., 2008. Characterization of shape and terminal velocity of tephra particles erupted during the 2002 eruption of Etna volcano, Italy. Bull. Volcanol. https://doi.org/10.1007/s00445-007-0192-8

Cox, E.., 1927. A method of Assigning Numerical and Percentage Values to the Degree of Roundness of Sand Grains. Source J. Paleontol. 73, 549–570.

Cummings, D.I., Kjarsgaard, B.A., Russell, H.A.J., Sharpe, D.R., 2014. Comminution of

indicator minerals in a tumbling mill: implications for mineral exploration, Geological Survey of Canada, Open File. https://doi.org/10.4095/293467

Cummings, D.I., Kjarsgaard, B.A., Russell, H.A.J., Sharpe, D.R., 2011. Abrasion of kimberlite pebbles in a tumbling mill : implications for diamond exploration. Geol. Surv. Canada, Curr. Res. 2011–07, 8. https://doi.org/10.4095/288022

Dawson, J.B., 1971. Advances in kimberlite geology. Earth Sci. Rev. https://doi.org/10.1016/0012-8252(71)90120-6

Dufek, J., Manga, M., 2008. In situ production of ash in pyroclastic flows. J. Geophys. Res. Solid Earth 113, 1–17. https://doi.org/10.1029/2007JB005555

Dufek, J., Manga, M., Patel, A., 2012. Granular disruption during explosive volcanic eruptions. Nat. Geosci. 5, 561–564. https://doi.org/10.1038/ngeo1524

Dufek, J., Wexler, J., Manga, M., 2009. Transport capacity of pyroclastic density currents: Experiments and models of substrate-flow interaction. J. Geophys. Res. Solid Earth 114, 1–13. https://doi.org/10.1029/2008JB006216

Eyre, T.S., 1976. Wear characteristics of metals. Tribol. Int. https://doi.org/10.1016/0301-679X(76)90077-3

Fedortchouk, Y., 2019. A new approach to understanding diamond surface features based on a review of experimental and natural diamond studies. Earth-Science Rev. https://doi.org/10.1016/j.earscirev.2019.02.013

Forsythe, W.L., Hertwig, W.R., 1949. Attrition Characteristics of Fluid Cracking Catalysts. Ind. Eng. Chem. https://doi.org/10.1021/ie50474a015

Freundt, A., Schmincke, H.U., 1992. Abrasion in pyroclastic flows. Geol. Rundschau 81, 383–389. https://doi.org/10.1007/BF01828605

Frye, L., 2007. Chapter 28 A New Concept for Addressing Bulk Solids Attrition in Pneumatic Conveying. Handb. Powder Technol. https://doi.org/10.1016/S0167-3785(07)12031-5

Fuerstenau, D.W., Abouzeid, A.Z., 2002. The energy efficiency of ball milling in comminution. Int. J. Miner. Process. https://doi.org/10.1016/S0301-7516(02)00039-X

Fulchini, F., Ghadiri, M., Borissova, A., Amblard, B., Bertholin, S., Cloupet, A., Yazdanpanah, M., 2019. Development of a methodology for predicting particle attrition in a cyclone by cfd-dem. Powder Technol. https://doi.org/10.1016/j.powtec.2019.08.101

Gernon, T.M., Fontana, G., Field, M., Sparks, R.S.J., Brown, R.J., Mac Niocaill, C., 2009a. Pyroclastic flow deposits from a kimberlite eruption: The Orapa South Crater, Botswana. Lithos. https://doi.org/10.1016/j.lithos.2009.04.016

Gernon, T.M., Gilbertson, M.A., Sparks, R.S.J., Field, M., 2009b. The role of gas-fluidisation in the formation of massive volcaniclastic kimberlite. Lithos 112, 439–451. https://doi.org/10.1016/j.lithos.2009.04.011

Gernon, T.M., Gilbertson, M.A., Sparks, R.S.J., Field, M., 2008. Gas-fluidisation in an experimental tapered bed: Insights into processes in diverging volcanic conduits. J. Volcanol. Geotherm. Res. 174, 49–56. https://doi.org/10.1016/j.jvolgeores.2007.12.034

Ghadiri, M., Zhang, Z., 2002. Impact attrition of particulate solids. Part 1: A theoretical model of chipping. Chem. Eng. Sci. 57, 3659–3669. https://doi.org/10.1016/S0009-2509(02)00240-3

Giuliani, A., 2018. Insights into kimberlite petrogenesis and mantle metasomatism from a review of the compositional zoning of olivine in kimberlites worldwide. Lithos. https://doi.org/10.1016/j.lithos.2018.04.029

Grace, J.R., 1986. Contacting modes and behaviour classification of gas—solid and other two-phase suspensions. Can. J. Chem. Eng. https://doi.org/10.1002/cjce.5450640301

Gravina, T., Lirer, L., Marzocchella, A., Petrosino, P., Salatino, P., 2004. Fluidization and attrition of pyroclastic granular solids. J. Volcanol. Geotherm. Res. https://doi.org/10.1016/j.jvolgeores.2004.06.005

Gupta, A., Yan, D., 2016. Introduction mineral Processing Design and Operation, Mineral Processing Design and Operations - 2nd Edition.

Gurney, J.J., Helmstaedt, H.H., Richardson, S.H., Shirey, S.B., 2010. Diamonds through time. Econ. Geol. https://doi.org/10.2113/gsecongeo.105.3.689

Gwyn, J.E., 1969. On the particle size distribution function and the attrition of cracking catalysts. AIChE J. https://doi.org/10.1002/aic.690150112

Harvey, S., Read, G., DesGagnes, B., Shimell, M., van Breugel, B., Fourie, L., 2013. Utilization of Olivine Macrocryst Grain Size and Abundance Data as a Proxy for Diamond Size and Grade in Pyroclastic Deposits of the Orion South Kimberlite, Fort à La Corne, Saskatchewan, Canada, in: Proceedings of 10th International Kimberlite Conference. https://doi.org/10.1007/978-81-322-1173-0_6

Heaman, L.M., Kjarsgaard, B.A., Creaser, R.A., 2004. The temporal evolution of North American kimberlites. Lithos. https://doi.org/10.1016/j.lithos.2004.03.047

Holden, E.J., Moss, S., Russell, J.K., Dentith, M.C., 2009. An image analysis method to determine crystal size distributions of olivine in kimberlite. Comput. Geosci. https://doi.org/10.1007/s10596-008-9115-9

Hutchings, I.M., 1993. Mechanisms of wear in powder technology: A review. Powder Technol. https://doi.org/10.1016/0032-5910(93)80035-9

Hutchings, I.M., 1992. Ductile-brittle transitions and wear maps for the erosion and abrasion of brittle materials. J. Phys. D. Appl. Phys. https://doi.org/10.1088/0022-3727/25/1A/033

Jankovics, M.É., Dobosi, G., Embey-Isztin, A., Kiss, B., Sági, T., Harangi, S., Ntaflos, T., 2013. Origin and ascent history of unusually crystal-rich alkaline basaltic magmas from the western Pannonian Basin. Bull. Volcanol. https://doi.org/10.1007/s00445-013-0749-7

Jones, T.J., McNamara, K., Eychenne, J., Rust, A.C., Cashman, K. V., Scheu, B., Edwards, R., 2016. Primary and secondary fragmentation of crystal-bearing intermediate magma. J. Volcanol. Geotherm. Res. 327, 70–83. https://doi.org/10.1016/j.jvolgeores.2016.06.022

Jones, T.J., Russell, J.K., 2018. Attrition in the kimberlite system. Mineral. Petrol. 112, 491–501. https://doi.org/10.1007/s00710-018-0580-0

Jones, T.J., Russell, J.K., 2017. Ash production by attrition in volcanic conduits and plumes/704/4111/704/2151/598 article. Sci. Rep. 7, 1–12. https://doi.org/10.1038/s41598-017-05450-6

Jones, T.J., Russell, J.K., Lim, C.J., Ellis, N., Grace, J.R., 2017. Pumice attrition in an air-jet. Powder Technol. 308, 298–305. https://doi.org/10.1016/j.powtec.2016.11.051

Jones, T.J., Russell, J.K., Porritt, L.A., Brown, R.J., 2014. Morphology and surface features of olivine in kimberlite: Implications for ascent processes. Solid Earth 5, 313–326. https://doi.org/10.5194/se-5-313-2014

Jones, T.J., Russell, J.K., Sasse, D., 2019. Modification of Mantle Cargo by Turbulent Ascent of Kimberlite. Front. Earth Sci. https://doi.org/10.3389/feart.2019.00134

Kamenetsky, V.S., Kamenetsky, M.B., Sobolev, A. V., Golovin, A. V., Demouchy, S., Faure, K., Sharygin, V. V., Kuzmin, D. V., 2008. Olivine in the Udachnaya-East kimberlite (Yakutia, Russia): Types, compositions and origins. J. Petrol. 49, 823–839. https://doi.org/10.1093/petrology/egm033

Kang, D.H., Ko, C.K., Lee, D.H., 2017. Attrition characteristics of iron ore by an air jet in gas-

solid fluidized beds. Powder Technol. 316, 69–78. https://doi.org/10.1016/j.powtec.2016.12.092

Kavanagh, J.L., Burns, A.J., Hilmi Hazim, S., Wood, E.P., Martin, S.A., Hignett, S., Dennis, D.J.C., 2018. Challenging dyke ascent models using novel laboratory experiments: Implications for reinterpreting evidence of magma ascent and volcanism. J. Volcanol. Geotherm. Res. https://doi.org/10.1016/j.jvolgeores.2018.01.002

Kavanagh, J.L., Sparks, R.S.J., 2011. Insights of dyke emplacement mechanics from detailed 3D dyke thickness datasets. J. Geol. Soc. London. https://doi.org/10.1144/0016-76492010-137

Kavanagh, J.L., Sparks, R.S.J., 2009. Temperature changes in ascending kimberlite magma. Earth Planet. Sci. Lett. https://doi.org/10.1016/j.epsl.2009.07.011

Khokhryakakov, A.F., Pal'Yanov, Y.N., 2010. Influence of the fluid composition on diamond dissolution forms in carbonate melts. Am. Mineral. https://doi.org/10.2138/am.2010.3451

Kim, J.Y., Ellis, N., Lim, C.J., Grace, J.R., 2019. Attrition of binary mixtures of solids in a jet attrition unit. Powder Technol. 352, 445–452. https://doi.org/10.1016/j.powtec.2019.05.010

Knight, A., Ellis, N., Grace, J.R., Lim, C.J., 2014. CO2 sorbent attrition testing for fluidized bed systems. Powder Technol. https://doi.org/10.1016/j.powtec.2014.06.013

Kueppers, U., Putz, C., Spieler, O., Dingwell, D.B., 2012. Abrasion in pyroclastic density currents: Insights from tumbling experiments. Phys. Chem. Earth 45–46, 33–39. https://doi.org/10.1016/j.pce.2011.09.002

Kunii, D., Levenspiel, O., Kunii, D., Levenspiel, O., 1969. Entrainment and Elutriation from Fluidized Beds. J. Chem. Eng. JAPAN. https://doi.org/10.1252/jcej.2.84

Kurszlaukis, S., Barnett, W.P., 2003. Volcanological and structural aspects of the Venetia kimberlite cluster - a case study of South African kimberlite maar-diatreme volcanoes.

South African J. Geol. https://doi.org/10.2113/106.2-3.165

Little, L., Mainza, A.N., Becker, M., Wiese, J., 2017. Fine grinding: How mill type affects particle shape characteristics and mineral liberation. Miner. Eng. https://doi.org/10.1016/j.mineng.2017.05.007

Liu, E.J., Cashman, K. V., Rust, A.C., 2015. Optimising shape analysis to quantify volcanic ash morphology. GeoResJ. https://doi.org/10.1016/j.grj.2015.09.001

Manga, M., Patel, A., Dufek, J., 2011. Rounding of pumice clasts during transport: Field measurements and laboratory studies. Bull. Volcanol. 73, 321–333. https://doi.org/10.1007/s00445-010-0411-6

Marzocchella, A., Salatino, P., Di Pastena, V., Lirer, L., 2000. Transient fluidization and segregation of binary mixtures of particles. AIChE J. https://doi.org/10.1002/aic.690461110

McGetchin, T.R., Ullrich, G.W., 1973. Xenoliths in Maars and Diatremes with inferences for the Moon, Mars, and Venus. J. Geophys. Res. https://doi.org/10.1029/jb078i011p01833

Mellors, R.A., Sparks, R.S.J., 1991. Spatter-rich pyroclastic flow deposits on Santorini, Greece. Bull. Volcanol. https://doi.org/10.1007/BF00280225

Mitchell, R., 1973. Composition of olivine, silica activity and oxygen fugacity in kimberlite. Lithos. https://doi.org/10.1016/0024-4937(73)90080-7

Moss, S., Russell, J.K., 2011. Fragmentation in kimberlite: Products and intensity of explosive eruption. Bull. Volcanol. 73, 983–1003. https://doi.org/10.1007/s00445-011-0504-x

Moss, S., Russell, J.K., Smith, B.H.S., Brett, R.C., 2010. Olivine crystal size distributions in kimberlite. Am. Mineral. 95, 527–536. https://doi.org/10.2138/am.2010.3277

Mueller, S.B., Lane, S.J., Kueppers, U., 2015. Lab-scale ash production by abrasion and collision experiments of porous volcanic samples. J. Volcanol. Geotherm. Res. 302, 163–172.

https://doi.org/10.1016/j.jvolgeores.2015.07.013

Nadolski, S., Klein, B., Kumar, A., Davaanyam, Z., 2014. An energy benchmarking model for mineral comminution. Miner. Eng. 65, 178–186. https://doi.org/10.1016/j.mineng.2014.05.026

Nairn, I.A., Wood, C.P., Bailey, R.A., 1994. The Reporoa Caldera, Taupo Volcanic Zone: source of the Kaingaroa Ignimbrites. Bull. Volcanol. https://doi.org/10.1007/BF00302833

Napier-Munn, T., Wills, B.A., 2005. Wills' Mineral Processing Technology, Wills' Mineral Processing Technology. https://doi.org/10.1016/B978-0-7506-4450-1.X5000-0

Novák-Szabó, T., Sipos, A.Á., Shaw, S., Bertoni, D., Pozzebon, A., Grottoli, E., Sarti, G., Ciavola, P., Domokos, G., Jerolmack, D.J., 2018. Universal characteristics of particle shape evolution by bed-load chipping. Sci. Adv. https://doi.org/10.1126/sciadv.aao4946

Ozyer, C.A., Hicock, S.R., 2011. Identifying kimberlite indicator mineral dispersal trains in the Pelly Bay region, Nunavut, Canada using GIS interpolation. Geochemistry Explor. Environ. Anal. https://doi.org/10.1144/1467-7873/10-IM-035

Pacciani, R., Müller, C.R., Davidson, J.F., Dennis, J.S., Hayhurst, A.N., 2008. How does the concentration of CO2 affect Its uptake by a synthetic ca-based solid sorbent? AIChE J. https://doi.org/10.1002/aic.11611

Peltonen, P., Kinnunen, K.A., Huhma, H., 2002. Petrology of two diamondiferous eclogite xenoliths from the Lahtojoki kimberlite pipe, eastern Finland. Lithos 63, 151–164. https://doi.org/10.1016/S0024-4937(02)00119-6

Persikov, E.S., Bukhtiyarov, P.G., Sokol, A.G., 2015. Change in the viscosity of kimberlite and basaltic magmas during their origin and evolution (prediction). Russ. Geol. Geophys. https://doi.org/10.1016/j.rgg.2015.05.005

Petcovic, H.L., Dufek, J.D., 2005. Modeling magma flow and cooling in dikes: Implications for emplacement of Columbia River flood basalts. J. Geophys. Res. Solid Earth. https://doi.org/10.1029/2004JB003432

Peterson, T.D., Lecheminant, A.N., 1993. Glimmerite xenoliths in early Proterozoic ultrapotassic rocks from the Churchill Province. Can. Mineral.

Pilbeam, L.H., Nielsen, T.F.D., Waight, T.E., 2013. Digestion fractional crystallization (DFC): An important process in the genesis of kimberlites. Evidence from olivine in the Majuagaa kimberlite, Southern West Greenland. J. Petrol. 54, 1399–1425. https://doi.org/10.1093/petrology/egt016

Pokhilenko, N.P., Afanas'ev, V.P., Vavilov, M.A., 2010. Behavior of kimberlite indicator minerals during the formation of mechanical dispersion halos in glacial settings. Lithol. Miner. Resour. https://doi.org/10.1134/S0024490210040024

Polakowski, C., Sochan, A., Bieganowski, A., Ryzak, M., Földényi, R., Tóth, J., 2014. Influence of the sand particle shape on particle size distribution measured by laser diffraction method. Int. Agrophysics. https://doi.org/10.2478/intag-20014-0008

Radziszewski, P., 2013. Energy recovery potential in comminution processes. Miner. Eng. https://doi.org/10.1016/j.mineng.2012.12.002

Ray, Y.C., Jiang, T.S., Wen, C.Y., 1987. Particle attrition phenomena in a fluidized bed. Powder Technol. https://doi.org/10.1016/0032-5910(87)80128-6

Reppenhagen, J., Werther, J., 2000. Catalyst attrition in cyclones. Powder Technol. https://doi.org/10.1016/S0032-5910(99)00290-9

Russell, J.K., Porritt, L.A., Lavallé, Y., Dingwell, D.B., 2012. Kimberlite ascent by assimilation-fuelled buoyancy. Nature 481, 352–356. https://doi.org/10.1038/nature10740

Russell, K., Jones, T., Andrews, G., Edwards, B., Pell, J., 2017. Transport and eruption of mantle xenoliths : A lagging problem 1–3.

Sadrai, S., 2007. High velocity impact fragmentation and the energy efficiency of comminution 287. https://doi.org/10.14288/1.0081177

Sadrai, S., Meech, J.A., Ghomshei, M., Sassani, F., Tromans, D., 2006. Influence of impact velocity on fragmentation and the energy efficiency of comminution. Int. J. Impact Eng. 33, 723–734. https://doi.org/10.1016/j.ijimpeng.2006.09.063

Salman, A.D., Biggs, C.A., Fu, J., Angyal, I., Szabó, M., Hounslow, M.J., 2002. An experimental investigation of particle fragmentation using single particle impact studies. Powder Technol. 128, 36–46. https://doi.org/10.1016/S0032-5910(02)00151-1

Scala, F., 2013. Fluidized Bed Technologies for Near-Zero Emission Combustion and Gasification, Fluidized Bed Technologies for Near-Zero Emission Combustion and Gasification. https://doi.org/10.1533/9780857098801

Scala, F., Chirone, R., Salatino, P., 2013. Attrition phenomena relevant to fluidized bed combustion and gasification systems, in: Fluidized Bed Technologies for Near-Zero Emission Combustion and Gasification. https://doi.org/10.1533/9780857098801.1.254

Scott Smith, B.H., 2008. Canadian kimberlites: Geological characteristics relevant to emplacement. J. Volcanol. Geotherm. Res. https://doi.org/10.1016/j.jvolgeores.2007.12.023

Scott Smith, B.H., Nowicki, T.E., Russell, J.K., Webb, K.J., Mitchell, R.H., Hetman, C.M., Harder, M., Skinner, E.M.W., Robey, J.A., 2013. Kimberlite Terminology and Classification, in: Proceedings of 10th International Kimberlite Conference. https://doi.org/10.1007/978-81-322-1173-0_1

Smith, D., Griffin, W.L., 2005. Garnetite xenoliths and mantle - Water interactions below the

Colorado Plateau, Southwestern United States. J. Petrol. 46, 1901–1924. https://doi.org/10.1093/petrology/egi042

Smolders, K., Baeyens, J., 1998. Hydrodynamic modeling of circulating fluidized beds. Adv. Powder Technol. https://doi.org/10.1016/S0921-8831(08)60591-9

Sparks, R.S.J., 2013. Kimberlite Volcanism. Annu. Rev. Earth Planet. Sci. https://doi.org/10.1146/annurev-earth-042711-105252

Sparks, R.S.J., 1976. Grain size variations in ignimbrites and implications for the transport of pyroclastic flows. Sedimentology 23, 147–188. https://doi.org/10.1111/j.1365-3091.1976.tb00045.x

Sparks, R.S.J., Baker, L., Brown, R.J., Field, M., Schumacher, J., Stripp, G., Walters, A., 2006. Dynamical constraints on kimberlite volcanism. J. Volcanol. Geotherm. Res. 155, 18–48. https://doi.org/10.1016/j.jvolgeores.2006.02.010

Spera, F.J., 1984. Carbon dioxide in petrogenesis III: role of volatiles in the ascent of alkaline magma with special reference to xenolith-bearing mafic lavas. Contrib. to Mineral. Petrol. https://doi.org/10.1007/BF00380167

Sun, P., Grace, J.R., Lim, C.J., Anthony, E.J., 2007. Sequential capture of CO2 and SO2 in a pressurized TGA simulating FBC conditions. Environ. Sci. Technol. https://doi.org/10.1021/es062445e

Takashimizu, Y., Iiyoshi, M., 2016. New parameter of roundness R: circularity corrected by aspect ratio. Prog. Earth Planet. Sci. https://doi.org/10.1186/s40645-015-0078-x

Tardin, P.R., Goldstein, L., Lombardi, G., Pagliuso, J.D., 2001. On the mechanical attrition and fragmentation of particles in a fast fluidized bed. Ind. Eng. Chem. Res. https://doi.org/10.1021/ie990816c

Tromans, D., 2008. Mineral comminution: Energy efficiency considerations. Miner. Eng. https://doi.org/10.1016/j.mineng.2007.12.003

Walters, A.L., Phillips, J.C., Brown, R.J., Field, M., Gernon, T., Stripp, G., Sparks, R.S.J., 2006. The role of fluidisation in the formation of volcaniclastic kimberlite: Grain size observations and experimental investigation. J. Volcanol. Geotherm. Res. 155, 119–137. https://doi.org/10.1016/j.jvolgeores.2006.02.005

Weit, A., Roche, O., Dubois, T., Manga, M., 2019. Maximum Solid Phase Concentration in Geophysical Turbulent Gas-Particle Flows: Insights From Laboratory Experiments. Geophys. Res. Lett. https://doi.org/10.1029/2019GL082658

Weit, A., Roche, O., Dubois, T., Manga, M., 2018. Experimental Measurement of the Solid Particle Concentration in Geophysical Turbulent Gas-Particle Mixtures. J. Geophys. Res. Solid Earth. https://doi.org/10.1029/2018JB015530

Werther, J., Xi, W., 1993a. Jet attrition of catalyst particles in gas fluidized beds. Powder Technol. 76, 39–46. https://doi.org/10.1016/0032-5910(93)80039-D

Werther, J., Xi, W., 1993b. Jet attrition of catalyst particles in gas fluidized beds. Powder Technol. https://doi.org/10.1016/0032-5910(93)80039-D

Wills, B. a, Napier-munn, T., 2006. Mineral Processing Technology:An Introduction to the Practical Aspects of Ore Treatment and Mineral Recovery, October. https://doi.org/10.1016/B978-075064450-1/50003-5

Wilson, L., Head, J.W., 2007. An integrated model of kimberlite ascent and eruption. Nature 447, 53–57. https://doi.org/10.1038/nature05692

Wilson, L., Sparks, R.S.J., Walker, G.P.L., 1980. Explosive volcanic eruptions — IV. The control of magma properties and conduit geometry on eruption column behaviour. Geophys.

J. R. Astron. Soc. https://doi.org/10.1111/j.1365-246X.1980.tb02613.x

Win, T.T., Davies, R.M., Griffin, W.L., Wathanakul, P., French, D.H., 2001. Distribution and characteristics of diamonds from Myanmar. J. Asian Earth Sci. https://doi.org/10.1016/S1367-9120(00)00055-9

Woolsey, T.S., McCallum, M.E., Schumm, S.A., 2019. Physical modeling of diatreme emplacement. Int. Kimberl. Conf. Ext. Abstr. 1, 325–328. https://doi.org/10.29173/ikc919

Woolsey, T.S., McCallum, M.E., Schumm, S.A., 1975. Modeling of diatreme emplacement by fluidization. Phys. Chem. Earth. https://doi.org/10.1016/0079-1946(75)90004-X

Xiao, G., Grace, J.R., Lim, C.J., 2014. Evolution of limestone particle size distribution in an air-jet attrition apparatus. Ind. Eng. Chem. Res. 53, 15845–15851. https://doi.org/10.1021/ie501745h

Xiao, G., Grace, J.R., Lim, C.J., 2012. Limestone particle attrition in high-velocity air jets. Ind. Eng. Chem. Res. 51, 556–560. https://doi.org/10.1021/ie201698r

Xiao, G., Grace, J.R., Lim, C.J., 2011. Attrition characteristics and mechanisms for limestone particles in an air-jet apparatus. Powder Technol. 207, 183–191. https://doi.org/10.1016/j.powtec.2010.10.028

Zhang, H., Kong, W., Tan, T., Gilles, F., Baeyens, J., 2017. Experiments support an improved model for particle transport in fluidized beds. Sci. Rep. https://doi.org/10.1038/s41598-017-10597-3

Zhang, Z., Fedortchouk, Y., Hanley, J.J., 2015. Evolution of diamond resorption in a silicic aqueous fluid at 1-3GPa: Application to kimberlite emplacement and mantle metasomatism. Lithos. https://doi.org/10.1016/j.lithos.2015.04.003

Zhang, Z., Ghadiri, M., 2002. Impact attrition of particulate solids. Part 2: Experimental work.

Chem. Eng. Sci. 57, 3671–3686. https://doi.org/10.1016/S0009-2509(02)00241-5

Appendices

Appendix A Experiment Apparatus

A.1 Experiment Apparatus Photograph

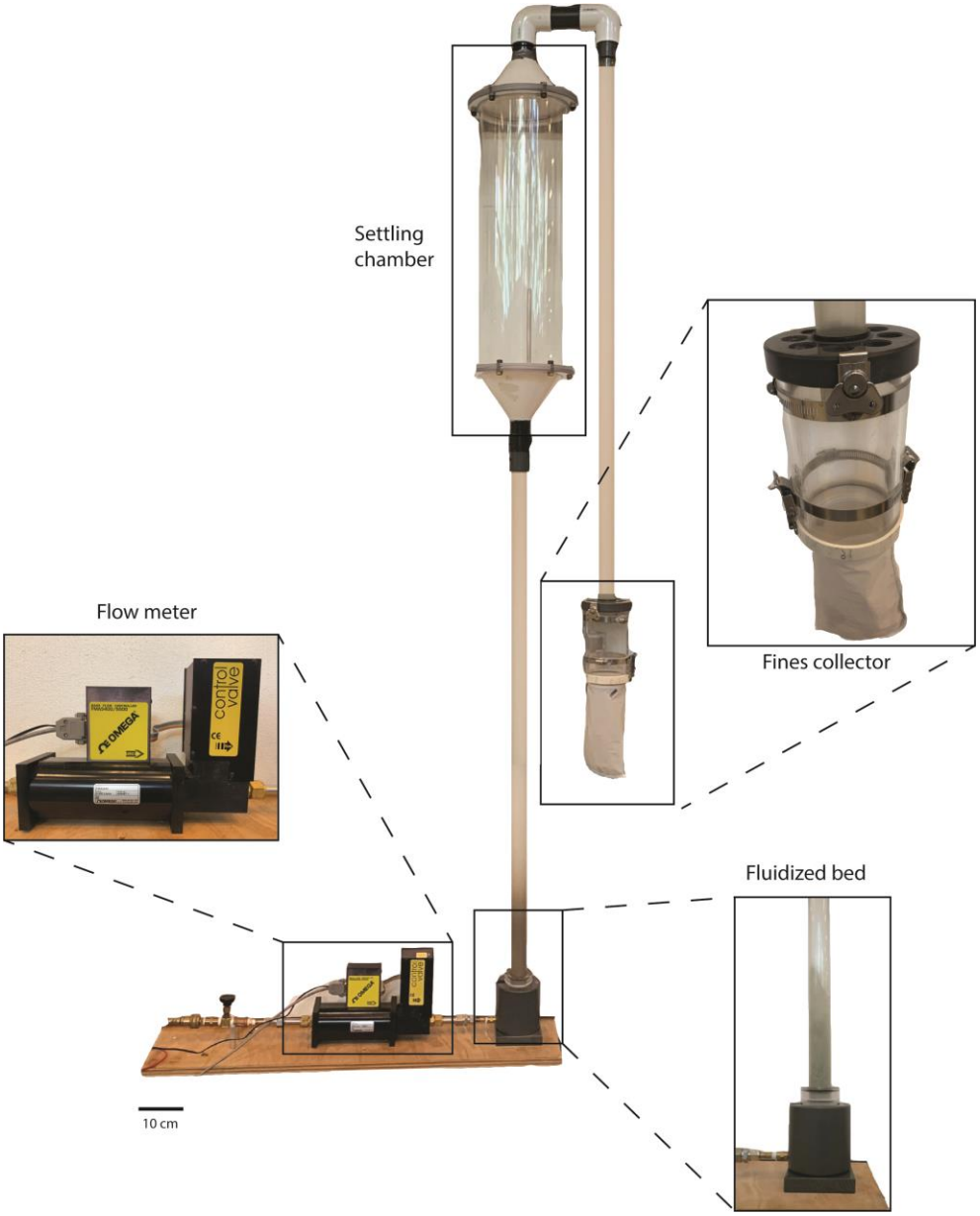

Figure A.1-1. Photograph of the experiment apparatus.

Appendix B Mineral Supplementary Information

B.1 Photographs of Minerals Used in This Study

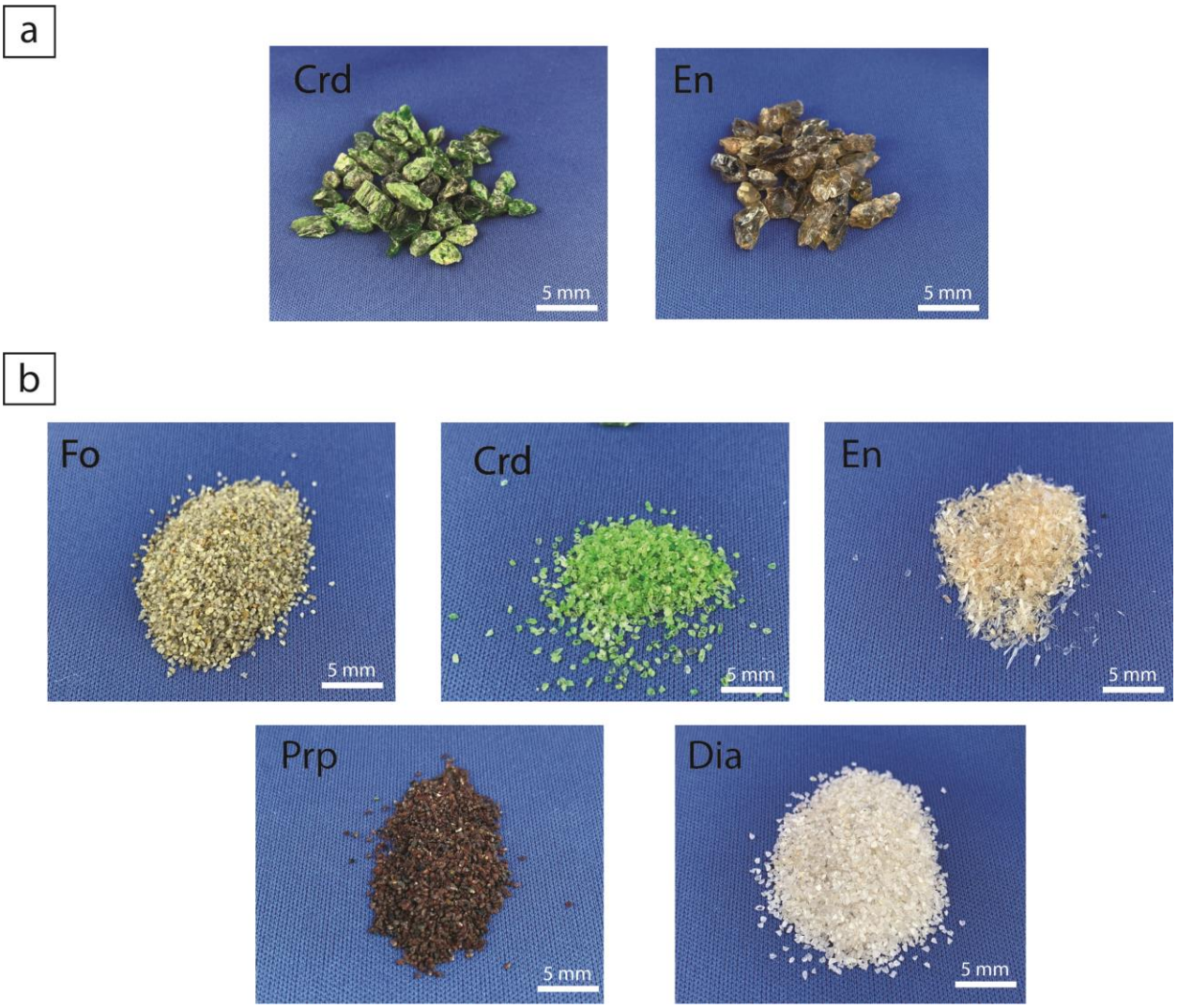

Figure B.1-1. Minerals used in this study: Chrome Diopside (Crd), Enstatite (En), Forsterite (Fo), Pyrope (Prp) and Diamond (Dia). a) Crd and En were not received in the desired grain size and were manually crushed. b) Starting material at desired size range.

B.2 Mineral X-Ray Diffraction Analysis

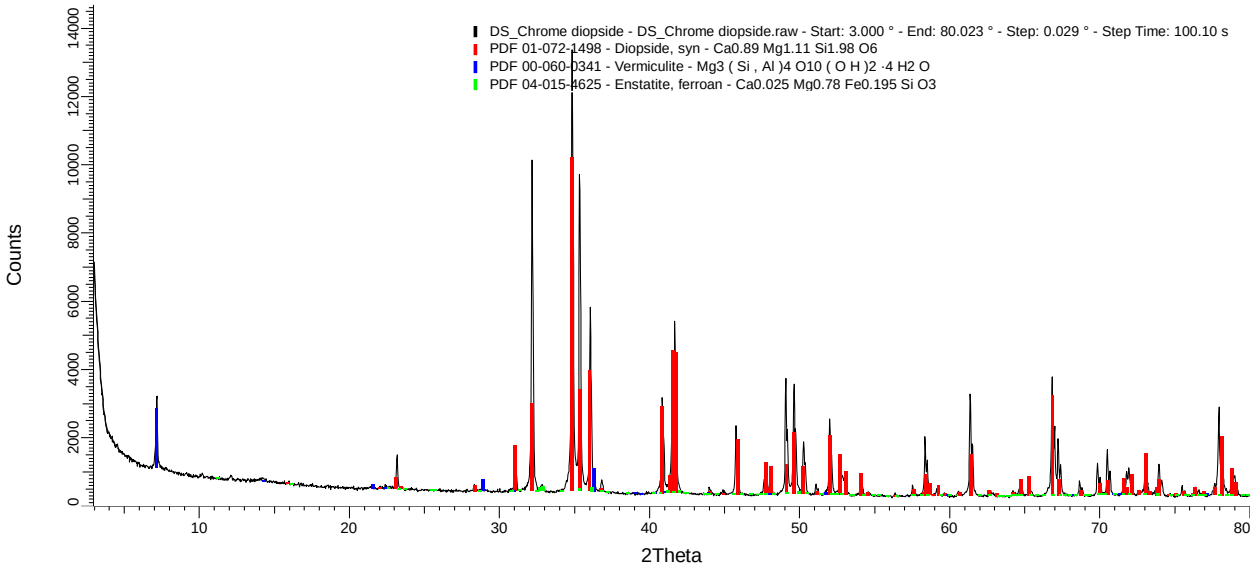

Figure B.2-1. X-ray diffraction analysis of chrome diopside sample. Black line shows sample observed intensity at each step. Colored lines are best fit diffraction patterns of select mineral phases.

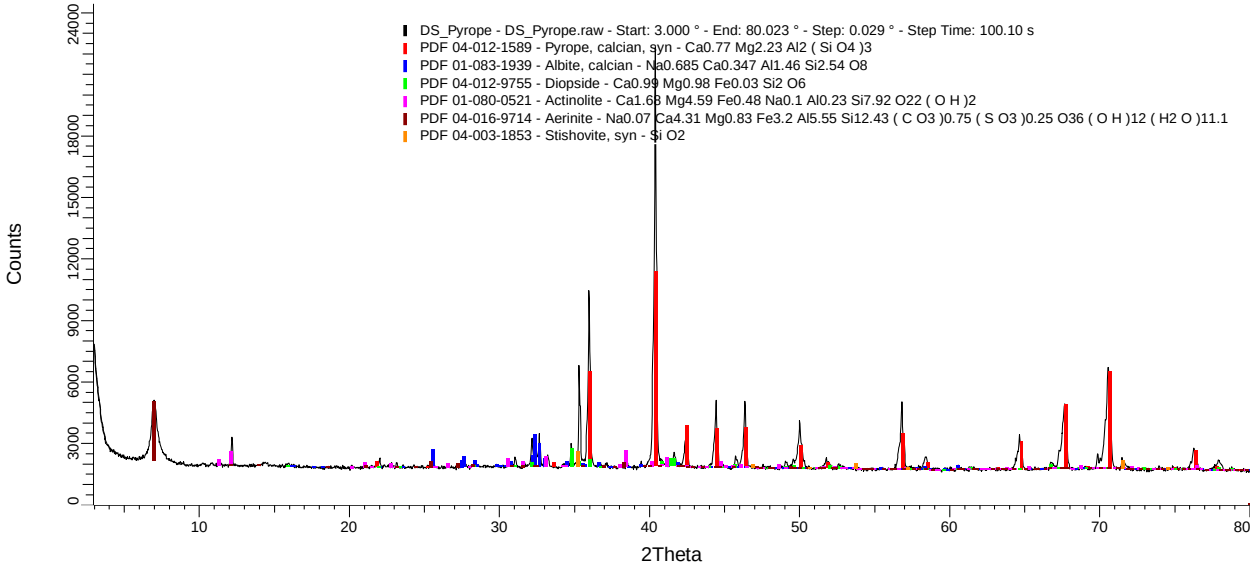

Figure B.2-2. X-ray diffraction analysis of pyrope sample. Black line shows sample observed intensity at each step. Colored lines are best fit diffraction patterns of select mineral phases.

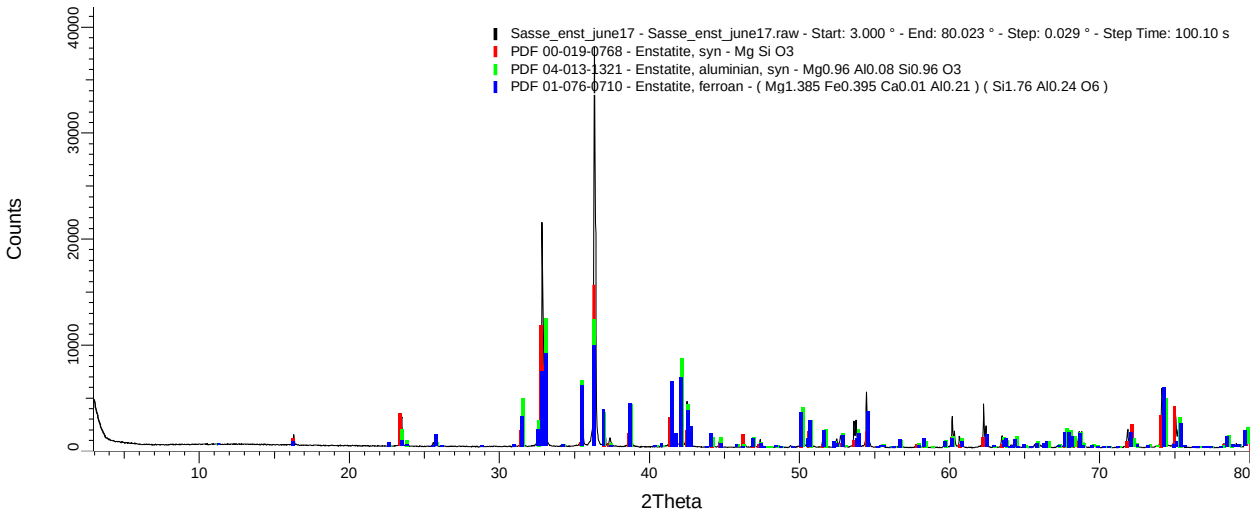

Figure B.2-3. X-ray diffraction analysis of enstatite sample. Black line shows sample observed intensity at each step. Colored lines are best fit diffraction patterns of select mineral phases.

Appendix C Select Datasets Analyzed

C.1 Grain Size Distribution Datasets

Plotting bins [µm]	1-A	1-B	1-C	1-D	1-E	1-F	1-G	1-H	1-I	1-J	1-K
0.010741	0	0	0	0	0	0	0	0	0	0	0
0.0123325	0	0	0	0	0	0	0	0	0	0	0
0.0141595	0	0	0	0	0	0	0	0	0	0	0
0.016257	0	0	0	0	0	0	0	0	0	0	0
0.0186655	0	0	0	0	0	0	0	0	0	0	0
0.021431	0	0	0	0	0	0	0	0	0	0	0
0.024606	0	0	0	0	0	0	0	0	0	0	0
0.0282515	0	0	0	0	0	0	0	0	0	0	0
0.032437	0	0	0	0	0	0	0	0	0	0	0
0.0372425	0	0	0	0	0	0	0	0	0	0	0
0.04276	0	0	0	0	0	0	0	0	0	0	0
0.049095	0	0	0	0	0	0	0	0	0	0	0
0.0563685	0	0	0	0	0	0	0	0	0	0	0
0.0647195	0	0	0	0	0	0	0	0	0	0	0
0.074308	0	0	0	0	0	0	0	0	0	0	0
0.085317	0	0	0	0	0	0	0	0	0	0	0
0.097957	0	0	0	0	0	0	0	0	0	0	0
0.1124695	0	0	0	0	0	0	0	0	0	0	0
0.129132	0	0	0	0	0	0	0	0	0	0	0
0.1482635	0	0	0	0	0	0	0	0	0	0	0
0.1702295	0	0	0	0	0	0	0	0	0	0	0
0.19545	0	0	0	0	0	0	0	0	0	0	0
0.2244065	0	0	0	0	0	0	0	0	0	0	0

0.257653	0	0	0	0	0	0	0	0	0	0	0
0.2958255	0	0	0	0	0	0	0	0	0	0	0
0.339653	0	0	0	0	0	0	0	0	0	0	0
0.3899735	0	0	0	0	0.00098	0	0	0	0	0	0
0.4477495	0	0.00244	0.00558	0.00584	0.00985	0.00925	0.0151	0.0151	0.02171	0.03253	0.05478
0.5140855	0	0.00437	0.01014	0.0114	0.01768	0.01928	0.03493	0.03586	0.05242	0.07202	0.12737
0.590249	0	0.00624	0.0146	0.01764	0.02613	0.03116	0.06157	0.06472	0.09546	0.12476	0.227
0.6776965	0	0.00749	0.01783	0.02298	0.03297	0.04191	0.09026	0.09552	0.14206	0.18179	0.33383
0.7781	0	0.00851	0.0207	0.02869	0.03992	0.05395	0.12418	0.13274	0.19878	0.25018	0.46347
0.8933785	0	0.00932	0.02332	0.03485	0.04734	0.06756	0.1624	0.17565	0.26375	0.32775	0.61082
1.0257355	0	0.01021	0.02655	0.04255	0.0571	0.08512	0.20718	0.22792	0.34107	0.41865	0.78363
1.1777015	0	0.01142	0.031	0.05235	0.07056	0.10789	0.25784	0.28988	0.42945	0.52061	0.97661
1.3521825	0	0.01322	0.03737	0.06488	0.08933	0.13728	0.31419	0.36242	0.52833	0.63208	1.18581
1.5525135	0	0.01571	0.04586	0.07984	0.11365	0.17242	0.37225	0.44128	0.63028	0.74396	1.39295
1.782524	0	0.019	0.05653	0.09667	0.14327	0.21169	0.42797	0.52145	0.72759	0.84724	1.58018
2.0466115	0	0.02304	0.069	0.11418	0.1765	0.2518	0.4761	0.59546	0.81025	0.93108	1.72667
2.349824	0	0.02781	0.08287	0.13134	0.21149	0.28988	0.51349	0.65801	0.87192	0.98917	1.82042
2.6979585	0	0.03323	0.0976	0.14713	0.2459	0.32319	0.53854	0.70528	0.90906	1.01863	1.85642
3.097671	0	0.03917	0.11257	0.16077	0.27728	0.34983	0.55152	0.73589	0.92187	1.02085	1.83815
3.5566025	0	0.04548	0.12723	0.17184	0.30362	0.36906	0.55449	0.75113	0.91403	1.00095	1.77639
4.083526	0	0.0519	0.14093	0.18015	0.32318	0.38111	0.55045	0.75394	0.89159	0.96662	1.68729
4.688515	0	0.05825	0.1534	0.18599	0.33538	0.38728	0.54245	0.74817	0.86082	0.92533	1.58629
5.3831355	0	0.06419	0.16415	0.18964	0.34007	0.3891	0.53301	0.73741	0.82763	0.88405	1.48835
6.1806665	0	0.06958	0.17316	0.1916	0.33808	0.38814	0.52323	0.72377	0.79493	0.84598	1.40048
7.096355	0	0.07408	0.18011	0.19217	0.33069	0.38551	0.51329	0.70821	0.76425	0.8127	1.32695
8.147706	0	0.07764	0.185	0.19157	0.31924	0.38154	0.50193	0.6895	0.73348	0.78168	1.26318
9.354818	0	0.08006	0.18751	0.18986	0.30561	0.37617	0.48813	0.66643	0.70076	0.75053	1.20459
10.740768	0	0.08135	0.18748	0.18694	0.29088	0.36873	0.47051	0.63666	0.66228	0.71501	1.14213
12.3320515	0	0.08148	0.18465	0.18286	0.27685	0.35902	0.44983	0.60068	0.61789	0.6746	1.07269

14.1590895	0	0.08053	0.17885	0.17757	0.26431	0.34682	0.42725	0.559	0.56747	0.62927	0.99362
16.25681	0	0.07861	0.1703	0.17144	0.25454	0.33315	0.40647	0.51629	0.51625	0.5843	0.9118
18.6653155	0	0.07577	0.15917	0.16461	0.24771	0.31875	0.39065	0.47619	0.46866	0.54452	0.83407
21.43065	0	0.07215	0.1462	0.15741	0.24362	0.30476	0.38305	0.44364	0.4311	0.51622	0.77145
24.6056785	0	0.06782	0.13188	0.14977	0.24099	0.29118	0.38505	0.42079	0.407	0.50267	0.73087
28.2510985	0	0.06305	0.11724	0.1418	0.23815	0.27776	0.39644	0.40894	0.39885	0.50533	0.71804
32.436601	0	0.05821	0.10302	0.1335	0.23333	0.26333	0.41539	0.40734	0.40666	0.52293	0.7347
37.242201	0	0.05384	0.09014	0.12513	0.22523	0.24672	0.43828	0.41402	0.42839	0.55156	0.77892
42.759768	0	0.05043	0.07899	0.1169	0.2132	0.22644	0.46025	0.42541	0.45935	0.58483	0.84398
49.0947825	0	0.04826	0.0695	0.10893	0.19724	0.20131	0.47536	0.4362	0.49143	0.61369	0.91671
56.3683525	0	0.04724	0.06101	0.10104	0.17783	0.17077	0.47742	0.43952	0.5133	0.62739	0.97736
64.719528	0	0.04681	0.05216	0.09284	0.1554	0.13568	0.46111	0.4279	0.51203	0.61527	1.0021
74.30796	0	0.04608	0.04289	0.08359	0.13105	0.09812	0.42346	0.3951	0.47608	0.56968	0.96781
85.3169535	0	0.044	0.0304	0.07348	0.10446	0.06603	0.36394	0.33862	0.40041	0.48722	0.85817
97.9569695	0	0.03979	0.0242	0.06463	0.07928	0.03841	0.28768	0.26125	0.29288	0.37645	0.67939
112.469649	0	0.03346	0.02147	0.05342	0.05511	0.01833	0.20191	0.17584	0.18176	0.2458	0.45001
137.5	0	0.23859	0.35041	0.37495	0.38103	0.35714	0.77309	0.63258	0.60193	0.74832	1.0461
165	0	0.2843	0.44064	0.40719	0.52666	0.55049	1.02747	0.75243	0.75936	0.63689	1.27411
196	0	0.30664	0.49487	0.4494	0.61148	0.58742	1.1385	0.8939	0.90726	1.20584	1.41032
231	0	0.37298	0.60672	0.55427	0.79479	0.77616	1.55086	1.23786	1.23867	1.50093	2.21432
275	0	0.7094	1.23717	1.20182	1.71337	1.77662	4.18988	3.12275	3.27641	3.9204	6.85112
327.5	0	0.84208	1.40393	1.31144	1.85427	1.85526	3.3748	2.68377	3.02169	2.84901	4.11361
390	0	1.04041	1.72662	1.67369	2.18121	2.22522	3.55409	3.04924	3.37159	3.71872	5.34371
462.5	0	1.72274	2.96921	3.05595	4.16749	4.88809	5.91866	7.48474	7.8045	11.7754	19.4301
550	0	14.98	22.1742	30.202	37.5745	45.1793	41.8554	46.7295	46.8475	43.6063	15.6022
655	100	77.6816	64.7837	55.9795	42.4102	32.5289	20.9487	14.794	10.5078	5.09228	0.61889
855	0	0	0	0	0	0	0	0	0	0	0

Table C.1-1. Olivine grain size distribution data created from merging a sieving data (≥137.5 µm) with Mastersizer data (<137.5 µm). The sizes used to plot the data are taken as the midpoint of original size interva

Plotting bins [µm]	2-A	2-B	2-C	2-D	2-E	2-F
0.010741	0	0	0	0	0	0
0.0123325	0	0	0	0	0	0
0.0141595	0	0	0	0	0	0
0.016257	0	0	0	0	0	0
0.0186655	0	0	0	0	0	0
0.021431	0	0	0	0	0	0
0.024606	0	0	0	0	0	0
0.0282515	0	0	0	0	0	0
0.032437	0	0	0	0	0	0
0.0372425	0	0	0	0	0	0
0.04276	0	0	0	0	0	0
0.049095	0	0	0	0	0	0
0.0563685	0	0	0	0	0	0
0.0647195	0	0	0	0	0	0
0.074308	0	0	0	0	0	0
0.085317	0	0	0	0	0	0
0.097957	0	0	0	0	0	0
0.1124695	0	0	0	0	0	0
0.129132	0	0	0	0	0	0
0.1482635	0	0	0	0	0	0
0.1702295	0	0	0	0	0	0
0.19545	0	0	0	0	0	0
0.2244065	0	0	0	0	0	0
0.257653	0	0	0	0	0	0
0.2958255	0	0	0	0	0	0
0.339653	0	0	0	0	0	0
0.3899735	0	0	0	0	0	0
0.4477495	0	0	0	0	0	0
0.5140855	0	0	0	0	0	0
0.590249	0	0	0	0	0	0
0.6776965	0	0	0	0	0	0
0.7781	0	0	0	0	0	0
0.8933785	0	0	0	0	0	0
1.0257355	0	0.00064	0.00411	0.00708	0.00999	0.01534
1.1777015	0	0.00477	0.02214	0.03813	0.05659	0.08298
1.3521825	0	0.02159	0.0649	0.11177	0.17624	0.25354
1.5525135	0	0.03892	0.1089	0.18754	0.3091	0.45129
1.782524	0	0.06019	0.15934	0.2744	0.46663	0.68869
2.0466115	0	0.08239	0.2088	0.35958	0.62671	0.93028
2.349824	0	0.10475	0.25527	0.43961	0.7816	1.16086
2.6979585	0	0.12632	0.29704	0.51154	0.9245	1.36795

3.097671	0	0.14636	0.33326	0.57392	1.05095	1.54406
3.5566025	0	0.16435	0.36349	0.62598	1.15771	1.68424
4.083526	0	0.17964	0.38719	0.66678	1.2412	1.78366
4.688515	0	0.19212	0.40505	0.69755	1.30213	1.8445
5.3831355	0	0.20171	0.41805	0.71994	1.34197	1.87184
6.1806665	0	0.2088	0.42772	0.73659	1.36436	1.87274
7.096355	0	0.2135	0.43482	0.74882	1.3715	1.85231
8.147706	0	0.21619	0.44016	0.75802	1.36581	1.81337
9.354818	0	0.21705	0.44383	0.76434	1.34953	1.75844
10.740768	0	0.21637	0.44607	0.7682	1.32478	1.68746
12.3320515	0	0.21441	0.44674	0.76934	1.29509	1.60411
14.1590895	0	0.21138	0.44583	0.76778	1.26244	1.50883
16.25681	0	0.2076	0.44345	0.76367	1.22962	1.40873
18.6653155	0	0.20316	0.43955	0.75696	1.19544	1.30677
21.43065	0	0.19815	0.43395	0.74731	1.15635	1.20945
24.6056785	0	0.19226	0.42581	0.7333	1.10275	1.11735
28.2510985	0	0.18521	0.41395	0.71288	1.0237	1.03094
32.436601	0	0.17645	0.3965	0.68282	0.90639	0.94526
37.242201	0	0.16558	0.37154	0.63984	0.74855	0.85432
42.759768	0	0.15226	0.33701	0.58037	0.55434	0.74969
49.0947825	0	0.13652	0.29149	0.50198	0.35922	0.62381
56.3683525	0	0.11902	0.23511	0.40489	0.19583	0.47343
64.719528	0	0.10128	0.17116	0.29476	0.05125	0.30725
74.30796	0	0.08669	0.108	0.186	0.00251	0.14217
85.3169535	0	0.07769	0.06858	0.11809	0	0.03727
97.9569695	0	0.07023	0.05256	0.09052	0	0.00702
112.469649	0	0.06136	0.04176	0.07192	0	0.0012
137.5	0	0.53893	0.62449	1.23711	1.19384	2.02702
165	0	0.49312	0.6082	0.72683	1.36254	1.91977
196	0	0.51929	0.75452	1.1572	2.01929	2.40133
231	0	0.72866	1.29268	1.8117	4.34642	3.6495
275	0	1.23623	2.02015	3.76232	8.9812	7.5056
327.5	0	2.01792	4.00216	5.34916	15.7146	12.3126
390	0	3.99176	5.43354	8.54506	11.3775	9.26269
462.5	0	7.64812	7.50224	10.3224	12.921	10.5094
550	0	12.7549	19.2147	16.1291	9.32291	9.33107
655	100	65.1162	48.2042	33.1469	5.45591	5.08987
855	0	0	0	0	0	0

Table C.1-2. Orthopyroxene grain size distribution data created from merging a sieving data (≥137.5 µm) with Mastersizer data (<137.5 µm). The sizes used to plot the data are taken as the midpoint of original size intervals.

Plotting bins [µm]	3-A	3-B	3-C	3-D	3-E	3-F	3-G	3-H	3-I	3-J	3-K	3-L
0.010741	0	0	0	0	0	0	0	0	0	0	0	0
0.0123325	0	0	0	0	0	0	0	0	0	0	0	0
0.0141595	0	0	0	0	0	0	0	0	0	0	0	0
0.016257	0	0	0	0	0	0	0	0	0	0	0	0
0.0186655	0	0	0	0	0	0	0	0	0	0	0	0
0.021431	0	0	0	0	0	0	0	0	0	0	0	0
0.024606	0	0	0	0	0	0	0	0	0	0	0	0
0.0282515	0	0	0	0	0	0	0	0	0	0	0	0
0.032437	0	0	0	0	0	0	0	0	0	0	0	0
0.0372425	0	0	0	0	0	0	0	0	0	0	0	0
0.04276	0	0	0	0	0	0	0	0	0	0	0	0
0.049095	0	0	0	0	0	0	0	0	0	0	0	0
0.0563685	0	0	0	0	0	0	0	0	0	0	0	0
0.0647195	0	0	0	0	0	0	0	0	0	0	0	0
0.074308	0	0	0	0	0	0	0	0	0	0	0	0
0.085317	0	0	0	0	0	0	0	0	0	0	0	0
0.097957	0	0	0	0	0	0	0	0	0	0	0	0
0.1124695	0	0	0	0	0	0	0	0	0	0	0	0
0.129132	0	0	0	0	0	0	0	0	0	0	0	0
0.1482635	0	0	0	0	0	0	0	0	0	0	0	0
0.1702295	0	0	0	0	0	0	0	0	0	0	0	0
0.19545	0	0	0	0	0	0	0	0	0	0	0	0
0.2244065	0	0	0	0	0	0	0	0	0	0	0	0
0.257653	0	0.00019	0.00039	0.0007	0.00111	0.00167	0.0021	0.00362	0.00292	0.0046	0.00526	0.00522
0.2958255	0	0.00106	0.00383	0.00556	0.00812	0.00955	0.01562	0.02007	0.01747	0.02648	0.045	0.03259

0.339653	0	0.00184	0.00605	0.01057	0.01619	0.02025	0.03017	0.03785	0.04286	0.05762	0.08991	0.08998
0.3899735	0	0.00241	0.00827	0.01496	0.02328	0.02908	0.04317	0.05181	0.06526	0.084	0.1357	0.1433
0.4477495	0	0.00289	0.01005	0.01891	0.02991	0.03763	0.0553	0.06502	0.08852	0.11014	0.18182	0.20043
0.5140855	0	0.00322	0.01135	0.02215	0.03549	0.04485	0.06561	0.07604	0.10987	0.13285	0.22471	0.25458
0.590249	0	0.00342	0.01226	0.02488	0.04038	0.05116	0.07473	0.08556	0.13009	0.15332	0.26602	0.30753
0.6776965	0	0.00351	0.01287	0.0273	0.04498	0.05701	0.0833	0.09425	0.14978	0.17287	0.30703	0.36063
0.7781	0	0.00355	0.01344	0.0299	0.05024	0.06355	0.0929	0.10363	0.17149	0.19503	0.35335	0.42045
0.8933785	0	0.00359	0.01421	0.03312	0.05696	0.07171	0.10479	0.11491	0.197	0.22274	0.40893	0.49151
1.0257355	0	0.0037	0.01551	0.0375	0.06618	0.08275	0.12059	0.12964	0.22909	0.26	0.47995	0.58109
1.1777015	0	0.00392	0.01758	0.04325	0.07823	0.09704	0.14064	0.14816	0.26813	0.30801	0.56738	0.68987
1.3521825	0	0.00427	0.02063	0.05049	0.09323	0.11476	0.16497	0.1705	0.31404	0.3673	0.67105	0.81707
1.5525135	0	0.00477	0.02468	0.05884	0.11015	0.13469	0.19168	0.19504	0.36319	0.43376	0.78254	0.95178
1.782524	0	0.0054	0.02968	0.0678	0.1277	0.15534	0.2186	0.22	0.41152	0.50231	0.89181	1.08125
2.0466115	0	0.00615	0.03538	0.07661	0.14396	0.17459	0.24274	0.24297	0.45369	0.56558	0.98545	1.18913
2.349824	0	0.00701	0.04152	0.08471	0.15742	0.19092	0.26204	0.2624	0.48634	0.61821	1.05446	1.26491
2.6979585	0	0.00799	0.04773	0.09165	0.16697	0.20333	0.27528	0.27743	0.50806	0.65693	1.09481	1.30458
3.097671	0	0.0091	0.05363	0.09724	0.17216	0.21161	0.28238	0.28804	0.5196	0.68133	1.10825	1.31122
3.5566025	0	0.01034	0.05884	0.1015	0.17321	0.21614	0.28417	0.29491	0.52322	0.69345	1.10089	1.29282
4.083526	0	0.01168	0.06299	0.10455	0.17085	0.2177	0.28212	0.29908	0.52197	0.69689	1.08136	1.25997
4.688515	0	0.01311	0.06593	0.10663	0.16609	0.21729	0.27791	0.30181	0.51876	0.69585	1.05798	1.22186
5.3831355	0	0.0146	0.06756	0.1079	0.16007	0.21585	0.2731	0.30408	0.51565	0.6938	1.03733	1.18525
6.1806665	0	0.01615	0.06807	0.10856	0.15363	0.21409	0.26875	0.30659	0.51332	0.69272	1.02194	1.15143
7.096355	0	0.01776	0.06782	0.10873	0.1476	0.21256	0.26554	0.30949	0.51123	0.69282	1.01125	1.11897
8.147706	0	0.01951	0.06729	0.10858	0.14228	0.21158	0.26363	0.3127	0.50781	0.69271	1.00122	1.0825
9.354818	0	0.02148	0.06701	0.10835	0.13802	0.21148	0.26306	0.3158	0.50131	0.69009	0.98688	1.03847
10.740768	0	0.02383	0.06729	0.10828	0.13472	0.21253	0.26372	0.31858	0.49002	0.68233	0.96251	0.98323
12.332052	0	0.02663	0.06811	0.10856	0.13225	0.21493	0.26561	0.3209	0.47384	0.66793	0.92572	0.92047
14.15909	0	0.03001	0.06904	0.10928	0.13008	0.21894	0.26894	0.32318	0.45342	0.64635	0.87588	0.85511
16.25681	0	0.03385	0.06908	0.11016	0.12755	0.22447	0.27382	0.32618	0.43198	0.62001	0.81889	0.79884

18.665316	0	0.03809	0.06701	0.11041	0.12345	0.23114	0.28017	0.3309	0.41241	0.59147	0.76077	0.75991
21.43065	0	0.04228	0.06118	0.10846	0.1165	0.23756	0.28676	0.3378	0.39785	0.56438	0.70979	0.7433
24.605679	0	0.04602	0.05171	0.10228	0.1052	0.24187	0.29158	0.34685	0.38917	0.54055	0.67002	0.74403
28.251099	0	0.04867	0.03587	0.08981	0.09009	0.24181	0.29173	0.35715	0.38579	0.52146	0.64386	0.74755
32.436601	0	0.04969	0.02251	0.07055	0.07181	0.2357	0.28446	0.36757	0.38548	0.50722	0.62983	0.73123
37.242201	0	0.04858	0.0158	0.04432	0.06183	0.22298	0.26796	0.37662	0.38518	0.4976	0.62403	0.67122
42.759768	0	0.04502	0.01356	0.02308	0.05707	0.20432	0.24167	0.38279	0.38143	0.49123	0.61918	0.55293
49.094783	0	0.03889	0.01258	0.01725	0.05104	0.18137	0.20652	0.38431	0.37091	0.48551	0.6051	0.38572
56.368353	0	0.03033	0.01173	0.01514	0.0434	0.15618	0.16466	0.37921	0.35095	0.47622	0.56983	0.24083
64.719528	0	0.02144	0.01107	0.01344	0.03476	0.13028	0.11889	0.36524	0.31971	0.4574	0.50121	0.15029
74.30796	0	0.01277	0.01056	0.01182	0.02738	0.10462	0.072	0.34042	0.27692	0.42297	0.40219	0.08425
85.316954	0	0.00904	0.01009	0.00967	0.02546	0.07936	0.04165	0.30281	0.2239	0.36599	0.26535	0.04747
97.95697	0	0.00629	0.00953	0.0066	0.024	0.05358	0.02989	0.25308	0.1632	0.28984	0.17426	0.02208
112.46965	0	0.00472	0.00876	0.00275	0.02194	0.03081	0.02062	0.19188	0.10363	0.18817	0.10427	0.00616
137.5	0	0.05807	0.09342	0.08769	0.16377	0.22586	0.27661	0.56676	0.43314	0.66855	0.75085	0.54761
165	0	0.05437	0.08081	0.12435	0.14164	0.26239	0.35638	0.51666	0.64902	0.73391	0.93	0.75317
196	0	0.04698	0.08485	0.1284	0.15316	0.29297	0.44547	0.59657	0.74183	0.92242	1.20244	1.26338
231	0	0.05303	0.10168	0.16151	0.19179	0.42417	0.71687	1.05124	1.36938	1.94116	2.76028	2.82117
275	0	0.0933	0.16566	0.26559	0.37274	0.86193	1.54203	2.43797	3.38293	4.72158	6.67667	6.5177
327.5	0	0.12216	0.27205	0.4048	0.63975	1.36835	2.18556	3.27221	4.16286	5.34253	7.20287	6.79139
390	0	0.20069	0.43636	0.71972	1.12499	1.991	3.52678	4.42953	5.40964	5.8817	7.89708	6.30976
462.5	0	0.47588	0.70909	1.26305	1.73357	3.0453	7.86844	7.09208	7.77436	8.44381	14.6982	11.4383
550	0	6.31402	6.57908	12.8981	15.9328	21.8011	29.6021	35.6092	36.4932	35.2895	21.7815	26.2402
655	100	91.8227	89.957	81.234	75.4929	63.0363	45.1642	33.391	24.5456	15.9368	7.28515	7.02434
855	0	0	0	0	0	0	0	0	0	0	0	0

Table C.1-3. Clinopyroxene grain size distribution data created from merging a sieving data (≥137.5 µm) with Mastersizer data (<137.5 µm). The sizes used to plot the data are taken as the midpoint of original size intervals.

Plotting bins [µm]	4-A	4-B	4-C	4-D	4-E	4-F	4-G	4-H	4-I	4-J	4-K
0.010741	0	0	0	0	0	0	0	0	0	0	0
0.0123325	0	0	0	0	0	0	0	0	0	0	0
0.0141595	0	0	0	0	0	0	0	0	0	0	0
0.016257	0	0	0	0	0	0	0	0	0	0	0
0.0186655	0	0	0	0	0	0	0	0	0	0	0
0.021431	0	0	0	0	0	0	0	0	0	0	0
0.024606	0	0	0	0	0	0	0	0	0	0	0
0.0282515	0	0	0	0	0	0	0	0	0	0	0
0.032437	0	0	0	0	0	0	0	0	0	0	0
0.0372425	0	0	0	0	0	0	0	0	0	0	0
0.04276	0	0	0	0	0	0	0	0	0	0	0
0.049095	0	0	0	0	0	0	0	0	0	0	0
0.0563685	0	0	0	0	0	0	0	0	0	0	0
0.0647195	0	0	0	0	0	0	0	0	0	0	0
0.074308	0	0	0	0	0	0	0	0	0	0	0
0.085317	0	0	0	0	0	0	0	0	0	0	0
0.097957	0	0	0	0	0	0	0	0	0	0	0
0.1124695	0	0	0	0	0	0	0	0	0	0	0
0.129132	0	0	0	0	0	0	0	0	0	0	0
0.1482635	0	0	0	0	0	0	0	0	0	0	0
0.1702295	0	0	0	0	0	0	0	0	0	0	0
0.19545	0	0	0	0	0	0	0	0	0	0	0
0.2244065	0	0	0	0	0	0	0	0	0	0	0
0.257653	0	0	0	0	0	0	0	0	0	0	0
0.2958255	0	0	0	0	0	0	0	0	0	0	0
0.339653	0	0	0	4E-05	0.00012	0.00032	8E-05	0.00015	0.0005	0.00063	0.00011
0.3899735	0	0.0004	0	0.00122	0.00273	0.00553	0.00406	0.00629	0.00872	0.01279	0.00775

0.4477495	0	0.00173	0	0.00356	0.00577	0.0117	0.01181	0.01917	0.01965	0.02684	0.03089
0.5140855	0	0.00269	0.00034	0.00526	0.00833	0.01698	0.01935	0.03198	0.02947	0.03989	0.05851
0.590249	0	0.00336	0.00056	0.0065	0.0101	0.0208	0.02633	0.04354	0.0373	0.05119	0.09039
0.6776965	0	0.00385	0.00067	0.00732	0.01122	0.02346	0.03285	0.05458	0.04379	0.06171	0.12557
0.7781	0	0.00414	0.00072	0.00782	0.0118	0.02523	0.03982	0.06598	0.04964	0.07296	0.1654
0.8933785	0	0.00436	0.00076	0.00824	0.01224	0.02701	0.04832	0.07942	0.05643	0.08733	0.20955
1.0257355	0	0.00462	0.0008	0.00887	0.01303	0.02989	0.06007	0.09724	0.06618	0.10811	0.25967
1.1777015	0	0.00507	0.00086	0.01003	0.01467	0.03495	0.0762	0.12079	0.08053	0.13756	0.31427
1.3521825	0	0.00585	0.00096	0.01198	0.01762	0.04319	0.09763	0.15109	0.10086	0.17758	0.37216
1.5525135	0	0.00701	0.00111	0.01482	0.02206	0.05501	0.12354	0.18666	0.12691	0.22673	0.42844
1.782524	0	0.00859	0.0013	0.0186	0.02813	0.07053	0.15246	0.22531	0.1578	0.28236	0.47867
2.0466115	0	0.01058	0.00151	0.0232	0.03568	0.08919	0.18168	0.2634	0.19127	0.33922	0.51784
2.349824	0	0.01292	0.00176	0.02849	0.04461	0.11031	0.20864	0.29782	0.22511	0.39217	0.54327
2.6979585	0	0.01555	0.00203	0.03427	0.05465	0.13281	0.2308	0.32563	0.2567	0.43572	0.55392
3.097671	0	0.01834	0.00233	0.04027	0.06548	0.15536	0.24626	0.34487	0.28363	0.46542	0.55087
3.5566025	0	0.02117	0.00265	0.04624	0.07678	0.1767	0.25423	0.35489	0.30411	0.47882	0.53686
4.083526	0	0.02391	0.00302	0.05187	0.0881	0.19544	0.25501	0.35628	0.31701	0.47574	0.51565
4.688515	0	0.02646	0.00346	0.057	0.09918	0.21081	0.24998	0.35074	0.32237	0.45833	0.49064
5.3831355	0	0.02872	0.00398	0.06139	0.10951	0.22203	0.2413	0.34069	0.321	0.43085	0.46514
6.1806665	0	0.03075	0.00462	0.06502	0.1189	0.22914	0.23116	0.32842	0.31451	0.39769	0.44055
7.096355	0	0.03257	0.00538	0.0678	0.1268	0.23221	0.22181	0.31625	0.30508	0.36412	0.418
8.147706	0	0.03439	0.00627	0.06983	0.13306	0.23179	0.21453	0.30529	0.29473	0.33303	0.39672
9.354818	0	0.03637	0.00723	0.07115	0.13718	0.22846	0.21022	0.2965	0.28581	0.30746	0.37673
10.740768	0	0.03874	0.00825	0.07188	0.13904	0.22266	0.20863	0.2897	0.27977	0.28755	0.35718
12.3320515	0	0.04152	0.00922	0.07208	0.13844	0.21502	0.20898	0.28483	0.278	0.27382	0.33928
14.1590895	0	0.04472	0.01007	0.0718	0.13543	0.2057	0.20985	0.28148	0.28102	0.26526	0.32427
16.25681	0	0.04793	0.01074	0.07105	0.13031	0.19528	0.20935	0.27959	0.28855	0.2615	0.31522
18.6653155	0	0.0507	0.01121	0.06978	0.12332	0.18377	0.20522	0.27887	0.29947	0.26175	0.31478
21.43065	0	0.05229	0.01156	0.06795	0.11504	0.17156	0.19517	0.2787	0.31105	0.26508	0.32496

24.6056785	0	0.05202	0.01198	0.06552	0.10578	0.15848	0.17711	0.27773	0.31986	0.27021	0.34625
28.2510985	0	0.04936	0.01277	0.0627	0.09615	0.14482	0.15049	0.2739	0.32184	0.27539	0.3766
32.436601	0	0.0441	0.01432	0.0599	0.08663	0.13067	0.11695	0.26453	0.31366	0.27889	0.41233
37.242201	0	0.03668	0.01703	0.05784	0.07792	0.11654	0.08058	0.24697	0.29367	0.27885	0.44728
42.759768	0	0.02756	0.02119	0.05731	0.07055	0.10276	0.05422	0.21862	0.2622	0.27349	0.47437
49.0947825	0	0.01887	0.02688	0.05897	0.06484	0.08956	0.04323	0.17838	0.22174	0.26099	0.48598
56.3683525	0	0.01517	0.03379	0.06301	0.06074	0.07681	0.04256	0.12784	0.17631	0.23982	0.47562
64.719528	0	0.01342	0.04129	0.06901	0.0577	0.06391	0.04734	0.06922	0.13016	0.2085	0.43915
74.30796	0	0.0117	0.04834	0.07574	0.05473	0.05083	0.05561	0.02864	0.08943	0.16902	0.37775
85.3169535	0	0.00988	0.05382	0.08144	0.05097	0.03696	0.06408	0.00847	0.05632	0.11952	0.29556
97.9569695	0	0.00794	0.05662	0.08405	0.04485	0.02769	0.07053	0.00093	0.03542	0.07982	0.20886
112.469649	0	0.00579	0.05605	0.08204	0.03886	0.01975	0.07312	0	0.01501	0.05142	0.14101
137.5	0	0.07003	0.29262	0.38522	0.30878	0.27037	0.55062	0.40489	0.33215	0.49708	0.66342
165	0	0.10356	0.15128	0.22324	0.32457	0.35828	0.46677	0.62139	0.51888	0.69171	0.69735
196	0	0.09885	0.15935	0.2273	0.3542	0.37895	0.4968	0.66729	0.52467	0.71821	0.78021
231	0	0.11903	0.18086	0.32404	0.53682	0.56015	0.7254	1.00025	0.76928	1.24676	1.23522
275	0	0.24478	0.39131	0.61696	0.9489	1.11135	1.44262	2.02858	1.70283	2.12465	2.56226
327.5	0	0.2932	0.46862	0.73467	1.00886	1.17887	1.50404	2.07859	1.80631	2.1107	2.32475
390	0	0.44518	0.73622	1.11215	1.51811	1.75694	2.13868	2.76575	2.56546	2.86726	3.02141
462.5	0	0.74174	1.83214	1.79811	2.51042	2.62162	3.6939	4.23666	4.13947	4.98075	5.15835
550	0	5.93663	11.9052	15.4091	18.5012	21.4601	25.8675	29.2826	31.2559	29.7297	29.7191
655	100	91.0352	83.3749	77.2064	71.1491	65.5117	57.4625	48.5627	48.2125	44.748	39.0339
855	0	0	0	0	0	0	0	0	0	0	0

Table C.1-4. Garnet grain size distribution data created from merging a sieving data (≥137.5 µm) with Mastersizer data (<137.5 µm). The sizes used to plot the data are taken as the midpoint of original size interval

Plotting bins [µm]	5-A	5-B	5-C	5-D	5-E	5-F	5-G	5-H
0.010741	0	0	0	0	0	0	0	0
0.0123325	0	0	0	0	0	0	0	0
0.0141595	0	0	0	0	0	0	0	0
0.016257	0	0	0	0	0	0	0	0
0.0186655	0	0	0	0	0	0	0	0
0.021431	0	0	0	0	0	0	0	0
0.024606	0	0	0	0	0	0	0	0
0.0282515	0	0	0	0	0	0	0	0
0.032437	0	0	0	0	0	0	0	0
0.0372425	0	0	0	0	0	0	0	0
0.04276	0	0	0	0	0	0	0	0
0.049095	0	0	0	0	0	0	0	0
0.0563685	0	0	0	0	0	0	0	0
0.0647195	0	0	0	0	0	0	0	0
0.074308	0	0	0	0	0	0	0	0
0.085317	0	0	0	0	0	0	0	0
0.097957	0	0	0	0	0	0	0	0
0.1124695	0	0	0	0	0	0	0	0
0.129132	0	0	0	0	0	0	0	0
0.1482635	0	0	0	0	0	0	0	0
0.1702295	0	0	0	0	0	0	0	0
0.19545	0	0	0	0	0	0.00039	0	0.00096
0.2244065	0	1.1E-05	0	0.00059	0.00085	0.00172	0	0.00334
0.257653	0	9.2E-05	0.00013	0.0023	0.00325	0.00407	0.00052	0.00641
0.2958255	0	0.00032	0.00074	0.00323	0.00435	0.00541	0.00268	0.00828
0.339653	0	0.00037	0.00109	0.00385	0.00508	0.00648	0.00321	0.0098
0.3899735	0	0.00043	0.00135	0.00425	0.00553	0.00713	0.00361	0.01056
0.4477495	0	0.00048	0.00157	0.00441	0.00569	0.00742	0.00383	0.01073
0.5140855	0	0.00052	0.00174	0.00441	0.00566	0.00749	0.00389	0.01051
0.590249	0	0.00057	0.00188	0.00434	0.00558	0.00757	0.00385	0.01024
0.6776965	0	0.00063	0.00202	0.00438	0.00563	0.00793	0.00382	0.01035
0.7781	0	0.0007	0.0022	0.00468	0.006	0.00888	0.00388	0.01133
0.8933785	0	0.00085	0.00242	0.00539	0.00684	0.01066	0.00416	0.01361
1.0257355	0	0.0011	0.00273	0.00665	0.00829	0.01352	0.00474	0.0176
1.1777015	0	0.00134	0.00315	0.00849	0.01034	0.01743	0.00567	0.02336
1.3521825	0	0.00158	0.0037	0.01091	0.01301	0.02235	0.00699	0.03088
1.5525135	0	0.00186	0.00439	0.01375	0.01612	0.02792	0.00866	0.0397
1.782524	0	0.00217	0.00526	0.01688	0.01956	0.0338	0.01065	0.0493
2.0466115	0	0.00251	0.00635	0.02004	0.02315	0.0395	0.01291	0.05886
2.349824	0	0.00291	0.00772	0.02307	0.02685	0.04469	0.0154	0.06774
2.6979585	0	0.00337	0.00944	0.0258	0.03066	0.04915	0.0181	0.07531

3.097671	0	0.0039	0.01151	0.02815	0.03465	0.0528	0.02097	0.0812
3.5566025	0	0.00448	0.01393	0.0301	0.03897	0.05571	0.02399	0.08533
4.083526	0	0.00508	0.01656	0.03168	0.04367	0.05802	0.02709	0.08785
4.688515	0	0.00563	0.01927	0.03302	0.04886	0.05994	0.03025	0.0892
5.3831355	0	0.00608	0.02185	0.03422	0.05442	0.06158	0.03339	0.08989
6.1806665	0	0.00641	0.02423	0.03548	0.06031	0.06306	0.03656	0.09048
7.096355	0	0.00663	0.02638	0.0369	0.06621	0.06439	0.03978	0.09136
8.147706	0	0.00686	0.02858	0.03869	0.07202	0.0656	0.04323	0.0928
9.354818	0	0.00728	0.0312	0.04089	0.07741	0.06674	0.04696	0.09475
10.740768	0	0.00814	0.03499	0.04363	0.08245	0.06803	0.05124	0.09711
12.3320515	0	0.00969	0.04051	0.04685	0.08714	0.06972	0.05603	0.09954
14.1590895	0	0.01217	0.04844	0.05057	0.09197	0.07226	0.0615	0.10186
16.25681	0	0.01556	0.05856	0.0546	0.09731	0.07597	0.06741	0.10388
18.6653155	0	0.01971	0.07035	0.05884	0.10373	0.08106	0.07372	0.10565
21.43065	0	0.02408	0.08193	0.06295	0.11122	0.08716	0.08009	0.10726
24.6056785	0	0.02799	0.09103	0.06665	0.11943	0.0935	0.08656	0.109
28.2510985	0	0.03057	0.09477	0.06952	0.127	0.09863	0.0932	0.11121
32.436601	0	0.03107	0.09083	0.07119	0.13201	0.10092	0.10062	0.11426
37.242201	0	0.0292	0.07809	0.0713	0.13182	0.09874	0.10949	0.11822
42.759768	0	0.02479	0.05743	0.06944	0.12386	0.09093	0.12051	0.12262
49.0947825	0	0.01887	0.03209	0.06534	0.10602	0.07741	0.1337	0.12598
56.3683525	0	0.01311	0.01142	0.05903	0.07759	0.05963	0.148	0.12586
64.719528	0	0.01113	0.00037	0.05012	0.04612	0.04236	0.16105	0.11892
74.30796	0	0.01098	0	0.04411	0.0103	0.03799	0.16919	0.10315
85.3169535	0	0.01077	0	0.03587	0.00048	0.03359	0.16847	0.07523
97.9569695	0	0.01025	0	0.02594	0	0.03102	0.15558	0.04726
112.469649	0	0.00934	0	0.01702	0	0.02666	0.1292	0.01538
137.5	0	0.25986	0.05599	0.13876	0.12612	0.19206	0.37601	0.17344
165	0	0.09412	0.08713	0.15115	0.18749	0.20184	0.25058	0.24056
196	0	0.09009	0.09524	0.1525	0.17198	0.18626	0.22445	0.23583
231	0	0.10757	0.12766	0.16802	0.2057	0.23774	0.25259	0.27434
275	0	0.17143	0.2614	0.26991	0.34666	0.34069	0.42478	0.48517
327.5	0	0.25076	0.35123	0.4467	0.49571	0.49173	0.60232	0.69397
390	0	0.42892	0.59845	0.69704	0.87205	0.91437	1.11152	1.17643
462.5	0	1.19397	1.9561	1.96223	2.36862	2.47558	3.50742	3.25833
550	0	10.3626	14.6822	15.6931	19.7468	20.0106	18.4805	22.0103
655	100	86.6491	80.7424	78.8811	73.3314	72.8323	72.3855	68.3776
855	0	0	0	0	0	0	0	0

Table C.1-5. Diamond grain size distribution data created from merging a sieving data (≥137.5 µm) with Mastersizer data (<137.5 µm). The sizes used to plot the data are taken as the midpoint of original size intervals

Appendix D University of Alberta Diavik Xenolith Analysis

D.1 Morphology Measurements of Select Eclogite and Peridotite Xenoliths

Sample	Pipe	Rock Type	Scan name	Dry Mass (g)	Sample Density (g cm^{-3})	Long Axis (cm)	Short Axis (cm)	Int Axis (cm)	Surface Area (cm^2)	Volume (cm^3)
DDM_265	A154N	Eclogite	Scan_05	1269.7	3.27251	12.1	5.4	9.8	290.556	387.99
DDM_301	A154N	Eclogite	Scan_04	803.4	3.07216	10.1	5.1	8.3	219.933	261.51
DDM_16	A154N	Eclogite	Scan_06	433.7	3.27543	7.2	5	6.7	137.818	132.41
DDM_379	A154N	Eclogite	Scan_07	823.9	3.33252	10.3	5.6	8.1	210.902	247.23
DDM_260	A154N	Eclogite	Scan_08	304.4	3.37248	6.5	4.2	6.4	105.845	90.26
DDM_194	A154N	Eclogite	Scan_10	296.3	3.19978	6.9	3.7	5.6	110.533	92.6
DDM_215	A154N	Eclogite	Scan_11	155.1	3.11258	5.3	3.3	4.2	71.4818	49.83
DDM_21	A154N	Eclogite	Scan_12	697.2	-	10.3	5.8	6.3	-	-
DDM_276	A154N	Eclogite	Scan_13	215.3	3.14674	6.1	3.2	4.9	91.0121	68.42
DDM_141	A154S	Eclogite	Scan_15	153.4	3.20184	5.4	3	4.2	73.6857	47.91
DDM_284	A154N	Eclogite	Scan_16	1294.3	3.21989	14.3	5.8	10.7	320.064	401.97
DDM_355	A154N	Eclogite	Scan_17	2047.2	-	15	7.2	10.5	426.859	
DDM_22	A154N	Eclogite	Scan_18	1570.3	3.16026	14.2	6.2	9.7	353.196	496.89
DDM_91	A154N	Eclogite	Scan_19	1129.3	3.35164	13.2	6.2	7.2	283.125	336.94
DDM_240	A154N	Eclogite	Scan_24	122.5	3.23134	4.8	3.6	3.7	58.1889	37.91
DDM_2	A154N	Eclogite	Scan_28	207.7	3.2719	5.7	3.8	5	83.4992	63.48
DDM_331	A154N	Eclogite	Scan_31	154.4	3.19669	6.1	3.1	4.8	72.3166	48.3
DDM_105	A154N	Eclogite	Scan_37	84.3	3.21756	4.1	3.1	3.4	45.4312	26.2
DDM_374	A154N	Eclogite	Scan_39	12.5	2.7115	2.6	1.9	2.3	14.5627	4.61
DDM_299	A154N	Eclogite	Scan_44	215.2	3.21002	6.4	3.7	5	88.265	67.04
DDM_249	A154N	Eclogite	Scan_46	90.4	3.26001	5	2.9	4.3	50.5514	27.73
DDM_181	A154N	Eclogite	Scan_47	639.1	3.14348	11.3	4.1	7.6	204.953	203.31
DDM_267	A154N	Eclogite	Scan_48	329.9	3.31624	7.8	3.4	6.3	121.616	99.48

DDM_185	A154N	Eclogite	Scan_49	4.24	0.30286	3.9	2.2	2.9	30.485	14
DDM_253	A154N	Harzburgite	Scan_29	403	2.98364	9.3	3.8	6.6	158.358	135.07
DDM_131	A154N	Harzburgite	Scan_36	457.4	3.10776	8.7	5.2	6.3	164.511	147.18
DDM_134	A154N	Lherzolite	Scan_20	772.8	2.75174	10.2	5.4	8.7	234.172	280.84
DDM_152	A154N	Lherzolite	Scan_21	126.8	3.03931	5.3	3.7	3.7	63.704	41.72
DDM_364	A154N	Lherzolite	Scan_25	323.9	3.11053	8.5	3.6	6.3	123.76	104.13
DDM_110	A154N	Lherzolite	Scan_26	220.2	2.92081	7.4	2.9	6.2	114.643	75.39
DDM_151	A154N	Lherzolite	Scan_32	609.8	2.98351	9.9	4.7	8.5	203.802	204.39
DDM_150	A154N	Lherzolite	Scan_33	557.9	2.93972	10.2	4.4	8.7	202.559	189.78
DDM_144	A154N	Lherzolite	Scan_34	266.4	3.02555	6.8	4	5.6	110.838	88.05
DDM_138	A154N	Lherzolite	Scan_35	922.8	2.87934	13.2	6.5	6.9	273.78	320.49
DDM_139	A154N	Lherzolite	Scan_38	743.4	2.8996	10.3	6.8	7.2	232.969	256.38
DDM_42	A154N	Lherzolite	Scan_40	250.7	2.85763	6.7	4.4	5.7	116.924	87.73
DDM_155	A154N	Lherzolite	Scan_41	153	3.03331	6	3.7	4.8	75.9721	50.44
DDM_154	A154N	Lherzolite	Scan_43	70.5	2.89766	5.2	2.4	3.6	46.8107	24.33
DDM_214	A154N	Lherzolite	Scan_45	91.9	2.81126	5.4	2.7	4.3	60.7806	32.69
DDM_223	A154N	Lherzolite	Scan_50	706.4	3.14305	10.6	4.6	8.3	212.714	224.75
DDM_31	A154N	Sheared Lherzolite	Scan_27	435.3	2.82204	8.9	3.9	6.8	164.42	154.25

Table D.1-1. Morphology dataset collected by analyzing select xenoliths from the University of Alberta Diavik collection. Axis measurements were taken using calipers and surface area and volume were extracted from 3D scans of the xenoliths.

D.2 3D Laser Scanner Methods

A NetEngine™ 3-D laser scanner was used to scan the outer surfaces of a selection of eclogite and peridotite xenoliths from the A154S pipe of the Diavik diamond mine. Using the ScanStudio HD PRO software, a sample was placed on a rotating pad and scanned with a resolution of 110,000 data points / cm^2 in macro mode. After being scanned, the sample would rotate 45 degrees to prepare for another scan. This was repeated 8 times to ensure the surface was approximated as well as possible and that no surface details were lost. Because the top and bottom of the rock sample are unreachable by the laser, the sample was rotated 90 degrees and the same process was carried out on the rotated xenolith. After this, the two scans were aligned using the ScanStudio software. Finally, all scans were fused together to form a completed mesh surface and any small holes in the mesh were filled. All surface area data of the samples were obtained using the software. Volume data was acquired by exporting the fused mesh as a .STL file and computed in using Gwyddion, an open source software designed to obtain surface data of meshes.

Appendix E MATLAB Shape Script

```
function results = myimfcn(im)

im = im2bw(im);
im = imcomplement(im);
bw = im;

imshow(bw);

% Use every 3rd pixel of the shape boundaries for the perimeter calculation
% (appears to provide truest estimate of perimeter):
s_wavelength=3;

% Remove the noise from the image, by deleting all of the "specks" on the
% image which do not belong the samples of interest (<10000 pixels):
bw = bwareaopen(bw,10000);

% Fill in any holes within the samples' boundaries:
bw = imfill(bw,'holes');

%% Trace the boundary of the Crystal

[B,L,NumberOfObjects] = bwboundaries(bw,'noholes');
% Option to display number of detected objects:
NumberOfObjects;

% Display image with a grayish background ([.5 .6 .6]), where the
% samples are shown coloured according the the 'summer' colour map, and
% outlined with a white line of width 2:
imshow(label2rgb(L, @summer, [.5 .6 .6]))
hold on
for k = 1:length(B)
boundary = B{k};
plot(boundary(:,2), boundary(:,1), 'w', 'LineWidth', 2)
end

%%  Calculate properties of samples' images


stats =
regionprops(L,'Area','Centroid','MajorAxisLength','MinorAxisLength','ConvexAr
ea','Perimeter','ConvexImage');

for k = 1:length(B)
boundary = B{k};
A = size(boundary);
boundary2 = boundary(s_wavelength:s_wavelength:A(1,1),:);
delta_sq = diff(boundary2).^2;
perimeter = sum(sqrt(sum(delta_sq,2)));
```

```
area2 = stats(k).Area;
area = polyarea(boundary2(:,1),boundary2(:,2));
% Metric for roundness: 4*pi*area/perimeter^2, which = 1 for a circle, and
% which < 1 for any other shape:
circularity = 4*pi*area/perimeter^2;
% Metric for elipticity: E = Pellipse/Perimeter
Pellipse = pi*(3*(stats(k).MajorAxisLength /2 +stats(k).MinorAxisLength/2) -
sqrt(((3*stats(k).MajorAxisLength
/2)+(stats(k).MinorAxisLength/2))*((stats(k).MajorAxisLength/2)+(3*stats(k).M
inorAxisLength/2))));
Ellipticity = Pellipse / perimeter;
%convexity metric (liu et al. 2015):
%Convexity = stats(k).Perimeter / perimeter;
%solidity metric (liu et al. 2015):
Solidity = area / stats(k).ConvexArea;

metric_string = sprintf('%2.2f',perimeter);
metric_string2 = sprintf('%2.2f',stats(k).MajorAxisLength);
metric_string3 = sprintf('%2.2f',stats(k).MinorAxisLength);
metric_string4 = sprintf('%2.2f',stats(k).Area);
metric_string5 = sprintf('%2.2f',stats(k).ConvexArea);
metric_string6 = sprintf('%2.4f',circularity);
metric_string7 = sprintf('%2.4f',Ellipticity);
metric_string8 = sprintf('%2.4f',Solidity);

% Put title and legend on figure:
figure(1)
% Insert text box with sample set name:
figure(1)

text(boundary(1,2),boundary(1,1)+0,metric_string,'Color','k',...
'FontSize',10,'FontWeight','bold');
text(boundary(1,2),boundary(1,1)+30,metric_string2,'Color','blue',...
'FontSize',10,'FontWeight','bold');
text(boundary(1,2),boundary(1,1)+60,metric_string3,'Color','c',...
'FontSize',10,'FontWeight','bold');
text(boundary(1,2),boundary(1,1)+90,metric_string4,'Color','magenta',...
'FontSize',10,'FontWeight','bold');
text(boundary(1,2),boundary(1,1)+120,metric_string5,'Color','r',...
'FontSize',10,'FontWeight','bold');
text(boundary(1,2),boundary(1,1)+150,metric_string6,'Color','k',...
'FontSize',10,'FontWeight','bold');
text(boundary(1,2),boundary(1,1)+180,metric_string7,'Color','k',...
'FontSize',10,'FontWeight','bold');
text(boundary(1,2),boundary(1,1)+210,metric_string8,'Color','k',...
'FontSize',10,'FontWeight','bold');
%text(boundary(1,2),boundary(1,1)+240,metric_string9,'Color','k',...
%'FontSize',10,'FontWeight','bold');
end

%Compute convexity
image(stats(k).ConvexImage)
%find perimeter of convex hull
im_CH = im2bw(stats(k).ConvexImage);
```

```
stats_hull = regionprops(im_CH,'Perimeter');
convexity = stats_hull.Perimeter / perimeter;


results.area = area
results.CHarea = stats(k).ConvexArea
results.perimeter = perimeter
results.CHperimeter = stats_hull.Perimeter
results.circularity = circularity
results.ellipticity = Ellipticity
results.convexity = convexity
results.solidity = Solidity
results.u_MajorAxisLength = stats(k).MajorAxisLength
results.u_MinorAxisLength = stats(k).MinorAxisLength
results.u_AxialRatio = stats(k).MinorAxisLength/stats(k).MajorAxisLength
```

Appendix F Physical Mineral Property References Used

Mineral Property	Forsterite	Enstatite	Chrome Diopside	Pyrope	Diamond
Density ($g\ cm^{-3}$)	N/A	N/A	N/A	N/A	N/A
Hardness	N/A	N/A	N/A	N/A	N/A
Chemical Formula	N/A	N/A	N/A	N/A	N/A
Crystal System	N/A	N/A	N/A	N/A	N/A
Cleavage	N/A	N/A	N/A	N/A	N/A
Fracture	N/A	N/A	N/A	N/A	N/A
Hardness (GPa)	Lee et al. (2012)	Sinogeikin et al. (1997)	Smedskjaer et al. (2008)	Whitney et al. (2007)	105
Tensile Strength (MPa)	Brett et al. (2015)	N/A	Kovaleva (1974)	N/A	Field (2012)

Bulk Modulus (GPa)	N/A	Kumazawa (1969)	Sang et al. (2011)	Tromans & Meech (2002)	Grimsditch & Ramadas (1975)
Young's Modulus (GPa)	Swain & Atkinson (1978)	KanParker et al. (2010)	N/A	Van Westrenen et al. 1999	Grimsditch & Ramadas (1975)
Fracture toughness (MPa $m^{1/2}$)	Tromans & Meech (2002)	N/A	Wang et al. (2014)	Whitney et al. (2007)	Field & Freeman (1996)
Fracture Surface Energy (J m^{-2})	Swain & Atkinson (1978)	N/A	N/A	Tromans & Meech (2002)	Field (2012)